Computational discovery and characterization of novel 2D materials

A 2D Materials Encyclopedia

Haastrup, Sten

Publication date:
2019

Document Version
Publisher's PDF, also known as Version of record

Ph.D. Thesis
Doctor of Philosophy

DTU Physics
Department of Physics

Computational discovery and characterization of novel 2D materials

A 2D Materials Encyclopedia

Sten Haastrup

Kongens Lyngby 2018

DTU

DTU Physics
Department of Physics
Technical University of Denmark

Fysikvej
Building 307
2800 Kongens Lyngby, Denmark
Phone +45 4525 3344
info@fysik.dtu.dk
www.fysik.dtu.dk

Abstract

In this thesis we have systematically investigated the ground state and response properties of around 3000 two-dimensional materials using density functional theory (DFT) and many body perturbation theory methods. A computational workflow scheme has been developed which allows us to accurately calculate the structural, thermodynamic, elastic, electronic, magnetic, and optical properties of any two-dimensional material.

Today, around 50 compounds have been synthesised in monolayer form and many more layered materials are known. Using combinatorial lattice decoration, we generate new, hypothetical, structures from the existing ones and systematically calculate their properties. To ensure the physical reasonableness of the hypothetical structures, we carefully investigate their global (thermodynamic) and local (mechanical) stability. This analysis reveals hundreds of novel two-dimensional materials with high stability which it should be possible to synthesise. One of the most exciting features of two-dimensional materials is their ability to form heterostructures; patterned stacks of different two-dimensional materials, with precisely tunable properties. This means that the discovery of a new stable two-dimensional material also represents the discovery of a new building block in this stacking framework.

The systematic calculation of properties for all materials also allows us to investigate the performance of simpler models, and lets us understand in more detail where they break down. An example of this is the behaviour of bound electron-hole pairs: *excitons*. They are frequently modelled using a hydrogen-like equation, but comparison with the BSE binding energy reveals several regimes where the model performs poorly.

Access to the complete structured database enables us to study structure-property and property-property relations in a data-driven manner. Using this paradigm, we can accurately predict the heat of formation of the two-dimensional materials based on knowledge of the chemical composition and the abstract crystal structure. Further investigations in this direction are likely to yield promising descriptors for more complex properties.

Recognising the unavoidable trade-off between computational depth and computational breadth, we also identify some tens of materials with novel magnetic, plasmonic or transport properties; which would be worth studying in greater detail, using more advanced methods.

Finally, at the complete opposite end of the depth vs. breadth spectrum from the systematic study of 3000 materials, we investigate the dissociation of excitons in a single two-dimensional material, MoS_2, upon application of an electric field. From this we conclude that it is possible to generate free electrons and holes using realistic field strengths.

Resumé

I denne afhandling er en række strukturelle, termodynamiske, elastiske, electroniske, magnetiske og optiske egenskaber beregnet for omkring 3000 atomart tynde materialer. Beregningerne bygger på tæthedsfunktionalteori (DFT) og mange-legeme perturbationsteori (MBPT). Der er udviklet et workflow til automatisk at beregne egenskaber for et vilkårligt to-dimensionelt materiale.

På nuværende tidspunkt er omkring 50 to-dimensionelle materialer blevet syntetiseret, og mange flere lagdelte strukturer kendes. Ved systematisk at dekorere det underliggende atomgitter for de kendte strukturer med andre grundstoffer fra det periodiske system kan vi generere nye, hypotetiske strukturer ud fra eksisterende, og derefter beregne deres egenskaber. For at sikre at de hypotetiske strukturer er fysisk ladsiggørlige, foretages en grundig analyse af deres lokale (mekaniske) stabilitet og deres globale (termodynamiske) stabilitet. Ud fra denne analyse ses det at flere hundrede af de undersøgte materialer er stabile, og det ville derfor være muligt at syntetisere dem. En af de ting der kendetegner to-dimensionelle materialer er at de nemt kan stables til Van der Waals heterostrukturer; kunstigt lagdelte strukturer med skræddersyede egenskaber. Hvert nyt to-dimensionelt materialer der opdages, repræsenterer derfor også en ny byggeklods i dette univers.

Når vi beregner egenskaber systematisk for mange forskellige materialer er det også muligt at undersøge opførslen af simplere modeller og tilnærmelser, og opnå en dybere forståelse af hvornår de er gyldige. Et eksempel på dette er bundne elektron-hul par i to-dimensionelle materialer: *eksitoner*. De beskrives ofte ved hjælp af en brintatomlignende model, men en sammenligning med resultaterne fra Bethe-Salpeter ligningen viser en række områder hvor denne beskrivelse er utilstrækkelig.

Den komplette samling af data gør det også muligt at undersøge sammenhænge mellem struktur og egenskaber, og mellem forskellige egenskaber. Ved brug af maskinllæring er det muligt nøjagtigt at forudsige energien af forskellige strukturer udelukkende ved kendskab til deres komposition og deres krystalstruktur.

I et hvert studie må der foretages en afvejning af dybde og bredde, og på baggrund af nogle udvælgelseskriterier identificeres derfor en række materialer som kunne være interessante at studere nærmere. Materialerne har interessante transport-, magnetiske, eller plasmoniske egenskaber, som gør at de kunne finde teknologisk anvendelse.

Endelig – i den modsatte ende af dybde/bredde spektret fra hvor vi startede – studeres dissociation af eksitoner i et enkelt materiale, MoS_2, og det konstateres at det er

muligt at generere frie elektroner og huller ved realistiske elektriske feltstyrker.

Preface

This thesis is submitted in candidacy for the Ph.D degree in physics from the Technical University of Denmark. The work was carried out at the section for Computational Atomic-scale Materials Design (CAMD) ath the Department of Physics, in the period from October 2015 to October 2018, and supervised by professors Kristian S. Thygesen and Karsten W. Jakobsen. The Ph.D. project was funded by an internal scholarship from DTU.

Kongens Lyngby, 1st October 2018

Sten Haastrup

Acknowledgements

- Kristian

A Ph.D. project, lasting 3 years, is ultimately the work of many more people than just the Ph.D. candidate. I would like to take the time to thank some of the people who have been involved in the project, and who have helped ensure that the end result is good.

First of all, this project and this thesis would not have existed had it not been for my supervisor, Kristian. I am extremely grateful for all the fruitful discussions we've had throughout the last years, and I remain in awe of your physical insight and intuition, and of your enthusiasm.

A big thanks goes out to both Korina and Kåre, with whom I have shared an office for the past three years, and who've therefore had to put up with me for a total of at least 4800 hours. Thanks for celebrating with me when things were going well, and for commiserating with me when things were going less well. To Korina, thanks for being brave enough to go travelling with me, not just once or twice, but three times. We'll have to do some more of that now!

Jens Jørgen and Mikkel also deserve a great thanks. Jens Jørgen, for seemingly knowing everything about electronic structure calculations and python, and for always having the time to answer questions and to help. Mikkel for all your efforts in our collaboration on the 2D database, and for our discussions on how to best implement things.

To Marianne, a big thanks for always being organised and knowing what was going on, even if no-one else did. I'm fairly sure that the section would fall apart without you!

To the CAMD gang, past and present – Anders, Asbjørn, Chris, Estefania, Jacob, Kirsten, Luca, Lucas, Mohnish, Morten, Nicki, Per Peter, Philip, Simone, Simone, Suranjan, Thorbjørn and Thorsten – thanks for making CAMD such a nice place to work, for the good discussions over the coffee machine, and for the much better discussions over pizza.

To all my friends outside DTU physics, thanks for being part of my life, and thanks. In particular thank you to Lisbeth, Daniel, Christoffer and Jonathan for our regular

swimming and gymming sessions. They've always helped clear my head, not matter what else was going on.

Thank you also to my parents, Palle and Kirsten, and to my sister Birgit for all their love and support during these years, especially perhaps during the last six months, when it was needed more than ever. And to my brother Erik, who wanted to be mentioned in this section, "Hi, Erik!"

Contents

CHAPTER 1

Introduction

Technological advancement and access to new materials go hand in hand, with new materials enabling the invention of new technologies, and new technologies enabling the discovery of new materials. Finding and exploiting new materials is thus the key to unlocking the technologies of tomorrow. The historical examples of this are too many to list, but a notable examples of each situation can be found in the case glass and aluminium. Glass provides an example of a materials-driven technological advancement, as high-quality glass is a prerequisite for the production of lenses, for glasses, binoculars or telescopes. Aluminium provides a clear example of the opposite case – technologically driven materials discovery. Aluminium commonly occurs as aluminium oxide, and to produce metallic aluminium from alumina involves an electrolytic process, and a high degree of technological sophistication.

Currently, much of our lives and societies have been shaped by one single material, namely silicon. If we return to an earlier practice of naming historical eras after materials, we might well be said to be living in the Silicon Age. The invention of the transistor in the late 1940s and early 1950s[1, 2] has enabled the computer revolution, and the ever-decreasing cost and size of silicon transistors has meant that in less than the space of a human lifetime we have progressed from having large mainframe computers typically operated by large companies or scientific institutions to having ubiquitous computers in our pockets. This trend of miniaturization has resulted in feature sizes in the latest generation of computer processors reaching just 7 nm[3], and has been partly responsible for the emergence of the field of nanoscience. Eventually, it will no longer be possible to continue this trend of miniaturizing features in silicon, and something new will emerge – either a new material or a new technology to build new devices.

In 2004, Kostya Novoselov and André Geim successfully isolated a single layer of carbon atoms in a hexagonal lattice: graphene[4]; for which discovery they were awarded the Nobel Prize in physics in 2010. Graphene is in many ways an extraordinary material, characterized by a high thermal conductivity[5], a high carrier mobility[6], and a large tensile strength [7]. Graphene also has unique quantum properties[8], but one thing it does not have is a band gap, making it unsuitable for many applications. Much research has gone into modifying or patterning graphene to achieve a gap[9, 10], but so far only with modest success.

Following the discovery of graphene, mechanical or liquid exfoliation of many other

layered compounds was attempted, leading to a whole family of known 2D materials, with many different properties, so that both metallic, semi-metallic, semiconducting and superconducting 2D materials have been observed[11, 12] though these materials have different properties, their 2D nature means that they also have a number of things in common, namely a significant quantum confinement effect and a weak dielectric screening. Additionally, the materials have in common that their exact properties are easily tunable, through mechanical strain, electrostatic gating, or substrate interactions[13, 14]. Finally, 2D materials represent perhaps the ultimate maximization of the surface area to volume ratio, giving them an advantage in applications where the surface area is important, such as catalysis and light absorption. So far more than 50 compounds have been synthesized in monolayer form, and it seems that 2D materials are much more common than anyone would have dreamed of in 2004. Additionally, it has proven possible to stack different 2D layers in so called van der Waals heterostructures[15, 16], allowing high-precision control of the properties of the resulting structure.

There is no reason to believe that the currently synthesized 2D materials are the only ones which could exist, and the discovery of new 2D materials is an active field of research, and this is where computational materials design can play an important role. The tremendous increase in computer power in the last 50 years, as well as the continued advances in theoretical models means that it is currently possible to simulate materials properties with accuracies comparable to experiments, but much faster, and at a much lower cost. Starting from experimentally known layered structures, a recent computational study found hundreds of materials where single layers could potentially be exfoliated, exactly like graphene was in 2004[17].

In this work, we have taken a different approach, and explored 2D materials with no known layered analogue. Instead, we have based our exploration on the crystal structures of the known 2D materials, and systematically replaced the constituent atoms of the known structures with chemically similar atoms from the periodic table. This has led to a set of 3000 materials being investigated, with 550 of these being classed as stable.

By casting the net wide, we undoubtedly calculate the properties of materials which turn out not to be of interest. The great advantage of consistently calculating all properties for all but the most unstable materials is that it allows us to see which properties correlate to one another, and how these are linked to the structure of the material. Ultimately, this allows us to develop easy to calculate descriptors for the properties we are interested in.

The second advantage of a systematic and comprehensive calculation is that it can serve as a reference for future work, thereby avoiding the duplication of efforts. Additionally, the creation of open databases helps the development and testing of new methods, and serves as a useful tool for benchmarking[18].

In any study there is a trade-off between depth and breadth: It is possible to examine a large number of different materials, and it is possible to examine materials in great

depth, but it is not possible to do both at the same time, and the essential thing is to know when to use which approach.

1.1 Outline

The remainder of this thesis is structured as follows:

Chapters 2 and 3 provide necessary background information on the tools we use to describe the properties of matter and how matter responds to external perturbation. Chapter 4 presents an overview of how we can use these methods to accurately calculate the properties of many novel two-dimensional materials, and in chapter 5 I restrict myself to describing a single type of excitation in monolayer MoS_2.

CHAPTER 2

Electronic Structure Theory

This chapter describes the fundamental theory we use to calculate and describe the properties of matter, from both a theoretical and a practical perspective

Since the start of the 20th century we have known that on a microscopic level, matter consists of atoms, which in turn are made up of light electrons and heavy nuclei. Adopting a bottom-up perspective, the properties of matter are determined by the behavior of the electrons and nuclei. The incredible variety of materials and their properties that we see in our daily lives can thus – in principle – be understood by understanding the behavior of the electrons and nuclei which make up the materials. The goal of electronic structure theory is then to predict the behavior of electrons and nuclei in any configuration.

2.1 The many-body Hamiltonian

The two ingredients needed for a quantum mechanical description of matter are the wave function and the Schrödinger equation. The wave function describes the configuration of a system as a function of time, and is written $\Psi(\underline{\mathsf{r}}, \underline{\mathsf{R}}, t)$, where $\underline{\mathsf{r}}$ and $\underline{\mathsf{R}}$ denote the full set of electronic and nuclear coordinates respectively: $\underline{\mathsf{r}} = \{\mathbf{r}_i\}$, $\underline{\mathsf{R}} = \{\mathbf{R}_i\}$. The Schrödinger equation then describes how this configuration evolves in time

$$\hat{H}(t)\Psi(t) = -i\partial_t \Psi(t), \tag{2.1}$$

where we have used atomic units as described in Appendix A, and suppressed all arguments to the functions apart from time.

Frequently, we are interested in equilibrium properties of materials, and the relevant equation becomes the time independent Schrödinger equation,

$$\hat{H}\Psi = \varepsilon\Psi(t). \tag{2.2}$$

Here ε denotes the eigenvalue corresponding to the many body eigenfunction of the Hamiltonian, $\hat{H}$. The general Hamiltonian of a system of N electrons and M nuclei

interacting via the Coulomb interaction can be written as

$$\begin{aligned}\hat{H} &= \hat{T}_{\mathrm{e}} + \hat{T}_{\mathrm{n}} + \hat{U}_{\mathrm{ee}} + \hat{U}_{\mathrm{nn}} + \hat{U}_{\mathrm{ne}} \\ \hat{H} &= -\sum_{i=1}^{N} \frac{\nabla_i^2}{2} - \sum_{I=1}^{M} \frac{\nabla_I^2}{2M_I} \\ &\quad + \frac{1}{2}\sum_{i=1}^{N}\sum_{j\neq i} \frac{1}{|\mathbf{r}_i - \mathbf{r}_j|} + \frac{1}{2}\sum_{I=1}^{M}\sum_{J\neq I} \frac{Z_I Z_J}{|\mathbf{R}_I - \mathbf{R}_J|} \\ &\quad - \sum_{i=1}^{N}\sum_{I=1}^{M} \frac{Z_I}{|\mathbf{r}_i - \mathbf{R}_I|}\end{aligned} \tag{2.3}$$

The first two terms represent the kinetic energy of the electrons and nuclei respectively, while the next three terms describe the electron-electron, the nucleus-nucleus and the electron-nucleus interaction. M_I and Z_I are the mass and charge on the I'th nucleus, and the factor $\frac{1}{2}$ appearing in both terms on the second line accounts for the double counting of the interaction between electrons i and j and j and i.

In principle, all equilibrium properties of a system can be found by solving the Schrödinger equation with this Hamiltonian. In practice, this is infeasible for all but the simplest systems. This is due to the coupling between all the electronic and nuclear degrees of freedom arising from the Coulomb interaction, which means that we cannot describe each electron or nucleus separately, as their behavior depends on that of all the others. Consider the example of a system consisting of two electrons and two nuclei (four particles in total). If we discretize space into a grid of $16\times16\times16$ points, specifying a single many-body configuration requires $16^{12} = 2^{48} \approx 2 \times 10^{14}$ numbers.

To proceed, a number of simplifying assumptions are therefore needed. One first simplification we can make is to separate the electronic and nucleic degrees of freedom. A proton is 2000 times heavier than an electron, and the nuclei will therefore move on very different timescales to the electrons. From the point of view of the electrons, the nuclei can be considered stationary, while from the point of view of the nuclei, the electrons can be considered to always be in their ground state. This is known as the Born-Oppenheimer approximation, and corresponds to making the ansatz $\Psi(\underline{\mathsf{r}}, \underline{\mathsf{R}}) = \psi(\underline{\mathsf{r}}; \underline{\mathsf{R}}) \otimes \Phi(\underline{\mathsf{R}})$. The electronic wave function depends *parametrically* on the nuclear coordinates, meaning that the functional form of $\psi(\underline{\mathsf{r}})$ depends on the nuclear coordinates.

The Hamiltonian for the electronic system can then be written as

$$\hat{H}_{\mathrm{el}} = \hat{T}_{\mathrm{e}} + \hat{V}_{\mathrm{ee}} + \hat{V}_{\mathrm{ext}}, \tag{2.4}$$

Where $\hat{V}_{\mathrm{ext}}$ describes the Coulomb potential set up by the nuclei, as well as any external potential applied. The number of degrees of freedom in this equation has

thus been reduced from $3(M + N)$ to $3N$. Returning to the example above, this means that it would now be feasible to store the configuration of up to four electrons.

Evidently further approximations are needed, in order to render the problem tractable. Before moving on, it is however worth stepping back to see what has been accomplished. We started this chapter with the goal of describing the behavior of matter, and have now reduced this problem to that of describing a system of interacting electrons moving in an external potential – a great simplification!

2.2 Density functional Theory

One very successful approach to avoiding the complexities involved in solving the many-body Schrödinger equation directly is to focus on the electron density instead of the electronic wave function. The density is inherently a much simpler quantity than the wave function, as it is a function of only three variables, rather than $3N$, so if it is possible to formulate the electronic structure problem in terms of the density, much complexity could be avoided.

The first attempts in this direction were made in the 1920s by Thomas and Fermi[19, 20], but it was not until the 1960s that modern density functional theory (DFT) emerged[21][22]. The basis of DFT consists of the Hohenberg-Kohn theorems, which demonstrate that it is indeed possible to work only with the density, rather than the many body wave function.

The first Hohenberg-Kohn theorem states that

First Hohenberg-Kohn Theorem *There is a one-to-one mapping between the external potential and the ground state density of a system.*

That a given potential gives a given ground state density is obvious. For, knowing the potential, we could solve the many-body Schrödinger equation to get the ground state wave function, and from this we could obtain the density. The other direction is more surprising, since there is no *a priori* reason that we could not have two different external potentials which gave rise to the same ground state density, but with different ground state wave functions. But this is not the case, as will be shown. Suppose two different external potentials $\hat{V}$ and $\hat{V}'$ gave rise to the same electronic density $n_0(\mathbf{r})$. The potentials would have different Hamiltonians, $\hat{H}$ and $\hat{H}'$, and different corresponding ground state wave functions, ψ and ψ'. If we let E_0 and E_0' be the non-degenerate ground state energies of the two systems, we are ready to proceed. As E_0 is the ground state energy of $\hat{H}$, we must have that the expectation value of H on ψ' is strictly greater than E_0

$$\begin{aligned} E_0 < \left\langle \psi' \middle| \hat{H} \middle| \psi' \right\rangle &= \left\langle \psi' \middle| \hat{H}' \middle| \psi' \right\rangle + \left\langle \psi' \middle| \hat{H} - \hat{H}' \middle| \psi' \right\rangle \\ &= E_0' + \int \mathrm{d}\mathbf{r}\, n_0(\mathbf{r}) \left[V(\mathbf{r}) - V'(\mathbf{r}) \right] \end{aligned} \tag{2.5}$$

Similarly for the expectation value of $\hat{H}'$ on ψ:

$$E_0' < \left\langle \psi \middle| \hat{H}' \middle| \psi \right\rangle = \left\langle \psi \middle| \hat{H} \middle| \psi \right\rangle + \left\langle \psi \middle| \hat{H}' - \hat{H} \middle| \psi \right\rangle$$
$$= E_0 + \int \mathrm{d}\mathbf{r}\; n_0(\mathbf{r}) \left[V'(\mathbf{r}) - V(\mathbf{r}) \right] \tag{2.6}$$

Summing Eq. (2.5) and (2.6) we arrive at the contradiction that $E_0 + E_0' < E_0 + E_0'$, and the theorem is thus proved. Since the ground state wave function can be determined from the external potential, this means that the ground state wave function and the ground state density contain the same information: knowing one, we can find the other. This means that the expectation values of the kinetic energy and the electron-electron interaction energies are also functionals of the density. The ground state energy of the system can then be written

$$E_0 = E[n_0] = T[n_0] + V_{\mathrm{ee}}[n_0] + \int \mathrm{d}\mathbf{r}\; n_0(\mathbf{r}) v_{\mathrm{ext}}(\mathbf{r}) \tag{2.7}$$

The first two terms on the right hand side are independent of the system under consideration, that is, the functional $F[n] \equiv T[n] + V_{\mathrm{ee}}[n]$ is *universal*. The second Hohenberg-Kohn theorem then states that

Second Hohenberg-Kohn Theorem *The total energy functional is subject to a variational principle, so that $E[n] \geq E[n_0]$ for all densities $n(\mathbf{r})$.*

We can thus find the ground state density by minimizing $E[n]$. This can be seen by using the mapping between the ground state density and the ground state wave function established by the first theorem. This variational approach gives us a method to find the ground state density, by evaluating the energy functional $E[n]$ at different densities, and looking for a minimum.

Together, these two theorems can help us solve the problem of having to find the many-body wave function, by focusing on the density instead. It should be emphasized that so far the theory is exact, and no approximations have been made. The main problem is that until now both $T[n]$ and V_{ee} are only implicit functionals of n, through the bijection between the ground state wave function and the ground state density. Thus, in order to evaluate them, we would need to calculate the many body wave function - exactly what we wish to avoid. To proceed, we need a further trick, and this is found in the Kohn-Sham equations.

2.3 Kohn-Sham DFT

To overcome the issue of having to find the many-body wave function, Kohn and Sham proposed an ingenious scheme in 1965[22]. The crucial idea insight is to consider a reference system consisting of non-interacting electrons moving in an effective

potential, and then to require that this reference system and the true system have the same ground state density.

We start by splitting the energy functional in (2.7) into known and unknown parts

$$E[n] = T_{\mathrm{r}}[n] + V_{\mathrm{H}}[n] + V_{\mathrm{ext}}[n] + \underbrace{T[n] - T_{\mathrm{r}}[n] + V_{\mathrm{ee}}[n] - V_{\mathrm{H}}[n]}_{E_{\mathrm{xc}}[n]}, \tag{2.8}$$

where T_{r} is the kinetic energy of the non-interacting reference system and the Hartree energy, $V_{\mathrm{H}} \equiv \int \mathrm{d}\mathbf{r}'\mathrm{d}\mathbf{r}\, \frac{n(\mathbf{r})n(\mathbf{r}')}{|\mathbf{r}-\mathbf{r}'|}$, is the classical electrostatic energy associated with a charge distribution $n(\mathbf{r})$. The last term, E_{xc} is the so-called *exchange-correlation* functional and accounts for all of the many-body effects in our system.

For the non-interacting reference system moving in an effective potential, a general energy functional reads $E_{\mathrm{r}}[n] = T_{\mathrm{r}}[n] + V_{\mathrm{KS}}[n]$, where $V_{\mathrm{KS}}[n] = \int \mathrm{d}\mathbf{r}\; n(\mathbf{r}) v_{\mathrm{KS}}(\mathbf{r})$ is the energy associated with the effective potential $v_{\mathrm{KS}}(\mathbf{r})$. Requiring that the reference system and the true system have the same ground state density is the same as requiring that the same density minimizes both energy functionals. This in turn allows us to write the effective potential in terms of functional derivatives

$$\begin{aligned} v_{\mathrm{KS}} &= \frac{\delta V_{\mathrm{H}}}{\delta n} + \frac{\delta V_{\mathrm{ext}}}{\delta n} + \frac{\delta E_{\mathrm{xc}}}{\delta n} \\ &= v_{\mathrm{H}}(\mathbf{r}) + v_{\mathrm{ext}}(\mathbf{r}) + v_{\mathrm{xc}}(\mathbf{r}) \end{aligned}$$

Using this effective potential, we are ready to find the ground state of the reference system. We can readily find the relevant one-electron orbitals by solving the single-particle Schrödinger equation

$$\left[-\frac{\nabla^2}{2} + v_{\mathrm{KS}}(\mathbf{r})\right] \phi_i(\mathbf{r}) = \varepsilon_i \phi_i(\mathbf{r}). \tag{2.9}$$

The ground state density of the non-interacting system can then be found by summing over the occupied orbitals, so that $n_{\mathrm{r}}(\mathbf{r}) = \sum_i^{\mathrm{occ}} |\phi_i(\mathbf{r})|^2$. Since the reference system is constructed so that it has the same ground state density as the true system, this finally allows us to obtain the ground state density we were seeking.

One thing to note is that both v_{H} and v_{xc} depend on the density, and the Kohn-Sham equations (2.9) must therefore be solved self-consistently: starting with a trial density, we evaluate the potential, v_{KS}, produced by that density. We then solve the Kohn-Sham equations using this potential to get a new density, which in turn produces a new potential. This process is repeated until the potential and the density agree.

2.4 The exchange-correlation functional

All of the complexity of the many-body problem has been hidden in the exchange-correlation term, and the usefulness of Kohn-Sham DFT depends on finding a good

expression for this term. If we knew the exact form of E_{KS}, the Kohn-Sham scheme would be exact, which is also an indication of the tremendous complexity which must be hidden there.

The simplest possible approximation which can be made is the Local Density Approximation (LDA). If we assume that the exchange-correlation energy depends only pointwise on the density, we can write

$$E_{\mathrm{xc}}^{\mathrm{LDA}} = \int \mathrm{d}\mathbf{r}\; n(\mathbf{r}) \epsilon_{\mathrm{xc}}^{\mathrm{LDA}}(n(\mathbf{r})). \tag{2.10}$$

The exchange-correlation energy density, $\epsilon_{\mathrm{xc}}^{\mathrm{LDA}}$, is now just a function[1] rather than a functional[2], since it depends only on the density at a single point, rather than the whole density. If we restricted ourselves only to constant densities, the above expression would be exact. On the other hand, for an electron gas of constant density – the homogeneous electron gas – we have analytical results for the exchange energy density[23], and the correlation energy density has been found through quantum Monte Carlo simulations[24]. A first approximation to the exchange-correlation energy is thus to take the exchange and correlation energy densities from the homogeneous electron gas and use directly in Eq. (2.10). Because the approximation is based on the homogeneous electron gas, the LDA should be expected to perform well when used for systems where the density is approximately uniform. In practice it has worked surprisingly well even for systems which are far from uniform, mainly due to a fortuitous cancellation of errors in the estimates for the exchange and correlation energies[25]. Overall, the LDA underestimates band gaps[26] and thus overestimates the dielectric screening[27].

A natural extension of the local density approximation is to include not only the density at each point in the calculation of the exchange-correlation energy, but also the gradient of the density. This leads to a class of functionals known as the generalized gradient approximations (GGAs). In this work these will mainly be used in the form written down by Purdue, Burke and Ernzerhof[28].

2.5 Beyond DFT: Many-body perturbation theory

By construction, DFT is intended to reproduce exactly the ground state density, and all quantities which can be written as functionals of the ground state density. The wave functions and single particle eigenvalues which appear in the Kohn-Sham formulation of DFT are not physically meaningful, and there is no reason that they should reproduce experimentally observed band structures and band gaps.

A very useful way of correctly calculating the single particle energies can be found in the many-body perturbation theory approach. When an electron is added from the

[1] A map from $\mathbb{R}^3$ to $\mathbb{R}$.
[2] A map from the space of functions on $\mathbb{R}^3$ to $\mathbb{R}$.

system, the repulsive force on all the other electrons creates a region around the electron with decreased electronic density. Compared with the neutral system, the bare electron is thus dressed by a positively charged screening cloud. The quasi-particle excitations of the system correspond to the bare electron along with its screening cloud. The same applies, mutatis mutandis, for excitations involving electron removal. The success of the quasiparticle approach lies in the fact that the dressed electrons interact weakly with one another through the screened Coulomb interaction, and a single-particle picture is thus appropriate.

To obtain the quasiparticle energies and eigenfunctions, we should solve the single-particle equation,

$$\left(-\frac{1}{2}\nabla^2 + v_{\text{ext}} + v_{\text{H}})\right)\psi^{\text{QP}}(\mathbf{r}) + \int \mathrm{d}\mathbf{r}'\ \Sigma_{\text{xc}}(\mathbf{r},\mathbf{r}',\varepsilon^{\text{QP}})\psi^{\text{QP}}(\mathbf{r}') = \varepsilon\psi^{\text{QP}}(\mathbf{r}) \qquad (2.11)$$

where the non-local, energy-dependent self-energy Σ has replaced the exchange-correlation functional of the Kohn-Sham equations. The self-energy accounts for all exchange and correlation effects between quasiparticles in the system.

A very useful way of predicting quasiparticle energies and gaps is the GW approximation[29], in which the self-energy is defined as

$$\Sigma(\mathbf{r},\mathbf{r}',\omega) = i\int \omega G(\mathbf{r},\mathbf{r}',\omega+\omega')W(\mathbf{r},\mathbf{r}',\omega), \qquad (2.12)$$

where G is the single-particle Green's function, and W is the screened Coulomb interaction; see Eq. (3.2). The simplest approach to calculating the screened interaction is to use the Green's function and screened interaction arising from the Kohn-Sham eigenstates and eigenvalues of DFT. This is the so-called $\mathrm{G_0W_0}$ approximation and it has proven to give significantly more accurate band gaps than bare DFT[26].

Examining (2.11), we see that the self-energy should be evaluated at the quasiparticle energies in order to determine the potential experienced by the quasiparticles. Since these energies are not known beforehand, we can instead treat the correction $\Sigma - V_{\text{xc}}$ as a small quantity, and use first order perturbation theory to approximate the energies, giving

$$\varepsilon^{\text{QP}} \approx \varepsilon^{\text{KS}} + Z\left\langle \phi^{\text{KS}}\middle|\Sigma - V_{\text{xc}}\middle|\phi^{\text{KS}}\right\rangle \qquad (2.13)$$

The normalization factor Z is close to unity if the Kohn-Sham wave function is a good approximation to the quasi-particle wave function.

For more detail on the GW approximation, and on many body perturbation theory in general, we refer the reader to [30].

2.6 Electronic Structure Calculations in GPAW

So far, we have only discussed the physical and mathematical approximations which need to be made in order to perform electronic structure calculations. An additional level of approximations is introduced when it comes to carrying these approximations out in practice. The numerical approximations in DFT lie in the details of how the Kohn-Sham wave functions are represented, and how the self-consistent cycle in Eq. (2.9) is carried out.

In this work, we use the GPAW[31] electronic structure code to do calculations, and the atomic simulation environment (ASE) to work with atomic structures[32]. Wave functions in GPAW can be represented either on a real-space grid, using a plane-wave basis set, or as a linear combination of atomic orbitals. Unless otherwise stated, the calculations in this work have all been carried out using the plane wave basis set.

Close to the nuclei, the potential varies quickly, and the wave functions are expected to exhibit oscillations at very short length scales. Representing these oscillations with a plane wave basis set or on a grid would require prohibitively many basis functions. Since the wave functions oscillate over much longer length scales away from the nuclei, using this level of detail in all of space would be wasteful. To avoid this, GPAW uses the projector-augmented wave method[33] to divide space into two different regions. Close to the nuclei (inside the *augmentation spheres*), the wave functions are represented on an atom-like basis, while in the regions further away, the wave functions are represented using one of the three basis sets described above. Matching these representations at the boundary of the augmentation spheres ensures that we can access the all-electron (non-smooth) wave function via a linear transformation of the smooth wave functions.

An additional approximation which is frequently adopted, and which greatly speeds up calculations is the frozen core approximation. This approximation is rooted in the observation that the core electrons of a material are tightly bound to the nuclei and thus do not participate in bonding or (low-energy) excitations. Since they are insensitive to the chemical environment, their behavior can be calculated once and for all for the isolated atoms, and there is no need to treat them explicitly in Eq. (2.9).

As well as being a DFT calculator, GPAW has tools to carry out beyond-DFT calculations, such as GW calculations (as described in the previous section), as well as linear response calculations (see the following chapter) and the Bethe-Salpeter Equation (see chapter 5)

CHAPTER 3

Dielectric Response in Solids

In the previous chapter, we saw how all the complexities involved in describing the properties of matter can ultimately be reduced to the problem of describing how interacting electrons behave in an external potential. This insight holds for almost all cases of interest, but the tools we use to describe the electrons differ according to the properties we wish to study.

One of the key properties of a material is how it interacts with an electromagnetic field. From an experimental perspective, almost every probe we can make of a system will involve an electromagnetic field, whether it be in absorption, emission, reflectance EELS, or transport measurements. From a technological perspective, understanding the response to an electric field can greatly help in designing materials for novel applications. In the case of 2D materials, one of their unique properties is their strong interaction with light[34].

From classical electromagnetism, it is well known that when we apply an electric field to a material, the total field inside the material is different from the one we apply. This is because the applied field creates a macroscopic polarization in the material, which then creates its own field. The applied field is thus screened by the material. In Maxwell's equations, this is expressed by the difference between the field we apply – the displacement field, $\mathbf{D}$ – and the total field, $\mathbf{E}$. These two quantities are linked by the dielectric function $\mathbf{D} = \epsilon\mathbf{E}$, and for many bulk materials and purposes, ϵ is a constant. If the field is longitudinal, we can reformulate the problem in terms of potentials, and the dielectric function then expresses how the external potential varies as a function of the total potential:

$$\epsilon(\mathbf{r}, \mathbf{r}', t, t') = \frac{\delta v_{\text{tot}}(\mathbf{r}, t)}{\delta v_{\text{ext}}(\mathbf{r}', t')}. \tag{3.1}$$

The different arguments to the potentials indicate that the full dielectric function is non-local, so that a perturbation at a point $\mathbf{r}'$ can give rise to a response at $\mathbf{r}$. A more intuitive quantity than the dielectric function is the inverse dielectric function, which relates the total potential to the external potential, such that

$$v_{\text{tot}}(r,t) = \int \mathrm{d}t' \int \mathrm{d}\mathbf{r}' \, \epsilon^{-1}(\mathbf{r},t;\mathbf{r}',t') v_{\text{ext}}(\mathbf{r}',t') \tag{3.2}$$

In the following sections, I will describe how we can use electronic structure theory to calculate both the macroscopic and the microscopic dielectric response of a material. I will also describe how we can use the dielectric function to calculate the optical absorption, and comment on the differences between the 2D and 3D cases.

3.1 Modeling response in DFT

We saw in the previous chapter that the essential properties of condensed matter can be described through the electronic density. The goal is therefore to describe how the electronic density changes on the application of an external field. For small fields we would expect a linear relationship between the applied potential and the change in the density, and the most general way of writing such as relationship is

$$\delta n(t) = \int \mathrm{d}t' \int \mathrm{d}\mathbf{r}' \, \chi(\mathbf{r},t;\mathbf{r}',t') v_{\text{ext}}(r',t'). \tag{3.3}$$

The object χ is the density-response function which shows how the density at (r,t) varies due to an external potential at $\mathbf{r}', t'$.

In the Kubo linear response framework[35], the first order change in the density due to an external perturbation H' is found as

$$\delta\langle \hat{O}(t)\rangle = -i \int_{t_0}^{\infty} \mathrm{d}t' \theta(t-t') \left\langle \left[\hat{O}(t), \hat{V}(t')\right]\right\rangle_0 \tag{3.4}$$

The Heaviside step function ensures that the response of the system obeys the causality principle, meaning that the response of the system at a time t does not depend on the perturbation at future times t', and $\langle\cdot\rangle_0$ denotes the expectation value of an operator with respect to the unperturbed system. Comparing equations (3.3) and (3.4), we see that we must have

$$\chi(\mathbf{r},t;\mathbf{r}',t') = -i\theta(t-t') \left\langle [\hat{n}(\mathbf{r},t), \hat{n}(\mathbf{r}',t')]\right\rangle_0 . \tag{3.5}$$

In DFT, accessing the density response function is difficult, but we can more easily access the non-interacting response function χ^0. This is the response the system would have if the electrons were non-interacting, which is exactly the case for the fictitious particles considered in the Kohn-Sham framework. Fortunately, the interacting and non-interacting response functions are related through the Dyson equation[36]

$$\hat{\chi} = \hat{\chi}_0 + \hat{\chi}_0(\hat{v} + f_{\text{xc}})\hat{\chi}, \tag{3.6}$$

where all quantities are understood as operators, and f_{xc} is the functional derivative of the exchange-correlation potential with respect to the density. In the random phase approximation (RPA)[37], the exchange-correlation kernel is neglected, and the interacting response function is given by

$$\hat{\chi} = \hat{\chi}_0 + \hat{\chi}_0 \hat{v} \hat{\chi} \tag{3.7}$$

The question then becomes how we calculate the non-interacting response function. Assuming homogeneity in time, so that the time dependence of the response function becomes $\chi^0(\mathbf{r}, t; \mathbf{r}', t') = \chi^0(\mathbf{r}, \mathbf{r}', t - t')$, we can Fourier transform in time to get the response function $\chi^0(\mathbf{r}, \mathbf{r}', \omega)$. This can be shown[38] to read

$$\begin{aligned}\chi^0(\mathbf{r}, \mathbf{r}', \omega) = \sum_{m,n} \sum_{\mathbf{k},\mathbf{q}} & \frac{f_{m,\mathbf{k}} - f_{n,\mathbf{k}+\mathbf{q}}}{\omega + \varepsilon_{m\mathbf{k}} - \varepsilon_{n,\mathbf{k}+\mathbf{q}} + i\eta} \\ & \times \psi^*_{m,\mathbf{k}}(\mathbf{r}) \, \psi_{n,\mathbf{k}+\mathbf{q}}(\mathbf{r}) \, \psi_{m,\mathbf{k}}(\mathbf{r}') \, \psi^*_{n,\mathbf{k}+\mathbf{q}}(\mathbf{r}')\end{aligned} \tag{3.8}$$

Here $f_{n,\mathbf{k}}$ are the occupation numbers of the system, satisfying $\sum_{n,\mathbf{k}} f_{n,\mathbf{k}} = N$, where N is the number of electrons in the system, $\psi_{m,\mathbf{k}}$ are Kohn-Sham eigenfunctions, $\varepsilon_{m,\mathbf{k}}$ are the corresponding eigenenergies and η is an infinitesimal introduced to ensure the convergence of the Fourier transform.

As we are dealing with a periodic crystal, it must be the case that $\chi^0(\mathbf{r}, \mathbf{r}', \omega) = \chi^0(\mathbf{r} + \mathbf{R}, \mathbf{r}' + \mathbf{R}', \omega)$ for any two lattice vectors $\mathbf{R}$ and $\mathbf{R}'$. In this case, it is more convenient to express χ^0 in a plane wave basis, which finally gives the non-interacting response function in reciprocal space[37, 39]

$$\begin{aligned}\chi^0_{\mathbf{G}\mathbf{G}'}(\mathbf{q}, \omega) = 2 \sum_{m,n} \sum_{\mathbf{k},\mathbf{q}} & \frac{f_{m,\mathbf{k}} - f_{n,\mathbf{k}+\mathbf{q}}}{\omega + \varepsilon_{m\mathbf{k}} - \varepsilon_{n,\mathbf{k}+\mathbf{q}} + i\eta} \\ & \times \left\langle \psi_{m\mathbf{k}} \middle| e^{i(\mathbf{G}+\mathbf{q})\cdot\mathbf{r}} \middle| \psi_{n,\mathbf{k}+\mathbf{q}} \right\rangle \left\langle \psi_{n,\mathbf{k}+\mathbf{q}} \middle| e^{i(\mathbf{G}'+\mathbf{q})\cdot\mathbf{r}} \middle| \psi_{m\mathbf{k}} \right\rangle\end{aligned} \tag{3.9}$$

From this we can obtain the interacting density response function via Eq. (3.7), and the inverse dielectric function can then be found as

$$\epsilon^{-1}_{\mathbf{G}\mathbf{G}'}(\mathbf{q}, \omega) = \delta_{\mathbf{G}\mathbf{G}'} + \nu \chi_{\mathbf{G}\mathbf{G}'}(\mathbf{q}, \omega) \tag{3.10}$$

The total potential is given by

$$v^{\mathrm{tot}}_{\mathbf{G}}(\mathbf{q}, \omega) = \sum_{\mathbf{G}'} \epsilon^{-1}_{\mathbf{G}\mathbf{G}'}(\mathbf{q}, \omega) v^{\mathrm{ext}}_{\mathbf{G}'}(\mathbf{q}, \omega), \tag{3.11}$$

and we can thus describe how the system will respond to any applied field.

3.2 The macroscopic dielectric function

We also see that the structure of $\epsilon_{\mathbf{GG'}}$ means that the total potential will have rapid variations on the scale of the unit cell, even if a slowly varying external potential is applied. These are the local field effects[**!!!**].

We can link the microscopic picture and our macroscopic experiments by taking the average of the total potential over a single unit cell. The macroscopic total potential is then linked to the external potential via $V^{\text{tot}}(\mathbf{q},\omega) = \epsilon^{-1}_{\mathbf{00}}(\mathbf{q},\omega)V^{\text{ext}}(\mathbf{q},\omega)$, from which we see that the macroscopic dielectric function in three dimensions, $\epsilon_{\text{M,3D}}$, is given by

$$\epsilon_{\text{M,3D}}(\mathbf{q},\omega) = \frac{1}{\epsilon^{-1}_{\mathbf{00}}(\mathbf{q},\omega)}. \tag{3.12}$$

It is important to note that $\epsilon_{\text{M,3D}} \neq \epsilon_{\mathbf{00}}$, since off-diagonal elements of $\epsilon_{\mathbf{GG'}}$ can contribute to the head when the matrix is inverted.

For the case of two-dimensional materials, this procedure for extracting the macroscopic dielectric function fails. This is because of the averaging procedure used to link the macroscopic and microscopic dielectric functions, and because of the way we represent 2D layers. Typically, we represent 2D crystals as 3D crystals with a very large out of plane lattice constant, which lets us avoid spurious interlayer interactions and hybridization between the different layers. The electronic density and response are however confined to the 2D layer, and when the average of the microscopic dielectric function is taken over the whole unit cell, most of the contribution comes from the vacuum between layers, where there is no response. From this we would thus conclude that there is essentially no screening of charges, regardless of $\mathbf{q}$[40].

The natural approach to dealing with this issue is to limit the out of plane average to a certain thickness, instead of averaging over the whole unit cell[41]. Doing this yields the quasi-2D analogue of the 3D dielectric function, which links the in-plane total potential to the in-plane external potential. In the limit of a purely 2D material, the macroscopic dielectric function is linear in q and has the form

$$\epsilon(\mathbf{q},\omega) = 1 + 2\pi\alpha(\omega)q \tag{3.13}$$

We see that as $q \to 0$, $\epsilon \to 1$, meaning that there is no long-range screening in two dimensions. Intuitively, this makes sense: when two charges in a 2D material are well separated, almost all of the field lines between them will lie outside the 2D layer, where there is no screening.

The advantage of the functional form of Eq. (3.13) is that it is possible to analytically perform the Fourier transform and derive the real-space screened interaction[42]

$$W(\mathbf{r}) = \frac{1}{4\alpha}\left[Y_0(\rho) - H_0(\rho)\right]_{\rho=r/2\pi\alpha}, \tag{3.14}$$

Where Y_0 is a Bessel function of the second kind, and H_0 is a Struve function. This is a very different functional compared with the 3D screened Coulomb interaction which generally has the form $W(\mathbf{r}) \sim \frac{1}{\epsilon r}$. Eq. 3.14 has the following limiting behaviors

$$W(\mathbf{r} \to \infty) \sim \frac{1}{r}$$
$$W(\mathbf{r} \to 0) \sim \log(r),$$

And thus shows the expected lack of screening at long distances, and a logarithmic divergence at the origin.

3.3 Optical Properties

We can also use the dielectric function to determine the optical absorption of a material. Within the RPA, the absorption in a given direction, $\hat{\mathbf{e}}$, is given by[16]

$$\mathrm{ABS}_{\hat{\mathbf{e}}}(\omega) = \lim_{q\to 0} -\frac{4\pi}{q^2}\mathrm{Im}\left(\chi^0_{\mathrm{M}}(q\hat{\mathbf{e}},\omega)\right), \tag{3.15}$$

where χ^0_{M} is the macroscopic non-interacting polarizability. In three dimensions, we can combine Eqs. (3.7) and (3.10) to obtain $\epsilon_{\mathrm{M}}(\mathbf{q},\omega) = 1 - \frac{4\pi}{q^2}\chi^0_{\mathrm{M}}(q,\omega)$, from which we immediately see that

$$\mathrm{ABS}_{\hat{\mathbf{e}},3\mathrm{D}}(\omega) = \lim_{q\to 0}\left(\epsilon_{\mathrm{M}}(q\hat{\mathbf{e}},\omega)\right). \tag{3.16}$$

As we saw in the previous section, the 2D macroscopic dielectric function is ill-defined, but the polarizability retains its structure. To see this, we can look at the $\mathbf{q} \to 0$ limit of $\chi^0_{\mathbf{G}\mathbf{G}'}$. Using $\mathbf{k}\cdot\mathbf{p}$ perturbation theory, we find that in this limit, the matrix elements in Eq. (3.9) go as

$$\left\langle \psi_{m,\mathbf{k}} \middle| e^{i\mathbf{q}\cdot\mathbf{r}} \middle| \psi_{n,\mathbf{k}+\mathbf{q}} \right\rangle \approx \frac{\langle \psi_{m,\mathbf{k}} | \hat{\mathbf{p}} | \psi_{m,\mathbf{k}} \rangle}{\varepsilon_{m\mathbf{k}} - \varepsilon_{n,\mathbf{k}+\mathbf{q}}} \cdot \mathbf{q} \tag{3.17}$$

For semiconductors, the energy difference in the denominator will always be non-zero. We therefore have that as $\mathbf{q} \to 0$, the matrix elements are $O(q)$, and χ^0 goes as $O(q^2)$. The limit in Eq. (3.15) is thus well-defined, and we have a valid expression for the optical absorption also in two dimensions.

CHAPTER 4

The computational 2D materials database

In the preceding two chapters, we have seen how we can calculate a wide variety of properties of any material based solely on knowledge of the atomic positions. We have also seen how two-dimensional materials are different from three-dimensional materials, at least with regards to their dielectric screening properties. Using this knowledge we can systematically calculate the properties of many materials.

As we saw in chapter 1, 2D materials have a number of unique properties, and more than fifty compounds have been synthesized as monolayers. Many more compounds are predicted to exist, but so far no systematic study has been undertaken to explore these properties, or to map out this materials space.

We have set out to perform just such systematic a study, starting with the known 2D structures. The most important figure in the genesis of the C2DB is shown on Fig. 4.1. This illustrates the workflow we have developed to characterize the structural, thermodynamic, elastic, electronic, magnetic, and optical properties of any 2D material, starting with determining just which structure we should be looking at. The following two sections will explain the left and the right hand side of the figure using illustrative examples, and will go into the reasoning behind the choices we have made in developing the workflow. A great deal of time will be spent dealing with stability issues, as it is our stability analysis which makes us confident that we are working with real materials, rather than abstract atoms arranged in space. After explaining how we can calculate the properties of 2D materials, the final section of this chapter shows some examples of scientific insights we have gained from the database, as well as listing some materials which are potentially of interest for further study.

Before moving on, the reader should note two things. Firstly, this chapter is intended to both summarize and complement the work described in Paper I. For a comprehensive overview of the work, the reader should look there.

Secondly, since the publication of Paper I, we have completed calculations for many new materials and released a new version of the database, version 18.09. This brings the total number of materials studied from 1900 to 3000, and the total number of

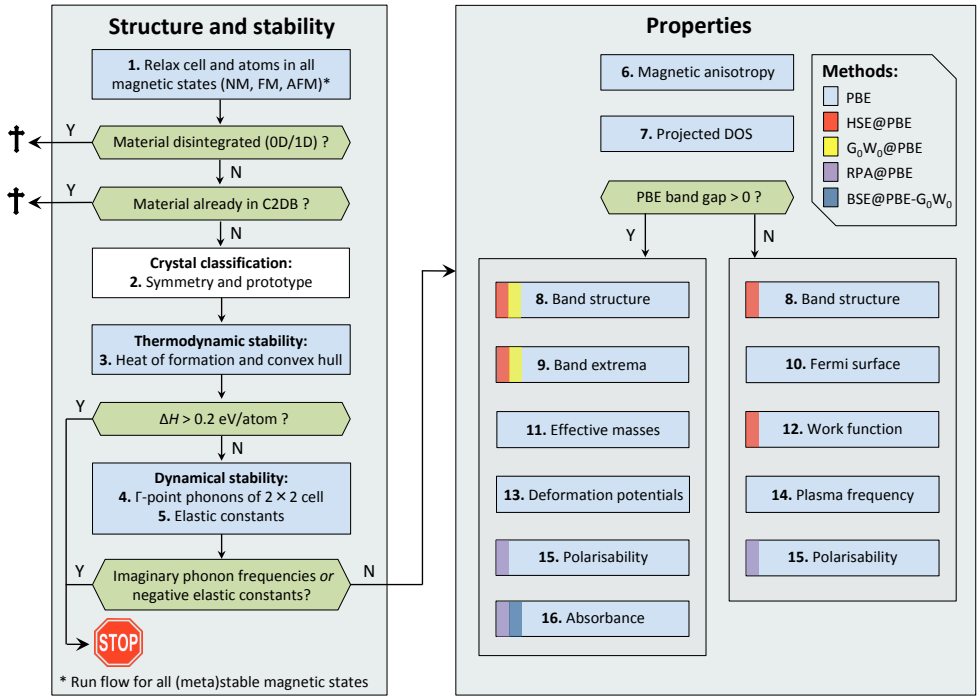

Figure 4.1: The workflow used to generate the structures in the C2DB and to calculate their properties.

stable materials found to 550. When we quote results from full the database, they will refer to the version with 3000 materials, unless otherwise stated.

4.1 Generating novel 2D structures

The first step in the systematic investigation of 2D materials is the question of how to generate novel 2D structures, that is the left hand side of 4.1 In principle, using electronic structure methods, it should be possible to calculate the properties of arbitrary arrangements of atoms. The probability of any one of these arrangements being physically meaningful is very small, and the probability of discovering a novel layered or two-dimensional structure is even smaller.

The guiding idea behind the initial generation of structures is that similar materials are likely to have similar properties. Therefore, if we start from the existing set of

known 2D materials, and perform small changes, we are likely to arrive at another 2D material. The most obvious variation we can perform is varying the composition: for example, if there is a known 2D material with composition MX_3, with M a metal atom and X a halogen atom, then the same structure with a different halogen atom, MY_3, is potentially of interest. We term this approach to generating materials combinatorial lattice decoration.

To generate structures, we therefore base our exploration on known layered and 2D materials. For these crystals, we have chosen to substitute materials from within the same group in the periodic table (for the nonmetallic elements), or across all the transition metals. This approach seems chemically reasonable; an alternative approach could have been to use a scale of chemical similarity such as the Pettifor scale[43] or a modified version[44] to determine which substitutions should be attempted.

This approach of lattice decoration will undoubtedly lead to structures which are not synthesizable, or which are unstable (see Sec. 4.1.1), but it will also lead to some stable structures with interesting properties. The great advantage of performing computational materials' discovery is that it is significantly faster and cheaper than working experimentally. This means that we can use *in silico* discovery to guide experimental discovery, by identifying materials or classes of materials with useful properties. In this way, we can create a map for the space of materials properties, and hopefully put some crosses on it to say "X marks the spot".

From a perspective of understanding correlations and trends, performing the substitutions and calculating properties for entire, closed classes of material is very useful. This lets us make general statements about the behavior of one entire class compared with another, or about the behavior of one composition across different classes. The complete, structured and consistently calculated data are also an ideal playground for data mining and data driven approaches to materials modeling. See Sec. 4.3.2 for more detail on this.

Once we have an initial structure, we relax it, by allowing the atomic coordinates and the lattice parameters to vary, and finding the nearest local energy minimum with respect to the atomic positions and the atomic parameters. This accounts for the different sizes of the substituting, atoms, as well as the different bond angles of the systems.

To keep track of the different phases we investigate, we label each material according to a representative material with the same crystal structure, as will be described in section 4.1.2. An subset of the representative structures is shown in Fig. 4.2

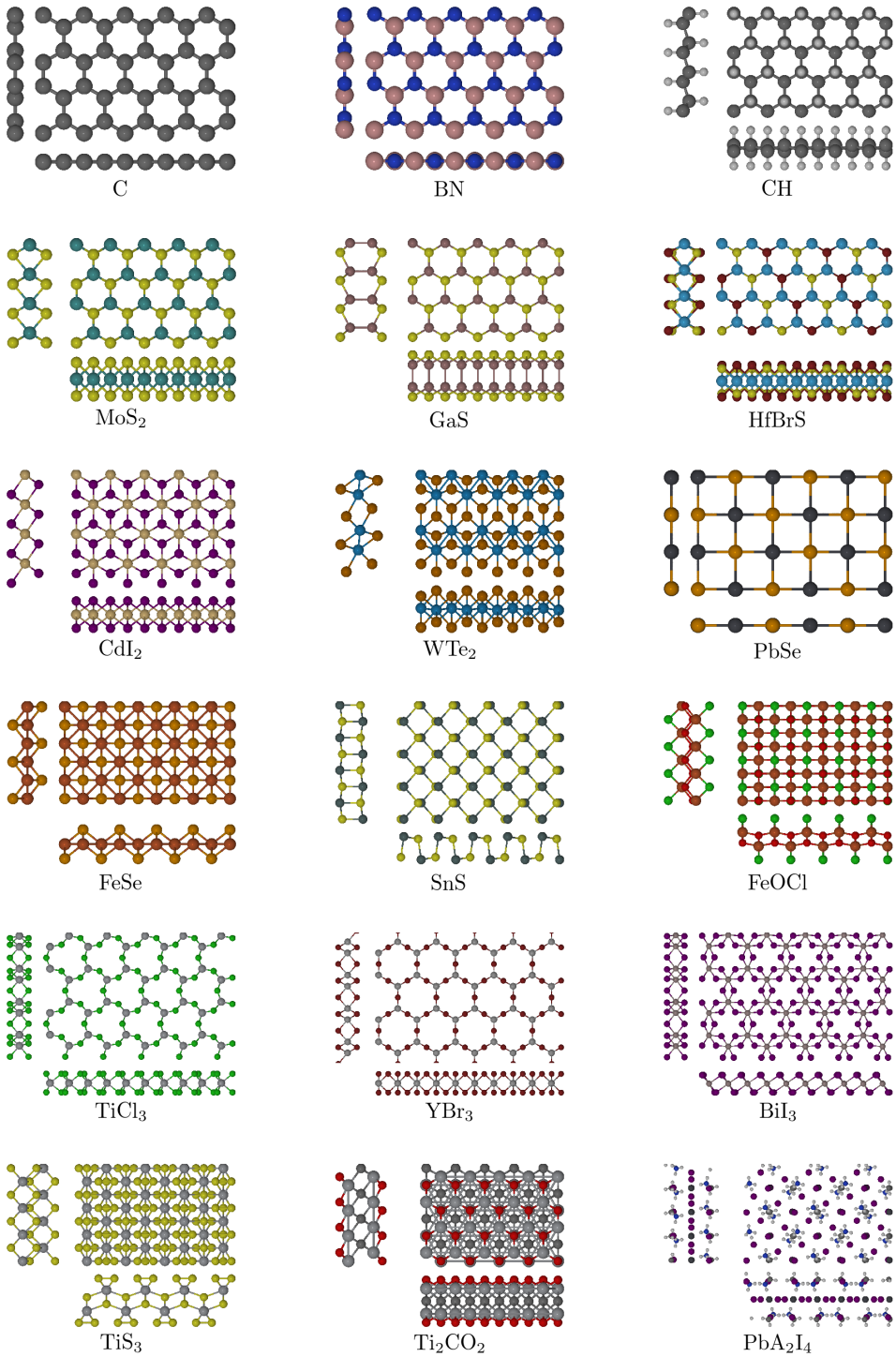

Figure 4.2: A subset of the different prototypes in the C2DB.

4.1.1 Stability

The most important decision we make with respect to a given structure is whether or not we consider it stable – for it is this winnowing of the stable structures from the unstable which links our computationally derived novel structures with the outside world. A useful way looking at the stability is to look at local and global stability, namely stability with respect to local distortions – dynamical stability – and stability with respect to global reconfiguration of the atoms in the structure – thermodynamic stability. In the following, I will explain the two different axes, and describe the stability scale we use to classify the stability of a 2D material.

As described in the previous section, the first thing we do when we consider a new 2D structure is to relax the atomic positions and the lattice parameters. We would therefore expect that the final structure is in a local minimum of the potential energy surface, and no local distortions would be energetically favorable. The reason that we need to consider the dynamical stability is that the initial relaxation is constrained to preserve the symmetries of the original structure. This means that our relaxation only guarantees that we are on a saddle point of the potential energy surface, and a symmetry-breaking distortion of the structure which lowers the energy would not be discovered. An example of this is the case of WTe_2 which undergoes a distortion from a hexagonal structure, as illustrated in Fig 4.3.

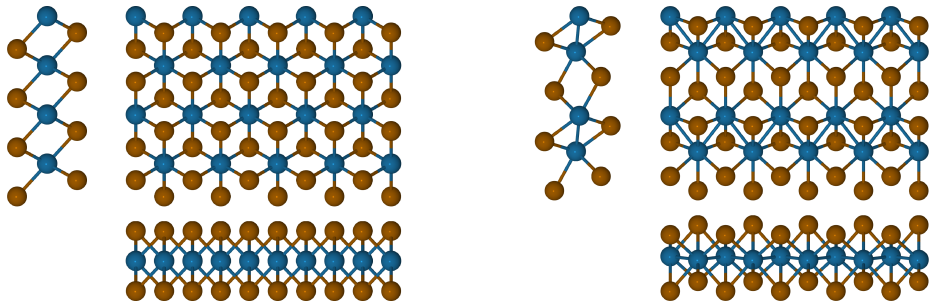

Figure 4.3: The distortion of WTe_2 from the T phase (left) to the T′ phase (right).

To make it more likely that the structure we have found truly is at a minimum of the potential energy surface, we calculate the Γ-point phonons of the 2×2 cell. To do this, we successively displace every atom in the primitive cell along the three coordinate axes, and calculate the forces on all the other atoms. In the basis of atomic displacements, these forces express the curvature of the potential energy surface. By diagonalizing the force matrix, we obtain the principal curvatures of the potential energy surface in all directions, and the normal modes which describe the motion of the atoms along these directions. If any of the principal curvatures is negative, the structure can gain energy by moving along the corresponding normal mode, and the structure is therefore unstable. Fig. 4.4 shows the phonon energies of WTe_2 in the

CdI_2 phase (left panel of Fig. 4.3). As expected, we see modes with negative energy, indicating that this configuration of atoms is not locally stable.

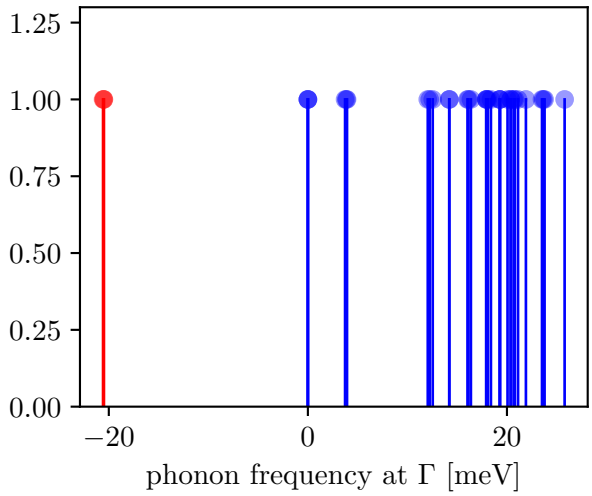

Figure 4.4: The phonons of WTe_2 in the CdI_2 phase at the zone center and at the zone boundary.

Along with stability towards local distortions, global thermodynamic stability is also an important factor. A first approximation to this is the heat of formation of the structure, which compares the energy of the structure with the energy of the most stable phases of its constituent elements. If the heat of formation is positive, the energy of the structure is higher than that of the constituent elements, and the material will be both difficult to synthesize from elemental precursors, and, if formed, likely to dissociate back into the elemental states. However, the heat of formation does not tell the full story of the thermodynamic stability: It is not sufficient that a material be stable with respect to the elemental references: to be truly stable, the material should also be stable with respect to every other arrangement of the same atoms. We can quantify this by comparing the energy of the structure with respect to all the competing phases of the structure. The relevant quantity is the convex hull of the energies of the competing phases; for any composition it gives the energy of the optimal linear combination of alternative phases. An example of a convex hull is shown in Fig. 4.5, for iron-selenium compounds. We see that for $FeSe_3$ in the TiS_3 prototype, the heat of formation is negative, and there is no structure with the same stoichiometry and a lower heat of formation. However, the material is unstable, as the total energy would be lowered if the following reaction took place $FeSe_3 \longrightarrow FeSe_2 + Se$. With respect to the convex hull, the most stable 2D material in this class has AB stoichiometry, as it actually lies on the hull.

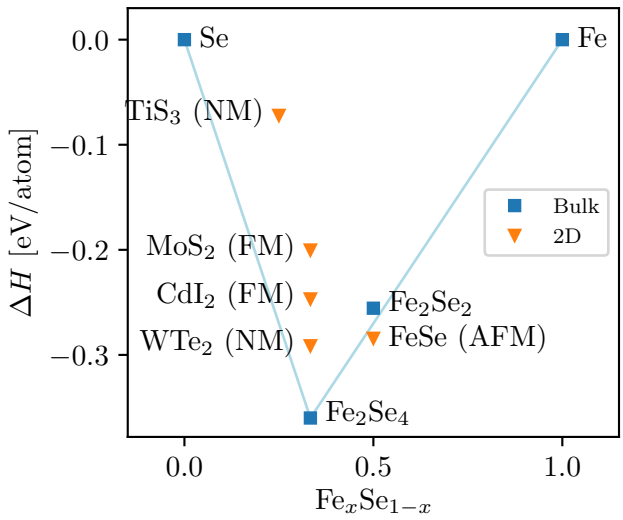

Figure 4.5: An example of a two-component convex hull, with the bulk reference structures in blue, and the 2D materials in orange. The blue line indicates the convex hull of the energies of the reference states.

Ideally, we would consider only dynamically stable materials lying on the convex hull. This criterion is fulfilled by approximately 7% of the materials studied. However, such a criterion is too strict.

It is true that given sufficient time, we would expect to observe only the ground state atomic configuration, i.e. the *global minimum* of the potential energy surface. This might be a different phase with the same stoichiometry, or it might involve phase separation into two different phases lying on the convex hull. The crucial issue is one of time scales. If the length of time it takes for a material to move from its local minimum to the global minimum is longer than the time we are concerned with, then we can treat the material as stable. We call this property of being stable for long enough metastability, and a classic example of this is diamond. The most stable phase of elemental carbon under standard conditions is graphite, but nonetheless diamond is easily accessible for both commercial and technological purposes, and it would be a mistake to exclude it from consideration just because a more stable phase exists.

Looking for atomic configurations which lie in local minima of the potential energy surface is therefore sufficient for our considerations. This is also why investigating the dynamical stability is so important, for we would expect local distortions (if any) to take place on short timescales, as they involve moving downhill on the potential energy surface towards the local minimum, and therefore have essentially no energy barrier. Nonetheless, even dynamically unstable materials can sometimes be stabilized by

substrate interactions, or by encapsulation in other materials such as boron nitride. A striking example of this is the prediction of two-dimensional phases of ice encapsulated in graphene[45].

In addition to the possibility of stabilization, we must consider the accuracy of the calculations. We know that PBE formation energies have an error of up to 0.2 eV/atom[46], and there are also errors in our determination of the convex hull. To account for these effects we therefore devise a stability scale for both thermodynamic and dynamical stability, and classify each material as having "HIGH", "MEDIUM" or "LOW" stability along each axis. The choices we have made defining each axis are as follows, where the minimum eigenvalue of the force matrix ω^2_{min} has units of eV/Å, and the heats of formation have units of eV/atom:

	LOW	MEDIUM	HIGH
Dynamic stability	$\omega^2_{\text{min}} < -2$	$-2 < \omega^2_{\text{min}} < 0$	$\omega^2_{\text{min}} \geq 0$
Thermodynamic stability	$\Delta H_{\text{f}} > 0.2$	$\Delta H_{\text{f}} < 0.2$	$\Delta H_{\text{hull}} < 0.2$

In addition to these requirements, for a material to be classed as dynamically stable, we also require that it be stable under mechanical strain. Applying these criteria to all the materials included in the C2DB v. 18.09 gives the distribution of stabilities shown in table 4.1. We see that the approach of combinatorial lattice decoration has resulted in almost 20% of the structures investigated being classed as highly stable on both axes, and thus potentially synthesizable.

Thermodynamic	Dynamic stability			
stability	LOW	MEDIUM	HIGH	Total
LOW	**6.9%**	**3.5%**	**2.0%**	12.3%
MEDIUM	**17.8%**	**12.7%**	**8.6%**	39.1%
HIGH	**9.8%**	**20.0%**	**18.9%**	48.6%
Total	34.4%	36.2%	29.4%	

Table 4.1: The materials in the C2DB distributed over the nine stability categories defined by the three levels of dynamical stability and thermodynamic stability. The color indicates the overall stability of the materials, which is defined as the lower of the two separate stability scales.

To complement the tabulation of the stability levels, we can also visualize the distribution of all the materials in the database along the two stability axes, which is done on Fig. 4.6. From this we see that there is generally a correlation between dynamical and thermodynamic stability: the most dynamically stable materials are also more

likely to be thermodynamically stable. It is also encouraging to see that most of the materials with known layered parent structures have a formation energy above the convex hull close to zero, indicating that the interlayer interactions are weak.

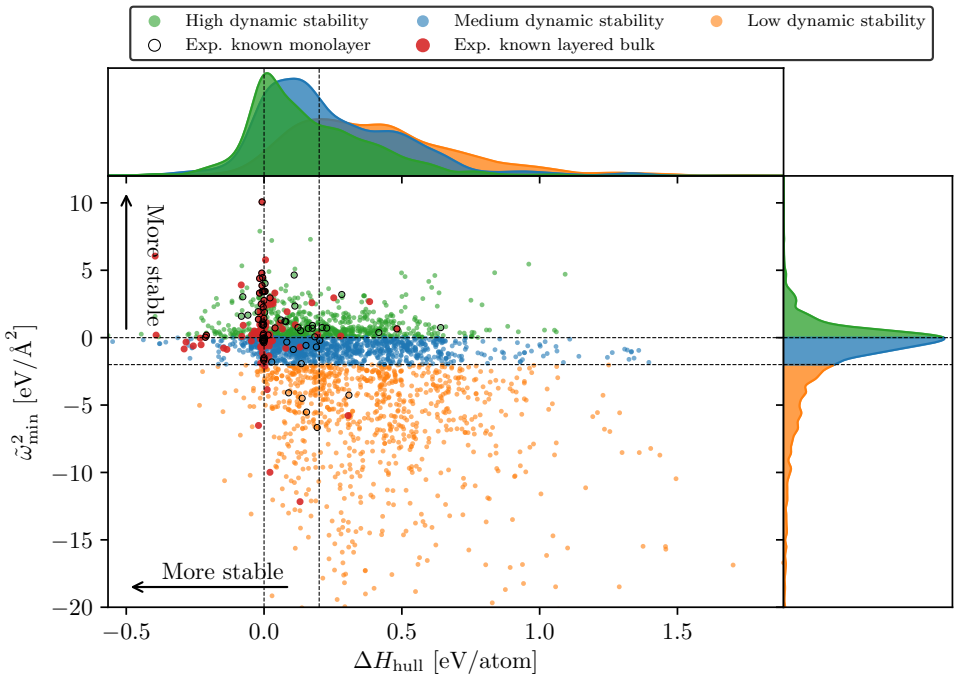

Figure 4.6: The distribution of the materials in the C2DB v. 18.09 according to the minimum eigenvalue of the hessian and the energy above the convex hull. The materials are colored according to their dynamical stability level, and the experimentally known monolayers and layered bulk structures are highlighted.

It should be noted that the stability analysis we do here only concerns itself with zero-temperature stability of the structure in isolation. This means that we are missing two effects which are relevant to the stability of any synthesized material. The first is the role of entropic effects at finite temperatures, where we should be considering changes in free energies rather than changes in total energies. The second effect is that of stability in an environment: Interactions with the environment, such as oxidation, reduction or the leaching away of metal atoms by a solute can all impact whether or not a material is suitable for a given purpose. The stability levels we define here should thus be seen as a guideline, rather than an absolute statement of fact.

Overall, by far the most time – certainly human time, and potentially also CPU time – has been spent in relaxing structures from an initial state and in performing the stability analysis. The result of this is that we can be fairly certain that we are working with physically reasonable and potentially synthesizable structures. Once we have completed the stability analysis do we move on to calculating the properties of the material – and for unstable materials (those with low stability on either stability axis), we do not calculate any properties.

The first thing we do is to class the materials into prototypes according to some symmetry criteria. This is described briefly in Paper I, but since then we have developed an improved method of prototype determination, which will be described in the following section.

4.1.2 Crystal Structure Prototypes

From an abstract perspective, the crystals we are considering can all be classed according to their space group, which reveals all the symmetry transformations that map the crystal onto itself.

The prototype requirement we have considers only the space group of the atoms, meaning that structures which intuitively seem wildly different could be given the same prototype. In the first classes of materials we considered ($\sim$ 1900 structures), this occurred very infrequently, and was mainly due to some materials having extension out of plane, while others did not. Figure 4.7 shows the case of hBN and GaS, which both have reduced stoichiometry AB and space group P$\bar{6}$m2. To account cases for these in a first approximation, we have therefore also classed materials as 2D or quasi-2D, depending on their out-of-plane extension.

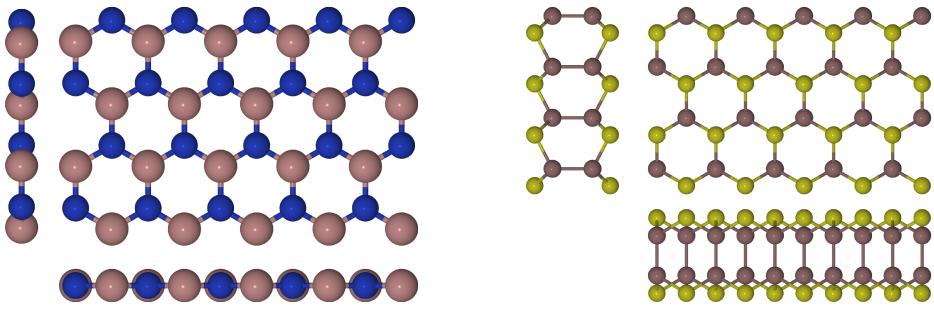

Figure 4.7: The structures of hBN and GaS, both with the space group P$\bar{6}$m2. Visual inspection shows that the in-plane structures are the same, and the mirror plane at $z = 0$ maps all atoms of BN to itself, and all atoms of GaS to an equivalent atom.

A better approach to symmetry classification is to look at the site symmetry group of each atom. In the case of BN, each atom lies in a horizontal mirror plane, and is thus mapped to itself under a reflection in this plane. On the other hand, for GaS, none of the atoms lie on a mirror plane, and under a reflection in the mirror plane, they are mapped to equivalent atoms, rather than to themselves.

The formalization of this idea leads us to look at the conjugate subgroups of the space group, and gives us the Wyckoff sites of the crystal. These have been tabulated for every space group[47]. By specifying which Wyckoff sites are occupied, we therefore arrive at a full symmetry classification of the system. One thing to note in this respect is that sometimes a given set of occupied Wyckoff sites is related to another set through a rigid transformation (rotation or translation). This means that for a given crystal, a different choice of unit cell could result in a different set of Wyckoff sites being occupied. A method is therefore needed to identify these equivalent sets of occupations, and this was provided in [48].

Including the Wyckoff positions in our analysis, we are able to distinguish not only the case of BN and GaS highlighted above, but also that of graphane and GaSe shown in Fig. 4.8.

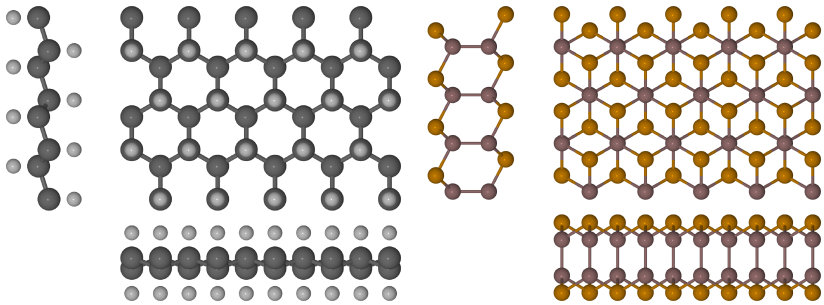

Figure 4.8: The structures of CH and GaSe, both with the space group $P\bar{3}m1$.

Both structures again have space group $P\bar{6}m2$, but for graphane, the occupied Wyckoff positions are d and d, while for GaSe they are c and d. Intuitively, these different positions capture the fact that for GaSe, identical metal atoms are located directly above one another, while for the CH prototype, we have inequivalent atoms above one another.

The key feature of the symmetry-based prototype analysis, is that we can scale the unit cell of the crystal, and vary all the free parameters in the Wyckoff sites without affecting the symmetries. This can be both an advantage and a disadvantage – in some cases, these transformations can yield structures which are sufficiently different that at first glance they should belong to different prototypes. A second point is that the presence or absence of a symmetry is inherently a discontinuous property. Even with a large tolerance parameter, there will still be arbitrarily similar structures which

fall into different symmetry classes. Due to these issues, a natural question to ask is what the prototype determination would look like if an different method were used, one which depends only on the positions of the atoms, and not on the symmetries.

To capture this notion of intuitive similarity, a metric for 3D and 2D periodic structures has recently been proposed[49], which calculates the atomic displacements between two systems, taking account the periodicity of the crystal. Using this metric, we can calculate the distance between a selection of structures with the AB stoichiometry, and based on this distance, we can cluster all the structures into different classes, using a hierarchical clustering analysis[1]. The distance matrix and resulting dendrogram are shown in Fig. 4.9. The dendrogram is created by initially considering each structure to be its own cluster, and then successively merging the two closest clusters, keeping note of what the cluster-cluster distance was at the point of merging.

The structure of the data is also visible in the distance matrix on the bottom, where we observe darker squares along the diagonal of the matrix, indicating that the matrix has been ordered so that similar structures are close to one another.

From the figure, we see that there is generally good agreement between the symmetry-based prototyping and the atomic distance measure: If we cut the dendrogram at the height indicated by the dashed line, we end up with seven clusters. For seven of these, the cluster only contains materials assigned the same symmetry-based prototype; the remaining cluster consists of small symmetry distortions of the same template. Each different symmetry prototype lies entirely within the same cluster, with the exception of FeSe which has been split in two. This agreement between the symmetry-based prototype assignment and the distance-based clustering is, as it indicates that the prototype assignment we perform is meaningful, and reflects some underlying structure in the data.

To evaluate the performance of the clustering more systematically, we can compare the distance between each pair of structures, and the height at which the two are merged in the hierarchical clustering. This last quantity is known as the cophenetic distance[50], and the correlation between the original distance and the cophenetic distance is the cophenetic correlation coefficient. For the clustering shown in figure 4.9, this value comes to 0.84, again illustrating that there is a good match between the geometric similarity, and the clustering we have performed.

[1] Completely flat structures are not included, and neither are prototypes with only one or two structures in the database

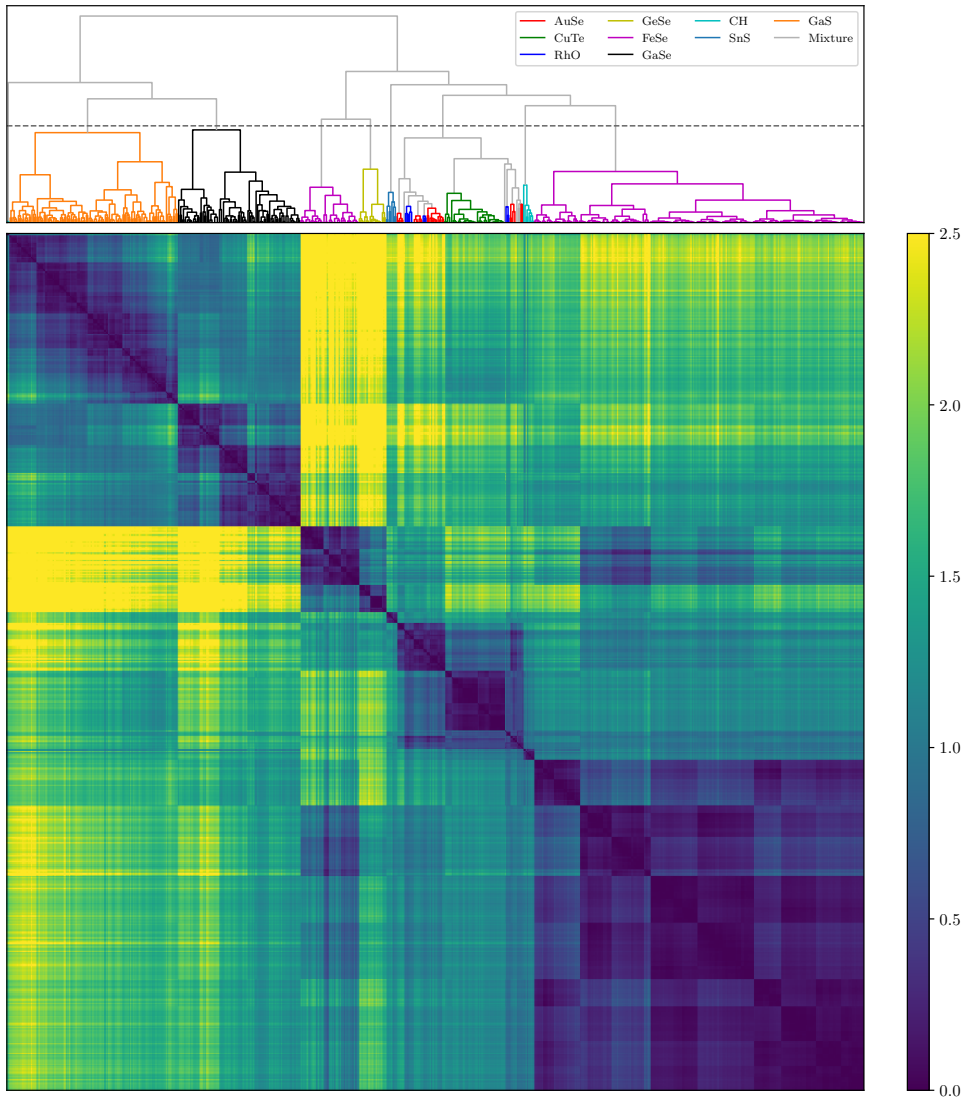

Figure 4.9: The 2D-periodic RMSD between structures in the AB prototype. Each (i, j) cell in the bottom panel is shaded according to the distance between structures i and j. The structures have been ordered according to the clustering induced by the dendrogram in the upper panel, so that similar materials are close to one another, and the dark squares on the diagonal reveal clusters of similar materials. The links in the dendrogram have been colored according to the prototype of each structure. If more than one prototype is present in a cluster, the links are colored grey.

4.2 Calculating the properties of 2D materials

In this section, I will explain the philosophy behind our approach to calculating materials properties of 2D materials (the right panel of Fig. 4.1), and the reasoning behind the choices we have made. I will do this through the illustrative example of the effective masses. For the complete details of how we calculate all the various quantities shown in the right panel of Fig. 4.1, we refer to Paper I, which extensively documents and validates the calculations we have performed, as well as listing all the relevant parameters.

Frequently, we are interested in modeling the behavior of free carriers in solids, that is electrons in the conduction band or holes in the valence band. These carriers can be generated through photo-absorption processes, or through impurities in the crystal which donate or trap electrons. The population of carriers will live at the bottom (top) of the conduction (valence) band, and usually, interband tunneling and scattering for these carriers is small, so that when an external force is applied to the carriers, they will move along the dispersion curve of their band[51].

Close to a band minimum, the dispersion of a smooth band will be approximately parabolic, and in the simplest, isotropic case, the energy as a function of k around these points thus looks like $E(\mathbf{k}) = E_0 + \frac{1}{2}ck^2$ to lowest order, for some band curvature c. The dispersion relation of a free electron looks like $E(\mathbf{k}) = E_0 + \frac{k^2}{2m_0}$. Comparing these two expressions, we see that near the band edge, an electron behaves like a free electron, but with an effective mass given by

$$\frac{1}{m^*} = c = \frac{\partial^2 E}{\partial k^2}. \tag{4.1}$$

This means that we can consider the carriers to act as if they were in free space, but with an effective mass determined from the curvature of the band at that point. In a semi-classical picture, when a force is applied to the carriers, they obey Newton's laws, but with their mass given by the effective mass. The entirety of the band structure of the solid and the quantum mechanical nature of the problem has thus been abstracted away into one parameter.

Often, however, the situation is slightly more complex. The curvature in one direction can be different from the curvature in other directions, and the effective mass becomes an $N \times N$ tensor in N dimensions, rather than a scalar. In the semi-classical picture, this means that depending on which direction a force is applied in, the carriers will respond as if they had different masses.

The first step in calculating the effective mass is to find the band edges in the Brillouin zone. For 3D materials, just finding the band edge can be a challenge, as it requires a very fine k-point sampling throughout the entire Brillouin zone[52]. What is often done instead is to restrict the search to certain high-symmetry paths in the Brillouin zone, and look for the edges values there. In two dimensions, finding the band edges is a much simpler task, as the parameter space is much smaller. It is therefore not

too computationally costly to finely sample the entire Brillouin zone and find the true band edges. This also turns out to be necessary, as 15% of the semiconductors in the C2DB have at least one of their band edges away from a high-symmetry line. The upper two panels of Fig. 4.10 show the band structure and Brillouin zone of SnS in the GeSe structure, as well as where the band edges are located in the Brillouin zone. We see that in this case, both the valence band maximum and the conduction band minimum lie on a high-symmetry line, but neither lies on a high-symmetry point.

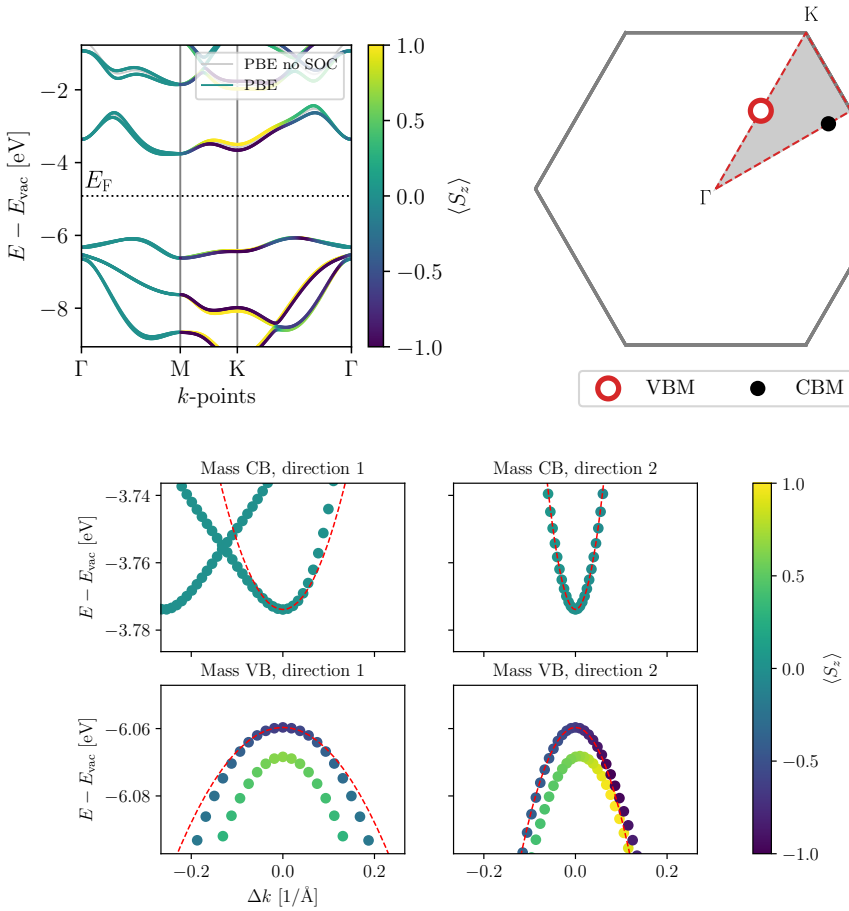

Figure 4.10: Band structure, Brillouin zone and band edge zoom for SnS in the GeSe prototype.

Once we have identified the points of interest, we need to calculate the curvature. We do this by calculating the eigenvalues on a fine k-point mesh in a circle around the

relevant point, with the radius of the circle chosen so that for a typical curvature, the energy differences are above the noise level of the calculation, but still within the harmonic regime. The energy scale of the dispersion within the circle is also small enough that the risk of "accidental" band crossings and degeneracies is minimized.

Once we have the energies, we can obtain the curvature (and thus the mass) by fitting a polynomial to them. It turns out that the procedure is less sensitive to the numerical details of the k-point sampling if we fit a third order polynomial, and then use that to extract the effective mass tensor. By diagonalizing the effective mass tensor, we can obtain the two principal axes of the (potentially anisotropic) masses, and to check the quality of the fit, we also calculate the exact eigenvalues along these two directions.

For the case of SnS in the GeSe structure, this is shown on the lower panel of Fig. 4.10, where we see anisotropic conduction and valence masses, as well as a Rashba-like band splitting in the conduction band.

The philosophy behind the calculation of the effective masses, and the database as a whole can be summarized in the following

- **Robustness**: The method used has to work across a wide range of different systems and situations, and fail only in the rarest of cases.
- **Simplicity**: The method should represent the simplest way of calculating the desired quantity from a DFT calculation. A simple but slow method is preferable to a complex but faster.
- **Accuracy**: The calculated value should quickly converge towards the true value as a function of some convergence parameter. There should be as few convergence parameters in the calculation as possible.

Overall, none of the above principles is revolutionary, but they all play a significant part in making the project management simpler. This will be described further in the following section.

4.2.1 Project Management

The number of different materials included in the C2DB, and the number of properties calculated for each material have meant that much time has been spent on managing calculations, and ensuring that they were proceeding as planned. A quick estimate of the number of calculations involved shows that at a minimum, a 200000 DFT calculations have been performed to reach the final database; not taking into account all the failed calculations along the way.

The most important tool in managing the project is the workflow illustrated in Fig. 4.1. Organizing calculations in this way has been a great help in structuring the process of calculating all the required properties. Ultimately, considering the full

set of calculations as a workflow or assembly line has meant the creation of scripts which (i) Take well-defined inputs; (ii) perform one simple calculation; (iii) produce a well-defined output, which can be consumed by subsequent tasks.

A lesson learned along the way is that it is necessary to automate as much of the calculation as possible, and only require human input in extraordinary cases. This means, for example, that the dependency graph implied by the workflow should be automatically enforced, rather than relying on people to submit the correct jobs at the correct time. It also means that the common failure cases of a calculation, namely lack of resources, should be dealt with automatically, rather than relying on human intervention. These considerations led to the creation of the `myqueue` tool, which is described in https://gitlab.com/jensj/myqueue.

Aside from the workflow and the calculations themselves, several steps are needed to generate the completed database file and the associated website. These are illustrated schematically in Fig. 4.11, and are separated into three separate phases, namely: running calculations, collecting data, and organizing its presentation. I will not go into detail of the different steps; the most important thing to note is that the last two phases should be carried out frequently, to ensure that they still work, even with new materials in the database or new tasks in the workflow.

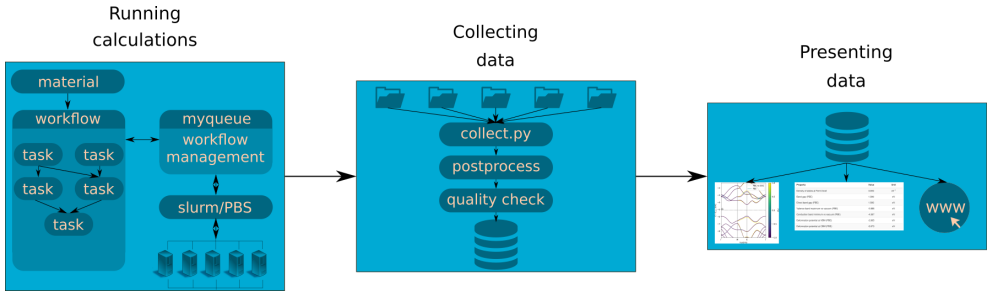

Figure 4.11: The steps involved in the creation of the database.

4.3 Using the database

The scientific value of the database extends far beyond merely being a reference work in which we can look up values if we ever need to. In this section I will highlight three ways in which we can use the database to advance materials science.

One advantage of having comprehensive data is that it is possible to evaluate the performance of simple descriptors over a wide range of materials, and we can begin to understand where simpler models break down. I will explore this theme more fully in Section 4.3.1

A second advantage of having all the properties calculated is that we can begin to explore structure-property and property-property relations, and thereby develop new descriptors for properties we are interested in. A surprising example of this is the agreement we observe between the G_0W_0 band gap of the 2D materials and GLLB-SC band gap; we observe that they scale in the same manner.

Finally, because we did not have a specific application in mind when creating the database, we can use it for many different applications. In particular the database can be used as the starting point for later screening studies, based on properties we have already calculated and descriptors we can derive from them. Some examples of interesting materials which might be found in this way are for novel high-mobility 2D materials, materials with magnetic properties, or with properties making them useful in tandem solar cells.

4.3.1 Evaluating the Performance of Descriptors and Simple Models

An advantage of having comprehensive data for a large and heterogeneous set of 2D materials is that it is possible to evaluate the performance of simpler models which work well in restricted situations. An example of this is in exciton binding energies, which are frequently described using a Mott-Wannier model (5.3), or the even simpler 2D hydrogen-like model[53]. For the systems which were originally considered, these models worked very well, but when they are applied to the full set of 2D materials, their performance drops significantly.

Figure 4.12 compares performance of the screened hydrogen model with the full solution of the BSE. The mean absolute deviation between BSE and the model is 0.28 eV for all materials and 0.20 eV for the subset of transition metal dichalcogenides. For very strongly bound excitons, it seems that the model systematically overestimates the binding energy, while for weakly bound excitons, it appears to underestimate the binding energy. We attribute the errors in the model to two sources

- *Weak screening*: If α^{2D} is small, the exciton becomes strongly localized and the orbital character of the states comprising the exciton plays a significant role.
- *Breakdown of the parabolic band approximation*: If the bands of the material are flatter in the vicinity of the minimum (maximum) than predicted by a parabolic band approximation, the exciton will be more delocalized in k-space than predicted by the Mott-Wannier model, leading to a stronger localization in real space, and thus a larger binding energy.

4.3.1.1 Band gaps and effective masses

A similar story holds for the relationship between band gaps and effective masses. Applying $\mathbf{k} \cdot \mathbf{p}$ perturbation theory, we can write down an expression for the band

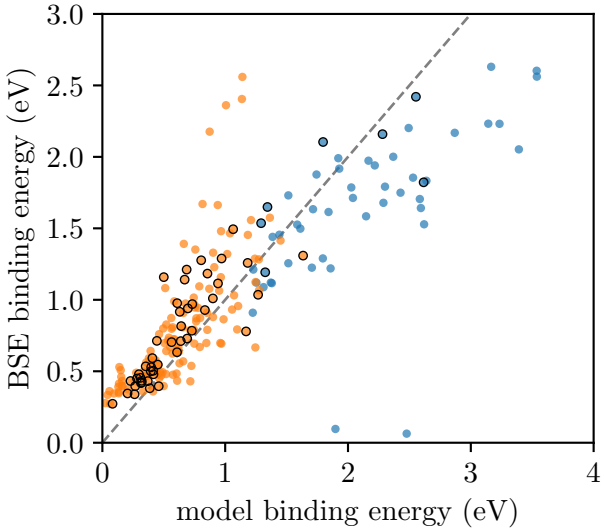

Figure 4.12: The performance of the simple hydrogen model for exciton in 2D materials evaluated on the original set of TMDCs (left) and on all the materials in the C2DB (right).

energy as a function of $\mathbf{k}$ near a band edge (which for simplicity is assumed to occur at $\mathbf{k} = \mathbf{0}$). This gives

$$\begin{aligned} E_{n,\mathbf{k}} &= E_{n,\mathbf{0}} + \frac{k^2}{2} + \sum_{m \neq n} \frac{|\langle u_{n,\mathbf{0}} | \mathbf{k} \cdot \hat{\mathbf{p}} | u_{m,\mathbf{0}} \rangle|^2}{E_{n,\mathbf{0}} - E_{m,\mathbf{0}}} \\ &= E_{n,\mathbf{0}} + \frac{k^2}{2} + \sum_{m \neq n} \frac{|\mathbf{k} \cdot \langle u_{n,\mathbf{0}} | \hat{\mathbf{p}} | u_{m,\mathbf{0}} \rangle|^2}{E_{n,\mathbf{0}} - E_{m,\mathbf{0}}} \end{aligned} \tag{4.2}$$

If the main contribution to this expression comes from just the valence and conduction band, we see that the band curvature should be inversely proportional to the band gap, and hence the band gap should be proportional to the effective mass. Additionally, if the corresponding matrix element $\langle \psi_c | \hat{p} | \psi_v \rangle$ is roughly constant across material classes, we would expect this relationship to be universal. This is the case for 3D direct band gap semiconductors, where a rule of thumb is that for carriers in the valence band[54],

$$\frac{1}{m^*} = \frac{1}{m_0} \left(1 + \frac{20 \text{ eV}}{E_\text{g}} \right) \tag{4.3}$$

Fig. 4.13 shows the inverse electron mass as a function of the inverse band gap for the semiconductors in the C2DB. Evidently, the clear correlation predicted by the

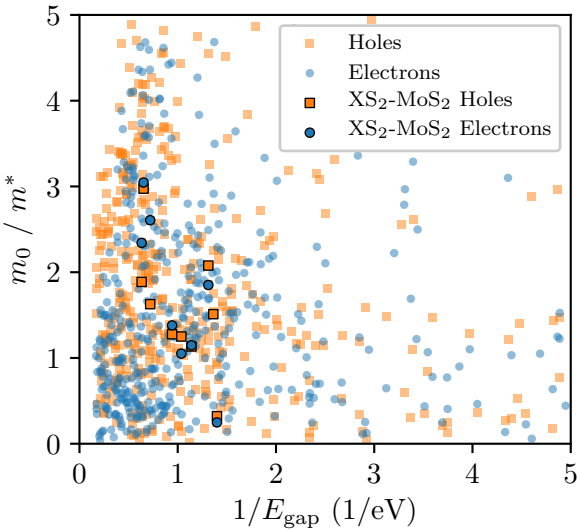

Figure 4.13: The inverse carrier as a function of the inverse band gap. A great deal of scatter is observed, rather than the predicted linear relationship. The linear correlation between the two. Materials with the formula XS_2 in the MoS_2 crystal structure are highlighted.

preceding analysis is not present. One of the main approximations used to predict the simple relationship 4.3 was to assume that the momentum matrix elements between conduction band states and valence band states are constant across material classes. To reduce the influence of this assumption, we can focus on materials of similar composition and crystal structure, where the approximation should hold. For these materials, there is a clearer relationship between the effective mass and the band gap, but it is by no means as simple as predicted by Eq. 4.3.

Overall, these examples show that while simple models work well for some cases, it is important to remember that they will break down at some point, and it is important to systematically check the validity of the assumptions behind the model.

4.3.2 Data-driven Analysis

As discussed in the beginning of chapter 2.2, the fundamental idea behind the atomic theory of materials is that all the properties of a material depend uniquely on the atomic structure of the material. Using electronic structure theory, we can access these properties, but at great computational cost.

One approach to finding correlations in data which has become immensely popular

in the last few years is known as machine learning. Outside of physics and materials science, machine learning and data analytics approaches have resulted in impressive performance in image recognition[55], speech recognition[56], self-driving cars[57] and games of strategy[58]. Within the field of materials science, there is also active research in applying machine learning methods [59, 60].

A full description of machine learning approaches is outside the scope of this thesis, so I will be extremely brief. The goal of a supervised machine learning process is to learn a function which maps some inputs to some target outputs. This requires a parameterized form of the target function, and an optimization routine which selects the best such parameters given a set of known $(\text{input}, \text{output})$ pairs.

The first step, before beginning with any kind of machine learning approach, is to find some way of representing a structure in a way that is useful for the problem at hand. Many different representations have been proposed, such as the coulomb matrix[61], the many-body tensor representation[62], the bag-of-bonds approach[63] or the smooth overlap of atomic potentials[64]. Ideally, a generalized representation of a structure should obey the following criteria

1. The representation should be one-to-one: Each platonic structure should correspond to one representation, and each representation should correspond to one structure
2. The representation should be invariant under transformations which do not change the structure, such as translations or rotations. For periodic systems, the representation should be invariant with respect to different choices of unit cell.
3. The representation should be continuous: Similar structures should have similar representations.
4. The representation should be simple to calculate

In the following, we use the FCHL representation[65], which represents structures in terms of the distances, angles and dihedral angles between the constituent atoms, and which uses a Gaussian placed on the periodic table to represent the chemical species. As an input, this fingerprint requires the atomic coordinates of the structure.

One of the issues with using a fingerprint based on the relaxed coordinates of a structure as input to a machine learning model is that relaxed structures are often difficult to find, or at least harder to find than some of the properties we might want to do machine learning for. For example, performing a local relaxation of a given structure may take tens of self-consistent calculations. Once that's accomplished, though, calculating the heat of formation takes just one self-consistent calculation, as does calculating the DFT band gap. Calculating a band-structure, which is already a more complex object, takes a similarly short time. The upshot of this is that to

create a machine learning model which takes as input a relaxed set of coordinates and produces as output a heat of formation, is nonsensical, as it violates rule 4 above.

Rather than using the relaxed structures as input to our model, we can instead use the fact that we have performed combinatorial lattice decoration based on known structures. For each structure in the database, we have access to the atomic coordinates of the seed structure. By replacing the atomic species of the seed structure with those of the target structure, we obtain a sensible initial guess of the coordinates of the target structure. This can be improved further by scaling the lattice parameter of the structure according to the ratio between the mean covalent radius of the target and seed structures. Using this approach, we can generate a representation for each structure in the database without knowing the relaxed coordinates.

In this case, the inputs are the representations of the structures given above, and the target outputs are the heats of formation. As a model, we use kernel ridge regression using a Gaussian kernel.

In this case the model y of a given input x is given by $y(x) = \sum_i \alpha_i K(x, x'; \sigma)$, where the kernel K is given by $K(x_i, x_j; \sigma) = e^{\frac{\|x_i - x_j\|^2}{2\sigma^2}}$ and the sum runs over the i training points in the data. The regression coefficients α_i can be found as $\boldsymbol{\alpha} = (\mathbf{K} + \lambda \mathbf{I})^{-1} \mathbf{y}$, where λ is a regularization parameter which prevents over-fitting and ensures that the matrix inversion is possible, and $\mathbf{y}$ is the vector of known outputs corresponding to the training points $\mathbf{x}$. Doing this for all the materials in the database, and optimizing the values of σ and λ gives the model performance and training curves shown in Fig. 4.14, where we have used a six-fold cross validation scheme.

We see that when training on 2500 materials, the model achieves a mean absolute error of 0.12 eV/atom, which is comparable to the accuracy of the DFT calculation itself. If we had used the prediction to evaluate the thermodynamic stability of the structures in each prototype, we would have found the following: 84% of the materials would have been correctly predicted to be potentially stable (medium or high stability) and 11% would have been correctly predicted to be unstable. A further 2% would have been predicted to be stable while actually being unstable, while 3% would be stable, despite being predicted as unstable. Using this approach to pre-screen the prototypes would thus allow us to reject the majority of the unstable materials *without* having to obtain the relaxed structure.

Ideally, we would like to be able to test the heat of formation of a completely new prototype before performing any relaxations. In this case, the preceding analysis is slightly too optimistic, since for every material in the test set there was a representative from the training set. Instead, we can train the model on $N - 1$ prototypes, and test it on the remaining prototype. Doing this gives a mean absolute error of 0.28 eV/atom, which is a significantly worse result. However, it is still sufficiently accurate we can determine which prototypes are generally more stable than others, and thus prioritize investigating those first.

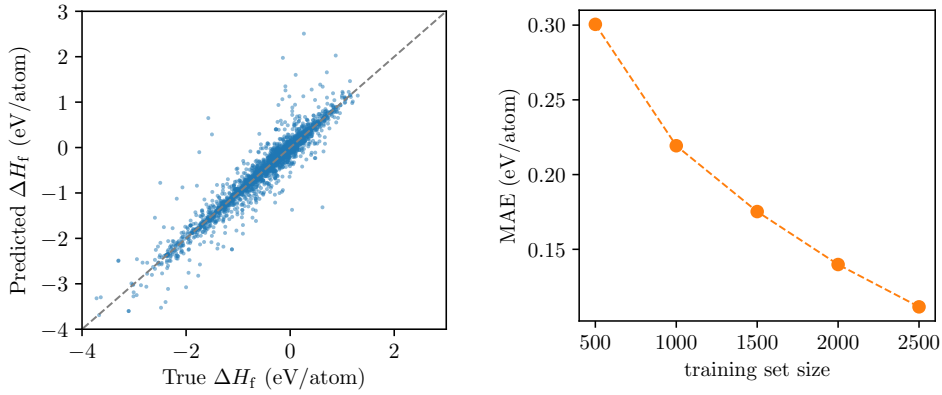

Figure 4.14: Predicting the heat of formation of the compounds in the C2DB using machine learning. (left) the predicted heat of formation vs the true heat of formation for each of the 3000 compounds in the C2DB, when the machine is trained on 2500 structures. (right) The learning curve of the model, showing the mean absolute error of the predicted heats of formation, as a function of the size of the training set.

This is only the first step in exploring the wealth of data available, but it already shows the promise of the approach. More work is needed to develop other descriptors, which can quickly predict properties of interest for 2D materials.

4.3.3 New materials for different applications

A widely used approach to materials discovery is a screening or funnel approach, which can be extremely useful when one has a specific application in mind and is searching for materials which would perform well. By defining a sequence of descriptors which characterize how well a material performs the desired tasks, and an accompanying set of exclusion criteria, one can take a starting set of candidate materials and successively filter out unsuitable materials. To reduce the computational cost, the calculations should be carried out so that the simplest descriptors are calculated first, and unsuitable materials are excluded as soon as possible.

For the C2DB, the only exclusion criteria we have applied are stability criteria. Otherwise, all properties have been calculated for all materials[2]. This means that we are not limited to a single application, but can search through the database, for any combination of properties, including for applications we did not have in mind when designing the workflow. Looking through the database, we find a number of differ-

[2]Apart from G_0W_0 band structures and the BSE spectrum

ent materials with interesting transport properties or magnetic properties. These will briefly be described in the following sections, which are a condensed version of section 3.2 of Paper I.

4.3.3.1 Transport

A key property for transport applications is the carrier mobility, which relates the drift velocity of the carriers to the strength of an applied field. In many cases, we wish to see as high a mobility as possible. Calculating the mobility from first principles is possible, but time-consuming. On the other hand, if one assumes energetically isolated and parabolic bands, the intrinsic mobility limited only by scattering on acoustic phonons can be estimated from the Takagi formula [66],

$$\mu_i = \frac{e\hbar^3 \rho v_i^2}{k_\mathrm{B} T m_i^* m_\mathrm{d}^* D_i^2}. \tag{4.4}$$

Here μ is the mobility, i refers to the transport direction, ρ is the mass density, v_i is the speed of sound in the material, m_i^* is the carrier mass, m_d^* is the equivalent isotropic density-of-state mass defined as $m_\mathrm{d}^* = \sqrt{m_x^* m_y^*}$, and D_i is the deformation potential, which expresses how the band edges of the system move under strain, and is a good descriptor for the strength of the electron-phonon coupling.

Comparing the terms appearing in Eq. (4.4) with the properties we calculate in Fig. 4.1, we see that all of the necessary quantities are already calculated. This means that we have enough information to estimate the mobility of all the semiconductors in the C2DB.

Restricting our attention to the materials with high stability in both directions, we find several materials with high electron or hole mobilities, which could be of interest for further study. As a validation of our approach, we observe the known high-mobility semiconductors appear in our list. Table 4.2 shows some key transport properties of stable, novel 2D materials with high carrier mobilities.

4.3.3.2 Magnetism

Magnetism in low-dimensional materials is currently a very active field of research, since the discovery of magnetism in monolayer CrI_3[67]. From the Mermin-Wagner theorem[68], we know that for isotropic systems in low dimensions is not possible at finite temperatures. A finite magnetic anisotropy with an out of plane easy axis breaks the assumption behind the Mermin-Wagner theorem and makes magnetic order possible at finite temperature. The critical temperature for magnetic order in 2D materials will thus have a strong dependence on the anisotropy.

On table 4.3 we list some stable magnetic materials with magnetic anisotropies comparable or greater than those of CrI_3; these are likely to have critical temperatures similar to, or potentially even higher than, CrI_3.

Carrier	Formula	Prototype	Gap (eV)	μ_{high} ($\text{cm}^2/(\text{V}\cdot\text{s})$)	m^* (m_0)	$\frac{\mu_{\text{high}}}{\mu_{\text{low}}}$
Holes	PbS_2	MoS_2	1.39	30000	0.62	1.4
	OsO_2	WTe_2	0.17	23000	0.23	3.0
	$ZrCl_2$	MoS_2	0.98	12000	0.43	1.1
	WSSe	MoSSe	1.40	5500	0.37	1.0
Electrons	$PtTe_2$	CdI_2	0.30	9600	0.17	1.3
	GaO	GaS	1.56	7200	0.32	1.0
	NiS_2	CdI_2	0.58	6000	0.29	1.5
	$RuTe_2$	WTe_2	0.64	4600	1.55	8.5

Table 4.2: Stable materials with high intrinsic mobility according to Equation (4.4), and some selected transport properties. μ_{high} is the larger value of the mobilities in the x or y directions, m^* is the corresponding effective mass, and $\mu_{\text{high}}/\mu_{\text{low}}$ quantifies the anisotropy in the mobility..

Formula	Prototype	MM (μ_{B})	Gap (eV)	MA (meV/atom)	Magnetic state	ΔH_{hull} (eV/atom)
OsI_3	BiI_3	0.9	0.0	−3.17	FM	0.18
CrTe	FeSe	2.6	0.0	−1.85	AFM	0.15
$FeCl_3$	BiI_3	1.0	0.01	−1.84	FM	−0.08
FeTe	FeSe	1.9	0.0	−1.06	FM	0.08
$MnTe_2$	CdI_2	2.7	0.0	−0.94	FM	−0.10
$FeBr_3$	BiI_3	1.0	0.04	−0.88	FM	−0.04
CrI_3	**BiI_3**	**3.0**	**0.90**	**−0.85**	**FM**	**−0.21**
MnTe	FeSe	3.8	0.69	−0.75	AFM	−0.15
NiO	PbSe	1.1	0.0	−0.53	FM	0.05
FeBrO	FeOCl	1.1	0.0	−0.47	FM	−0.05
CrISe	FeOCl	3.0	0.0	−0.45	FM	−0.10
$MnSe_2$	CdI_2	2.8	0.0	−0.40	FM	−0.18
CrIS	FeOCl	3.0	0.35	−0.36	FM	−0.10
MnO_2	CdI_2	3.0	1.13	−0.36	FM	0.02
VCl_3	BiI_3	2.0	0.0	−0.35	FM	−0.01
MnSe	FeSe	3.7	0.90	−0.31	AFM	−0.20
CrSe	FeSe	2.0	0.0	−0.31	AFM	0.12

Table 4.3: A selection of magnetic materials with a negative MA per magnetic atom.

CHAPTER 5

Dissociation of Excitons in 2D materials

In this chapter, the focus shifts from calculating general properties for many different materials, to calculating single properties for only one or two materials, namely the dissociation rate of excitons in the transition metal dichalcogenides MoS_2 and WSe_2.

One of they key features of two-dimensional materials is a very strong interaction with light. As an illustration, monolayers of the three transition metal dichalcogenides WS_2, MoS_2 and $MoSe_2$ have been observed to absorb more than 5% of incident sunlight[34]. Additionally, it has been observed that there is a strong optical response below the quasiparticle band gap[69, 70]. This fact seems counter-intuitive, as the band gap is an energy region with no electronic states, and it should therefore not be possible to have transitions with energies below the gap. The answer to the paradox lies in the breakdown of the single particle picture of the quasiparticles: When an electron is excited from the valence band to the conduction band, it leaves behind a positively charged hole. When the electron and the hole are close to one another, the Coulomb interaction between them causes them to gain energy compared with when they are separated. This excitonic state, with an electron bound to a hole, has lower energy than a free electron and hole, and thus lives inside the quasiparticle gap

The key feature of excitons is that they are bound; for many purposes however, we are interested in generating free carriers, rather than excitons. An example could be photovoltaic applications or photodetectors, which both depend on the separation of electrons and holes. Typically, this is much harder to accomplish with excitons in 2D (where binding energies are on the order of 0.1-1.0 eV) than it is in 3D systems (where the binding energies are much smaller)[71]. This means that thermal effects are typically not strong enough to dissociate 2D excitons, and an additional mechanism is needed.

One way this can be accomplished is by the application of an electric field[72], which causes the electron and hole to move in opposite directions, thereby dissociating the exciton. The exciton thus changes from a bound state to a *resonance* with a finite lifetime, and shifts down in energy – the so-called Stark shift[73].

In the following, I will describe how we can model excitons using many-body perturbation theory, and how this leads to a hydrogen-like model for the exciton wave

function.

Following that, in section 5.2, I will develop the theory of how to define resonances, and describe how it is necessary to use open boundary conditions to describe them mathematically. I will then provide a brief overview of the complex scaling technique, which allows us to precisely calculate the lifetimes and energy shifts.

Finally, I will summarize the contents of two publications in this area – Paper IIand Paper III– which demonstrate that it is realistic to use electric fields to dissociate excitons in two-dimensional materials, and furthermore illustrate the applicability of the complex scaling technique.

5.1 Modeling Excitons

In the single-particle picture, the optical absorption is given by (3.16) and (3.15) for 3D and 2D materials respectively. In both cases, we see that the absorption onset corresponds to the onset of single-particle transitions, as this is where the denominator in the expression diverges.

To model the excitonic behavior, we therefore need to include many-body effects. This is accomplished by writing the excitation we seek for as a linear combination of single particle excitations, $\Psi_{\mathrm{ex}}(\mathbf{q}_{\mathrm{ex}}) = \sum_{vc\mathbf{k}} F(\mathbf{k})\Phi_{c\mathbf{k}+\mathbf{q}_{\mathrm{ex}},v_{\mathbf{k}}}$, where $\Phi_{c\mathbf{k}+\mathbf{q}_{\mathrm{ex}},v_{\mathbf{k}}} \equiv \Phi_S$ is the state created from the electronic ground state by taking an electron from an occupied state v with momentum $\mathbf{k}$ and placing it into an unoccupied state c with momentum $\mathbf{k} + \mathbf{q}_{\mathrm{ex}}$. Frequently it is sufficient to consider only a few occupied and unoccupied bands, and to consider only positive energy transitions[74]. Inserting the trial state into the many-body Hamiltonian (equation (2.3)) reveals that the expansion coefficients F obey the equation

$$\sum_{S'} \mathcal{H}_{SS'}(\mathbf{q}_{ex}) F^{\lambda}_{S'}(\mathbf{q}_{\mathrm{ex}}) = E^{\lambda}(\mathbf{q}_{\mathrm{ex}}) F^{\lambda}_{S}(\mathbf{q}_{\mathrm{ex}}), \tag{5.1}$$

with the two-particle Hamiltonian given by

$$\mathcal{H}_{SS'}(\mathbf{q}) = (\varepsilon_{c,\mathbf{k}+\mathbf{q}} - \varepsilon_{v,\mathbf{k}})\delta_{SS'} - (f_{c,\mathbf{k}+\mathbf{q}} - f_{v,\mathbf{k}})K_{SS'}(\mathbf{q}) \tag{5.2}$$

The kernel, K is given by the sum of two separate terms, namely the unscreened exchange interaction, and the screened direct electron-hole interaction, so that $K_{\mathrm{SS}'}(\mathbf{q}) = 2V_{\mathrm{SS}'} - W_{\mathrm{SS}'}$. The factor of two on the first term accounts for spin. Fourier transforming the expansion coefficients F appearing in Eq. (5.1), we can show[75] that they obey a hydrogen-like equation of the form

$$\left[-\frac{\nabla^2}{2\mu_{\mathrm{ex}}} + W(\mathbf{r})\right] \psi_{\mathrm{ex}}(\mathbf{r}) = \varepsilon_n \psi_{\mathrm{ex}}(\mathbf{r}) \tag{5.3}$$

An equation of this type holds in both two and in three dimensions, where in the two-dimensional case, the kinetic energy operator and the positions vectors are also two-dimensional. The difference between the two-dimensional case and the three-dimensional case lies in the behavior of the screened Coulomb interaction. In 3D, semiconductors typically have strong screening, and the potential in Eq. (5.3) is thus expected to be shallow, giving small binding energies. In 2D materials, the screening of the Coulomb interaction is much weaker, and thus the exciton binding energies are much larger.

As we have seen in section 3.2, the functional form of the screened Coulomb interaction is also different in 2D compared with 3D, which notably causes the higher-lying excitonic states to deviate from the expected Rydberg series behavior[76]. If the layers we are considering have negligible thickness, the 2D screening is given by $\epsilon_{2D} = 1 + 2\pi\alpha q$, leading to the expression for $W(\mathbf{r})$ given in Eq. (3.14) to model the behavior of excitons. For thicker layers, a more sophisticated approach is needed, but the approximation remains valid for small q [41].

Examining (3.14), we see that the relevant parameters we should calculate via *ab initio* calculations are the reduced exciton mass, and the slope of the dielectric screening at $q = 0$. In Tab. 5.1 I show the parameters for a single layer of MoS_2, as well as the exciton binding energy these Mott-Wannier model, as well as the result obtained from solving the BSE.

Material	μ_{ex} (m_0)	α (a_0)	$E_{b,\text{Mott-Wannier}}$ (eV)	$E_{b,BSE}$ (eV)
MoS_2	0.27	11.1	0.62	0.43[41]

Table 5.1: The Mott-Wannier parameters for monolayer MoS_2, and the corresponding exciton binding energy.

5.2 From Bound States to Resonances

To calculate the lifetime of an exciton in an electric field, we should look first at what changes when an electric field is applied. Figure 5.1 sketches the situation. The left panel shows the situation when no electric field is applied:The screened Coulomb interaction from the hole creates a potential well, localizing the electron in a bound state nearby, with a discrete, real energy. A continuum of unbound states lies above all the bound states, these represent free electrons and holes. The energy difference between the bound state and the lowest lying continuum states is the binding energy of the exciton. Applying a constant electric field corresponds to adding a linear term to the potential, as shown in the right panel of the figure. The bound states previously identified are no longer eigenstates of the Hamiltonian, since the exciton now couples to all of the continuum states, and can leak out of the potential well. For the situation sketched in the figure, the exciton can dissociate even for arbitrarily

small field strengths – as long as the electric field extends out far enough, it will always be energetically favorable for the electron to move "downhill" in the field.

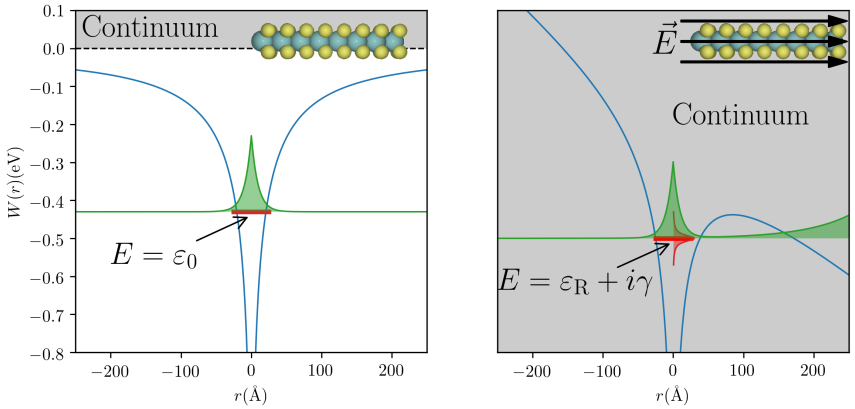

Figure 5.1: A sketch of the potentials and states involved in exciton dissociation. On the left we see the screened Coulomb potential of the hole, which gives rise to bound states confined to the well. On the right, we have the same screened Coulomb potential with an additional constant electric field. The previously bound state now couple to the continuum states, and leak out of the well. Its energy shifts down due to the Stark effect, and broadens, due to lifetime effects..

From an intuitive perspective, this decay of the exciton state can be modeled by giving the exciton a complex energy $E = E_R + i\Gamma$, with Γ representing its inverse lifetime. When this state evolves in time, it will undergo exponential decay, precisely as desired. However, this approach is unsatisfactory for two reasons. Firstly, in quantum mechanics we usually consider Hermitian Hamiltonians, which must of necessity have real eigenstates. In this setting, an eigenstate of the Hamiltonian with a complex eigenvalue is nonsensical. Secondly, by focusing on the resonance and its lifetime as a property of the Hamiltonian, we encounter *Howland's razor*, which states that

> No satisfactory definition of a resonance can depend only on the structure of a single operator on an abstract Hilbert space.[77]

An illustration of this principle is given by the family of Stark Hamiltonians, $\hat{H}_\kappa(\mathbf{r}) = -\frac{\nabla^2}{2} - \frac{1}{r} + \kappa x$. Then, for every nonzero κ and κ', there is a unitary transformation connecting the two Hamiltonians $\hat{H}_\kappa$ and $\hat{H}_{\kappa'}$. This transformation preserves eigenvalues, and we arrive at the puzzling conclusion that the decay rate of our state is independent of the electric field applied.

In order to describe these resonant states, a different approach is therefore needed. A key point to note is that the resonant states, such as decaying excitons, correspond to particles leaking out of our system. This means that the wave functions which correspond to these states are of a class we do not typically consider: Instead of having square-integrable wave functions ψ, with $|\psi(\mathbf{r})| \to 0$ as $r \to \infty$, we should look instead for states which resemble plane waves at infinity: $\psi(\mathbf{r}) \to ae^{i\kappa\cdot\mathbf{r}}$, with the (potentially complex) momentum κ obeying $\Re(\kappa \cdot \mathbf{r}) > 0$. These boundary conditions correspond to having only outgoing plane waves far away from the scattering region, and were first investigated by Siegert[78].

Mathematically, what we are doing by allowing these non square-integrable wave functions is to greatly extend the domain of the Hamiltonian. In this domain, there are stationary states with complex eigenvalues, and these are precisely the resonances we seek.

In principle, it should be possible to directly diagonalize the Hamiltonian we are interested in subject to these scattering boundary conditions. In practice, this is usually a difficult undertaking. Usually, we prefer to work with square-integrable functions and zero boundary conditions. These have the advantage that the boundary conditions are easy to impose, and the convergence of a simulation with respect to system size can easily be checked. The resonant states are not only divergent, they also have energy-dependent boundary conditions: for a plane wave state, the energy is related to the momentum through $E = \frac{k^2}{2m}$. Instead of directly diagonalizing the Hamiltonian, a much better approach is to use *complex scaling*.

5.3 Complex Scaling

The idea behind complex scaling is to somehow transform the problem sketched in the previous section in such a way that we can deal with square-integrable functions instead of divergent ones, and with zero boundary conditions instead of energy-dependent ones. The following brief explanation is based on [79], and the reader is invited to look there and in [80, 81] for a more rigorous treatment.

As hinted at by the name, the complex scaling technique involves transforming real positions and momenta into the complex plane. More specifically, we rotate the coordinates into the complex plane according to the following recipe

$$\begin{aligned} \mathbf{p} \equiv i\nabla \to e^{-i\theta}\mathbf{p} \equiv ie^{-i\theta}\nabla \\ \mathbf{r} \to e^{i\theta}\mathbf{r}, \end{aligned}$$

for some real angle θ. A single-particle Hamiltonian with a local potential then transforms as

$$\hat{H} \equiv -\frac{\nabla^2}{2m} + V(\mathbf{r}) \to -e^{-i2\theta}\frac{\nabla^2}{2m} + V\left(e^{i\theta}\mathbf{r}\right) \equiv \hat{H}_\theta, \tag{5.4}$$

and the transformed time-independent Schrödinger equation then reads $\hat{H}_\theta \psi_\theta(\mathbf{r}) = \varepsilon_\theta \psi_\theta(\mathbf{r})$.

In order for the transformation to leave the bound states and their energies unchanged, we must require that all wave functions transform as $\psi_\theta(\mathbf{r}) = e^{iN\theta/2}\psi\left(e^{i\theta}\right)\mathbf{t})$.

To see this, we can look at the inner product $\varepsilon_0 = \left\langle \psi \middle| \hat{H} \middle| \psi \right\rangle$. This is given by the integral $\varepsilon_0 = \int \mathrm{d}^N\mathbf{r}\, \psi^*(\mathbf{r}) H \psi(\mathbf{r})$. If the state ψ under consideration decays quickly enough, and both $\hat{H}$ and ψ are analytic, we can use contour integration to rotate the axis of integration into the complex plane without affecting the value of the integral. Letting $\rho_\alpha = e^{i\theta}\mathbf{r}_\alpha$ for each of the N Cartesian directions α, we have

$$
\begin{aligned}
\varepsilon_0 &= \int \mathrm{d}^N\mathbf{r}\, [\psi^*(\mathbf{r}) H(\mathbf{r}) \psi(\mathbf{r})] \\
&= \int \mathrm{d}^N\rho\, [\psi^*(\rho) H(\rho) \psi(\rho)] \\
&= \int \mathrm{d}^N\mathbf{r} e^{i\theta}\, \left[\psi^*(\mathbf{r}e^{i\theta}) H(\mathbf{r}e^{i\theta}) \psi(\mathbf{r}e^{i\theta})\right] \\
&= \int \mathrm{d}^N\mathbf{r}\, \left[e^{iN\theta/2}\psi^*(\mathbf{r}e^{i\theta}) H(\mathbf{r}e^{i\theta}) e^{iN\theta/2}\psi(\mathbf{r}e^{i\theta})\right] \\
&= \int \mathrm{d}^N\mathbf{r}\, [\psi_\theta^*(\mathbf{r}) H_\theta(\mathbf{r}) \psi_\theta(\mathbf{r})] = \varepsilon_\theta
\end{aligned}
$$

From this sketch, we can already see that for the complex scaling technique to work, there are certain requirements for the potential under consideration. That the potential is analytic is not a sufficient condition; it must also be *dilatation analytic*. This is a slightly technical requirement, which is described in more detail in [81]. For our purposes, it suffices to note that the class of allowed potentials is large enough to include the Coulomb potential and all Yukawa potentials, as well as the potential described by Eq. (3.14). Unfortunately, a constant electric field is not dilatation analytic, but for this particular case, it has been shown that the complex scaling technique works nevertheless[82].

The crucial result from complex scaling is that the eigenstates and eigenvalues of H_θ behave differently depending on whether they are bound states, resonances or part of the continuum. We have already seen that the bound states remain bound under the transformation, with the same eigenvalues. As to the continuum states, we can understand their behavior under the complex scaling by examining them far away from the scattering center, where the potential is negligible. In this region, we thus have $\hat{H} \sim -\frac{\nabla^2}{2m}$, and the wave functions resemble plane waves, $\psi_\mathrm{c}(\mathbf{r}) \sim e^{i\mathbf{k}\cdot\mathbf{r}}$, with energy eigenvalue $\frac{k^2}{2m}$. Any eigenstate of $\hat{H}$ is also an eigenstate of $\hat{H}_\theta$, but with eigenvalue $\varepsilon_\theta = -i2\theta\varepsilon_0$. The continuum states thus rotate into the complex plane, with a rotation angle equal to twice the scaling angle.

Finally, the last and most interesting case is that of the resonances. Let us consider a state satisfying the Siegert resonant boundary conditions and apply the complex scaling transformation to it, and let $\kappa \equiv \mathbf{p} - i\mathbf{q}$ be the complex momentum of this state. Then as $r \to \infty$ we have

$$\begin{aligned}\psi_\theta(\mathbf{r}) &= e^{iN\theta/2}\psi(r\exp i\theta),\\ &= e^{iN\theta/2}e^{i(\mathbf{p}-i\mathbf{q})\cdot e^{i\theta}\mathbf{r}}\\ &= e^{iN\theta/2}e^{i(\mathbf{p}\cos\theta+\mathbf{q}\sin\theta)\cdot\mathbf{r}}\,e^{(-\mathbf{p}\sin\theta+\mathbf{q}\cos\theta)\cdot\mathbf{r}}.\end{aligned}$$

We see that the final term leads to an exponential decay of the wave function with increasing r, as long as $\theta > \tan^{-1}(\mathbf{q}\cdot\hat{r}/\mathbf{p}\cdot r)$. For values of θ greater than this, the resonant state is therefore square integrable, and by an argument similar to that used for the bound states, it can be shown that the eigenvalue which then appears is independent of the value of θ.

Figure 5.2 shows the calculated eigenvalues of the Mott-Wannier exciton for MoS_2 with no applied electric field, for different values of the scaling parameter θ. The ground state of the exciton, as well as the higher-lying excitonic states can clearly be seen, as can the continuum, which rotates exactly as predicted. Due to the finite size of the simulation box, the continuum states do not start at zero energy, but slightly below it. For this system, there are no resonances since the electric field has been set to zero.

Armed with newfound understanding of what resonances are and how we can use complex scaling to describe them, we turn now to two separate applications of the complex scaling technique, in papers IIand III. In the first, the technique is applied to excitons in monolayer MoS_2, while in the second we wish to describe excitons in WSe_2

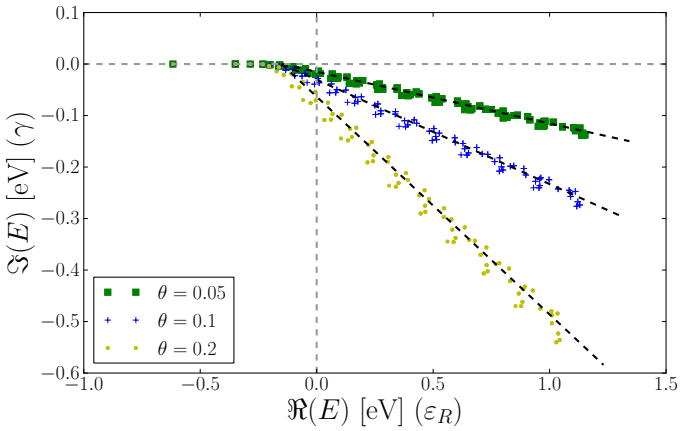

Figure 5.2: The numerically evaluated eigenvalues of the complex-scaled Mott-Wannier model of an exciton in MoS_2 for different values of the scaling parameter θ. The different behavior of the bound states and the resonances is clear; the slope of the dashed lines is not fitted, but rather forced to be 2θ. Due to the finite size of the simulation box, the continuum does not start at zero, but slightly below it.

5.4 Paper I: Stark shift and electric-field-induced dissociation of excitons in monolayer MoS_2 and hBN/MoS_2 heterostructures

In Paper I the complex scaling technique is used to describe exciton dissociation in a monolayer of MoS_2 in different dielectric environments. The exciton was modeled using the Mott-Wannier model, Eq. (5.3), and the screened potential was described using the linear 2D Coulomb interaction of (3.13), $\epsilon(\mathbf{q}) = 1 + 2\pi\alpha q$. Using this linear interaction has the advantage that there is a known analytic form of the potential in real space (Eq. (3.14)) which lends itself to easy evaluation on complex arguments.

Using the complex scaling technique, we obtain information about how both the real and imaginary part of the complex eigenvalue changes as a function of the electric field strength. The imaginary part reveals how the lifetime of the exciton is affected by the field, while the change in the real part quantifies the Stark shift of the resonance energy. This effect is directly observable in absorption measurements, which could be used verify the model.

From second order perturbation theory, we would expect the Stark shift to be quadratic in the field strength, for small fields. This is because the excitonic ground state is symmetric about $\mathbf{r} = 0$; the applied field induces a small dipole moment to this charge

distribution, and it is the interaction of this dipole with the field which gives the Stark shift.

Using a simple hydrogenic model for the exciton[53], the Stark shift is evaluated to be

$$\Delta E = -\frac{21}{64}\frac{\epsilon_{\text{eff}}^4}{\mu^3}E^2$$

where μ is the exciton mass, and $\epsilon_{\text{eff}} = \frac{1}{2} + \frac{1}{2}\sqrt{1 + 32\pi\alpha\mu/3}$, with α defined as in Eq. (3.13). A comparison of the result from perturbation theory with the result from complex scaling shows excellent agreement.

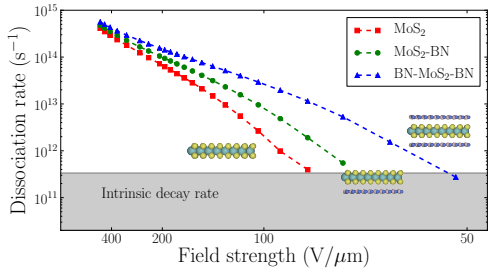

Figure 5.3: The exciton dissociation rates as a function of field strengths for three different dielectric environments of MoS_2.

With regards to the rates, we calculate the dissociation rates for freestanding MoS_2, MoS_2 on a single layer of graphene, and MoS_2 encapsulated between two layers of graphene. These rates are shown on Fig. 5.3 The graphene changes the dielectric environment of the exciton, and increases the dissociation rates by orders of magnitude. We also see that for all three systems, and for a realistic range of field strengths, the dissociation rate is greater than the intrinsic exciton decay rate. It should therefore be possible to use this approach to generate free electrons and holes from excitons.

5.5 Paper III: Dissociation of two-dimensional excitons in monolayer WSe_2

In this experimental paper, time and spectrally resolved photocurrent measurements in a monolayer WSe_2 pn junction were used to measure the dissociation rates of excitons under the application of an in-plane static electric field, and the results were found to be consistent with the field-induced ionization of 2D Mott-Wannier excitons.

My contribution to the paper was in helping calculate the parameters used to model the excitons and using the complex scaling technique to calculate the dissociation rates.

CHAPTER 6

Papers

6.1 Paper I

The Computational 2D Materials Database: high-throughput modeling and discovery of atomically thin crystals

TOPICAL REVIEW • OPEN ACCESS

The Computational 2D Materials Database: high-throughput modeling and discovery of atomically thin crystals

To cite this article: Sten Haastrup *et al* 2018 *2D Mater.* **5** 042002

2D Materials

OPEN ACCESS

RECEIVED
28 March 2018

REVISED
8 June 2018

ACCEPTED FOR PUBLICATION
28 June 2018

PUBLISHED
7 September 2018

TOPICAL REVIEW

The Computational 2D Materials Database: high-throughput modeling and discovery of atomically thin crystals

Sten Haastrup[1], Mikkel Strange[1], Mohnish Pandey[1], Thorsten Deilmann[1], Per S Schmidt[1], Nicki F Hinsche[1], Morten N Gjerding[1,2], Daniele Torelli[1], Peter M Larsen[1], Anders C Riis-Jensen[1], Jakob Gath[1], Karsten W Jacobsen[1], Jens Jørgen Mortensen[1], Thomas Olsen[1] and Kristian S Thygesen[1,2]

[1] CAMD, Department of Physics, Technical University of Denmark, 2800 Kgs. Lyngby, Denmark
[2] Center for Nanostructured Graphene (CNG), Technical University of Denmark, 2800 Kgs. Lyngby, Denmark

E-mail: thygesen@fysik.dtu.dk

Keywords: ab initio calculations, opto-electronic properties, database, materials discovery, materials design, 2D materials, many-body perturbation theory

Abstract

We introduce the Computational 2D Materials Database (C2DB), which organises a variety of structural, thermodynamic, elastic, electronic, magnetic, and optical properties of around 1500 two-dimensional materials distributed over more than 30 different crystal structures. Material properties are systematically calculated by state-of-the-art density functional theory and many-body perturbation theory (G_0W_0 and the Bethe–Salpeter equation for ∼250 materials) following a semi-automated workflow for maximal consistency and transparency. The C2DB is fully open and can be browsed online (http://c2db.fysik.dtu.dk) or downloaded in its entirety. In this paper, we describe the workflow behind the database, present an overview of the properties and materials currently available, and explore trends and correlations in the data. Moreover, we identify a large number of new potentially synthesisable 2D materials with interesting properties targeting applications within spintronics, (opto-)electronics, and plasmonics. The C2DB offers a comprehensive and easily accessible overview of the rapidly expanding family of 2D materials and forms an ideal platform for computational modeling and design of new 2D materials and van der Waals heterostructures.

1. Introduction

Over the past decade, atomically thin two-dimensional (2D) materials have made their way to the forefront of several research areas including batteries, (electro-) catalysis, electronics, and photonics [1, 2]. This development was prompted by the intriguing and easily tunable properties of atomically thin crystals and has been fueled by the constant discovery of new 2D materials and the emergent concepts of lateral [3] and vertical [4] 2D heterostructures, which opens completely new possibilities for designing materials with tailored and superior properties.

So far more than fifty compounds have been synthesised or exfoliated as single layers (see figure 7). These include the well known monoelemental crystals (Xenes, e.g. graphene, phosphorene) [5] and their ligand functionalised derivatives (Xanes, e.g. CF, GeH) [6], transition metal dichalcogenides (TMDCs, e.g. MoS_2, $TaSe_2$) [7], transition metal carbides and -nitrides (MXenes, e.g. Ti_2CO_2) [8], group III–V semiconductors and insulators (e.g. GaN, BN) [9, 10], transition metal halides (e.g. CrI_3) [11, 12], post-transition metal chalcogenides (e.g. GaS and GaSe) [13, 14] and organic-inorganic hybrid perovskites (e.g. $Pb(C_4H_9NH_3)_2I_4$) [15]. However, the already known monolayers are only the tip of a much larger iceberg. Indeed, recent data mining studies indicate that several hundred 2D materials could be exfoliated from known layered bulk crystals [16–19]. In the present work we take a complementary approach to 2D materials discovery based on combinatorial lattice decoration and identify another few hundred previously unknown and potentially synthesisable monolayers.

In the search for new materials with tailored properties or novel functionalities, first-principles calculations are playing an increasingly important role. The continuous increase in computing power and significant advancements of theoretical methods and numerical algorithms have pushed the field to a point where first-principles calculations are comparable to experiments in terms of accuracy and greatly

surpass them in terms of speed and cost. For more than a century, experimental databases on e.g. structural, thermal, and electronic properties, have been a cornerstone of materials science, and in the past decade, the experimental data have been augmented by an explosion of computational data obtained from first-principles calculations. Strong efforts are currently being focused on storing and organising the computational data in open repositories [20, 21]. Some of the larger repositories, together containing millions of material entries, are the Materials Project [22], the Automatic Flow for Materials Discovery (AFLOWLIB) [23], the Open Quantum Materials Database (OQMD) [24, 25], and the Novel Materials Discovery (NOMAD) Repository [26].

The advantages of computational materials databases are many. Most obviously, they facilitate open sharing and comparison of research data whilst reducing duplication of efforts. In addition, they underpin the development and benchmarking of new methods by providing easy access to common reference systems [27]. Finally, the databases enable the application of machine learning techniques to identify deep and complex correlations in the materials space and to use them for designing materials with tailored properties and for accelerating the discovery of new materials [28–30]. Among the challenges facing the computational databases is the quality of the stored data, which depends both on the numerical precision (e.g. the employed k-point grid and basis set size) and the accuracy of the employed physical models (e.g. the exchange-correlation functional). Most of the existing computational databases store results of standard density functional theory (DFT) calculations. While such methods, when properly conducted, are quite reliable for ground state properties such as structural and thermodynamic properties, they are generally not quantitatively accurate for excited state properties such as electronic band structures and optical absorption spectra.

Compared to databases of bulk materials, databases of 2D materials are still few and less developed. Early work used DFT to explore the stability and electronic structures of monolayers of group III–V honeycomb lattices [31, 32] and the class of MX_2 transition metal dichalcogenides and oxides [33]. Later, by data-filtering the inorganic crystal structure database (ICSD), 92 experimentally known layered crystals were identified and their electronic band structures calculated at the DFT level [34]. Another DFT study, also focused on stability and band structures, explored around one hundred 2D materials selected from different structure classes [35]. To overcome the known limitations of DFT, a database with many-body G_0W_0 band structures for 50 semiconducting TMDCs was established [36]. Very recently, data mining of the Materials Project and experimental crystal structure databases in the spirit of [34], led to the identification of close to one thousand experimentally known layered crystals from which single layers could potentially be exfoliated [16–19]. These works also computed basic energetic, structural and electronic properties of the monolayers (or at least selected subsets) at the DFT level.

In this paper, we introduce the open Computational 2D Materials Database (C2DB) which organises a variety of *ab initio* calculated properties for more than 1500 different 2D materials. The key characteristics of the C2DB are:

- **Materials**: the database focuses entirely on 2D materials, i.e. isolated monolayers, obtained by combinatorial lattice decoration of known crystal structure prototypes.
- **Consistency**: all properties of all materials are calculated using the same code and parameter settings following the same workflow for maximum transparency, reproducibility, and consistency of the data.
- **Properties**: the database contains a large and diverse set of properties covering structural, thermodynamic, magnetic, elastic, electronic, dielectric and optical properties.
- **Accuracy**: Hybrid functionals (HSE06) as well as beyond-DFT many-body perturbation theory (G_0W_0) are employed to obtain quantitatively accurate band structures, and optical properties are obtained from the random phase approximation (RPA) and Bethe–Salpeter equation (BSE).
- **Openness**: the database is freely accessible and can be directly downloaded and browsed online using simple and advanced queries.

The systematic combinatorial approach used to generate the structures in the database inevitably produces many materials that are unstable and thus unrealistic and impossible to synthesise in reality. Such 'hypothetical' structures may, however, still be useful in a number of contexts, e.g. for method development and benchmarking, testing and training of machine learning algorithms, identification of trends and structure-property relationships, etc. For this reason we map out the properties of all but the most unstable (and thus chemically unreasonable) compounds. Nevertheless, the reliable assessment of stability and synthesisability of the candidate structures is an essential issue. Using the 55 materials in the C2DB, which have been experimentally synthesised in monolayer form, as a guideline, we set down the criteria that a hypothesised 2D material should fulfill in order for it to be 'likely synthesisable'. On the basis of these criteria, we introduce a simple *stability scale* to quantify a candidate material's dynamic and thermodynamic stability. Out of an initial set of around 1900 monolayers distributed over 32 different crystal structures, we find 350 in the most stable category. In addition to the 55 experimentally synthesised monolayers, this set also includes around 80 monolayers from experimentally known vdW layered bulk materials, and thus around 200 completely new and potentially synthesisable 2D materials.

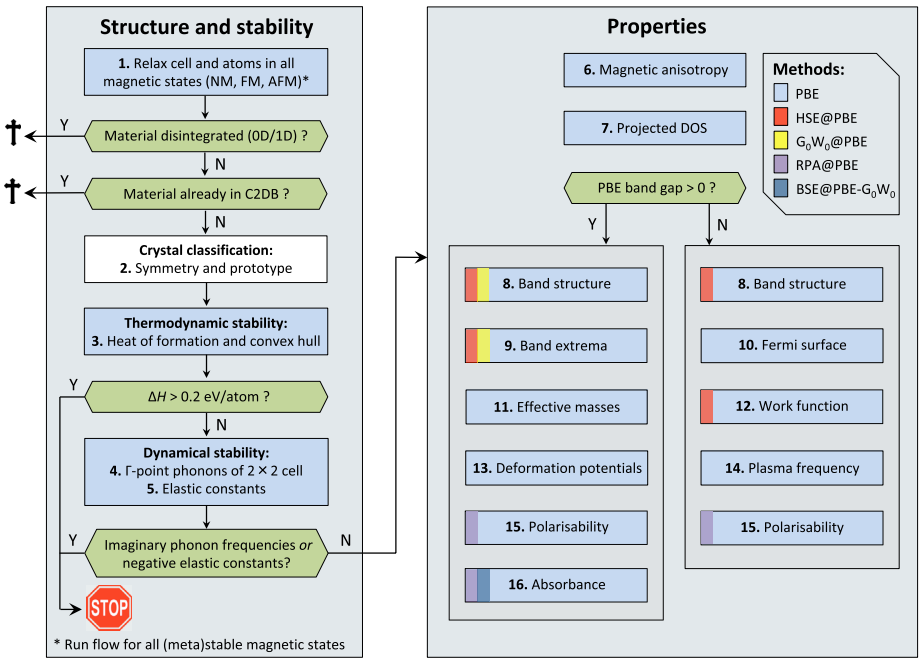

Figure 1. The workflow used to calculate the structure and properties of the materials in C2DB. The cross indicates that the material is not included in the database at all, while the stop sign indicates that no more of the workflow is performed.

In section 2, we describe the computational workflow behind the database. The structure and properties of the materials are calculated using well established state-of-the-art methodology. Technical descriptions of the different steps in the workflow are accompanied by illustrative examples and comparisons with literature data. Since *documentation and validation* is the main purpose of the section, we deliberately focus on well known 2D materials like the Xenes and transition metal dichalcogenides where plenty of both computational and experimental reference data is available. It should be clear that the novelty of the present work does not lie in the employed methodology nor in the type of materials properties that we calculate (we note, however, that to the best of our knowledge the present compilation of GW and BSE calculations represents the largest of its kind reported so far). The significance of our work is rather reflected by the fact that when large and consistently produced data sets are organised and made easily accessible, new scientific opportunities arise. As outlined below, this paper presents several examples of this effect.

In section 3 we give an overview of the materials and the data contained in the C2DB and provide some specific examples to illustrate its use. Using an extensive set of many-body G_0W_0 calculations as a reference, we establish the performance of various DFT xc-functionals for predicting band gaps, band edge positions, and band alignment at hetero-interfaces, and we propose an optimal strategy for obtaining accurate band energies at low computational cost. Similarly, the 250 BSE calculations allow us to explore trends in exciton binding energies and perform a statistically significant and unbiased assessment of the accuracy and limitations of the widely used Mott–Wannier model for 2D excitons. From the data on more than 600 semiconductor monolayers, we present strong empirical evidence against an often employed relation between effective masses and band gaps derived from $\mathbf{k}\cdot\mathbf{p}$ perturbation theory. Inspired by the potential of using 2D materials as building blocks for plasmonics and photonics, we propose a model to predict the plasmon dispersion relations in 2D metals from the (intraband) plasma frequency and the onset of interband transitions and use it to identify 2D metals with plasmons in the optical frequency regime. We propose several new magnetic 2D materials (including both metals and semiconductors) with ferromagnetic or anti-ferromagnetic ordering and significant out-of-plane magnetic anisotropy. Finally, we point to new high-mobility 2D semiconductors including some with band gaps in the range of interest for (opto)electronic applications.

In section 4 we provide our conclusions together with an outlook discussing some opportunities and possible future directions for the C2DB.

2. Workflow

The workflow used to generate the data in the C2DB is illustrated in figure 1. It consists of two parts: In the first part (left panel) the unit cell and atom positions

are optimised for different magnetic configurations: non-magnetic (NM), ferro-magnetic (FM) and antiferro-magnetic (AFM). Materials satisfying certain stability and geometry criteria (indicated by green boxes) are subject to the second part (right panel) where the different properties are computed using DFT and many-body methods. The G_0W_0 band structure and BSE absorbance calculations have been performed only for semiconducting materials with up to four atoms in the unit cell. Per default, properties shown in the online database include spin–orbit coupling (SOC); however, to aid comparison with other calculations, most properties are also calculated and stored without SOC.

All DFT and many-body calculations are performed with the projector augmented wave code GPAW [37] using plane wave basis sets and PAW potentials version 0.9.2. The workflow is managed using the Python based atomic simulation environment (ASE) [38]. We have developed a library of robust and numerically accurate (convergence verified) ASE-GPAW scripts to perform the various tasks of the workflow, and to create the database afterwards. The library is freely available, under a GPL license.

Below we describe all steps of the workflow in detail. As the main purpose is to document the workflow, the focus is on technical aspects, including numerical convergence and benchmarking. An overview of the most important parameters used for the different calculations is provided in table 1.

2.1. Structure relaxation

The workflow is initiated with a crystal structure defined by its unit cell (Bravais lattice and atomic basis). The crystal lattice is typically that of an experimentally known prototype (the 'seed structure') decorated with atoms picked from a subset of the periodic table, see figure 2. We refer to materials by the chemical formula of their unit cell followed by the crystal structure. The latter is indicated by a representative material of that prototype, as described in section 3.1. For example, monolayer MoS_2 in the hexagonal H and T phases are denoted MoS_2-MoS_2 and MoS_2-CdI_2, respectively. Now, MoS_2 is in fact not stable in the T phase, but undergoes a 2×1 distortion to the so-called T′ phase. Because the T′ phase is the thermodynamically stable phase of WTe_2, we denote MoS_2 in the distorted T phase by Mo_2S_4-WTe_2. In the following, we shall refer to the unit cell with which the workflow is initiated, i.e. the unit cell of the seed structure, as the primitive cell or the 1×1 cell, even if this cell is not dynamically stable for the considered material (see section 2.4).

The unit cell and internal coordinates of the atoms are relaxed in both a spin-paired (NM), ferromagnetic (FM), and anti-ferromagnetic (AFM) configuration. Calculations for the AFM configuration are performed only for unit cells containing at least two metal atoms. The symmetries of the initial seed structure are kept during relaxation. All relevant computational details are provided in table 1.

After relaxation, we check that the structure has remained a covalently connected 2D material and not disintegrated into 1D or 0D clusters. This is done by defining clusters of atoms using the covalent radius [39] + 30% as a measure for covalent bonds between atoms. The dimensionality of a cluster is obtained from the scaling of the number of atoms in a cluster upon repetition of the unit cell following the method described by Ashton *et al* [16]. Only materials containing exactly one cluster of dimensionality 2 are given further consideration (an exception is made for the metal-organic perovskites (prototype PbA_2I_4) for which the metal atom inside the octahedron represents a 0D cluster embedded in a 2D cluster). To illustrate the effect of the covalent radius + 30% threshold, figure 3 shows the distribution of the candidate structures in the database as a function of the covalent factor needed to fully connect the structure. Most materials have a critical covalent factor below 1.3 and fall in the green shaded region. There is, however, a tail of around 100 disconnected materials (red region); these materials are not included in the database (see first green box in figure 1).

We also check that the material is not already contained in the database (second green box in figure 1). This is done by measuring the root mean square distance (RMSD) [40] relative to all other materials in the C2DB with the same reduced chemical formula. A threshold of 0.01 Å is used for this test.

In case of multiple metastable magnetic configurations (in practice, if both a FM and AFM ground state are found), these are regarded as different phases of the same material and will be treated separately throughout the rest of the workflow. To indicate the magnetic phase we add the extensions 'FM' or 'AFM' to the material name. The total energy of the spin-paired ground state is always stored, even when it is not the lowest. If the energy of the non-magnetic state is higher than the most stable magnetic state by less than 10 meV/atom, the workflow is also performed for the non-magnetic state. This is done in recognition of the finite accuracy of DFT for predicting the correct energetic ordering of different magnetic states.

We have compared the lattice constants of 29 monolayers with those reported in [41], which were obtained with the VASP code using PBE and very similar numerical settings and find a mean absolute deviation of 0.024 Å corresponding to 0.4%. The small yet finite deviations are ascribed to differences in the employed PAW potentials.

2.2. Crystal structure classification

2.2.1. Symmetry

To classify the symmetries of the crystal structure the 3D space group is determined using the crystal

Table 1. Overview of the methods and parameters used for the different steps of the workflow. If a parameter is not specified at a given step, its value equals that of the last step where it was specified.

Workflow step(s)	Parameters
Structure and energetics (1–4)[a]	vacuum = 15 Å; k-point density = 6.0/Å^{-1}; Fermi smearing = 0.05 eV; PW cutoff = 800 eV; xc functional = PBE; maximum force = 0.01 eV/Å; maximum stress = 0.002 eV/Å^3; phonon displacement = 0.01Å
Elastic constants (5)	k-point density = 12.0/Å^{-1}; strain = ±1%
Magnetic anisotropy (6)	k-point density = 20.0/Å^{-1}; spin–orbit coupling = True
PBE electronic properties (7–10 and 12)	k-point density = 12.0/Å^{-1} (36.0/Å^{-1} for step 7)
Effective masses (11)	k-point density = 45.0/Å^{-1}; finite difference
Deformation potential (13)	k-point density = 12.0/Å^{-1}; strain = ±1%
Plasma frequency (14)	k-point density = 20.0/Å^{-1}; tetrahedral interpolation
HSE band structure (8–12)	HSE06@PBE; k-point density = 12.0/Å^{-1}
G_0W_0 band structure (8, 9)	G_0W_0@PBE; k-point density = 5.0/Å^{-1}; PW cutoff = ∞ (extrapolated from 170, 185 and 200 eV); full frequency integration; analytical treatment of $W(q)$ for small q; truncated Coulomb interaction
RPA polarisability (15)	RPA@PBE; k-point density = 20.0/Å^{-1}; PW cutoff = 50 eV; truncated Coulomb interaction; tetrahedral interpolation
BSE absorbance (16)	BSE@PBE with G_0W_0 scissors operator; k-point density = 20.0/Å^{-1}; PW cutoff = 50 eV; truncated Coulomb interaction; at least 4 occupied and 4 empty bands

[a] For the cases with convergence issues, we set a k-point density of 9.0 and a smearing of 0.02 eV.

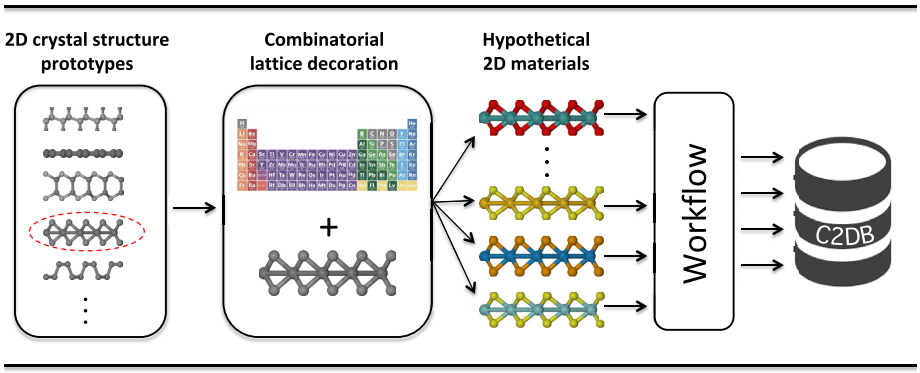

Figure 2. The materials in the C2DB are initially generated by decorating an experimentally known crystal structure prototype with atoms chosen from a (chemically reasonable) subset of the periodic table.

symmetry library Spglib [42] on the 3D supercell with a tolerance of 10^{-4} Å.

2.2.2. Prototypes

The materials are classified into crystal structure prototypes based on the symmetry of the crystals. For two materials to belong to the same prototype, we require that they have the same space group, the same stoichiometry, and comparable thicknesses. The last requirement is included to distinguish between materials with the same symmetry and stoichiometry but with different number of atomic layers, see for example monolayer BN and GaS in figure 4. Each prototype is labelled by a specific representative material. For prototypes which have been previously investigated, we comply with the established conventions. However, since the field of 2D materials is still young and because C2DB contains a large number of never-synthesised materials, some of the considered crystal structures fall outside the known prototypes. In these cases we have chosen the representative material to be the one with the lowest energy with respect to the convex hull. Some of the crystal structure prototypes presently contained in the C2DB are shown in figure 4.

2.3. Thermodynamic stability

The heat of formation, ΔH, is defined as the energy of the material with respect to the standard states of its constituent elements. For example, the heat of formation per atom of a binary compound, A_xB_y, is

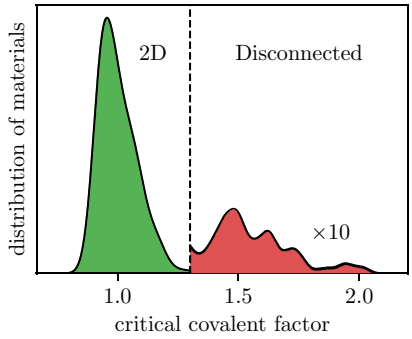

Figure 3. The distribution of candidate structures for the C2DB with respect to the critical covalent factor at which they become 2D. Materials in the red region are excluded from the database.

$$\Delta H = (E(A_xB_y) - xE(A) - yE(B))/(x+y), \quad (1)$$

where $E(A_xB_y)$ is the total energy of the material A_xB_y, and $E(A)$ and $E(B)$ are the total energies of the elements A and B in their standard state. When assessing the stability of a material in the C2DB, it should be kept in mind that the accuracy of the PBE functional for the heat of formation is only around 0.2 eV/atom on average [43]. Other materials databases, e.g. OQMD, Materials Project, and AFLOW, employ fitted elementary reference energies (FERE) [44] and apply a Hubbard U term [45] for the rare earth and transition metal atoms (or a selected subset of them). While such correction schemes in general improve ΔH they also introduce some ambiguity, e.g. the dataset from which the FERE are determined or the exact form of the orbitals on which the U term is applied. Thus in order not to compromise the transparency and reproducibility of the data we use the pure PBE energies.

For a material to be thermodynamically stable it is necessary but not sufficient that $\Delta H < 0$. Indeed, thermodynamic stability requires that ΔH be negative not only relative to its pure elemental phases but relative to all other competing phases, i.e. its energy must be below the *convex hull* [46]. We stress, however, that in general, but for 2D materials in particular, this definition cannot be directly applied as a criterion for stability and synthesisability. The most important reasons for this are (i) the intrinsic uncertainty on the DFT energies stemming from the approximate xc-functional (ii) substrate interactions or other external effects that can stabilise the monolayer (iii) kinetic barriers that separate the monolayer from other lower energy phases rendering the monolayer (meta)stable for all practical purposes.

We calculate the energy of the 2D material relative to the convex hull of competing bulk phases, ΔH_{hull}. The convex hull is currently constructed from the 2836 most stable binary bulk compounds which were obtained from the OQMD [24]. The energies of the bulk phases were recalculated with GPAW using the PBE xc-functional and the same numerical settings as applied for the 2D materials (but the structure was not re-optimised). Because the bulk reference structures from OQMD were optimised with the VASP code and with Hubbard U corrections for materials containing 3*d* elements, and because the PBE misses attractive vdW interaction, the bulk energies could be slightly overestimated relative to the monolayers. As a consequence, monolayers that also exist in a layered bulk phase could have $\Delta H_{\text{hull}} < 0$, even if the layered bulk phase is part of the convex hull and thus should be energetically more stable than the monolayer. Comparing our ΔH_{hull} values for 35 compounds with the exfoliation energies calculated in [18] employing vdW compliant xc-functionals for both bulk and monolayer, we estimate the errors in the convex hull energies to be below 0.1 eV/atom.

As an example, the convex hull for Fe_xSe_{1-x} is shown in figure 5. The convex hull as defined by the bulk binaries is indicated by the blue lines. The labels for the 2D materials refer to the crystal prototype and magnetic order. Clearly, most 2D materials lie above the convex hull and are thus predicted to be thermodynamically unstable in freestanding form under standard conditions. However, as mentioned above, depending on the material, errors on the PBE formation energies can be sizable and thus the hull diagram should only be taken as guideline. Nevertheless, in the present example we find that FeSe (which is itself a prototype) with anti-ferromagnetic ordering lies slightly below the convex hull and is thus predicted to be thermodynamically stable. This prediction is consistent with the recent experimental observation that monolayer FeSe deposited on $SrTiO_3$ exhibits AFM order [47].

2.4. Phonons and dynamic stability

Due to the applied symmetry constraints and/or the limited size of the unit cell, there is a risk that the structure obtained after relaxation does not represent a local minimum of the potential energy surface, but only a saddle point. We test for dynamical stability by calculating the Γ-point phonons of a 2×2 repeated cell (without re-optimising the structure) as well as the elastic constants (see section 2.5). These quantities represent second-order derivatives of the total energy with respect to atom displacements and unit cell lengths, respectively, and negative values for either quantity indicate a structural instability.

The Γ-point phonons of the 2×2 supercell are obtained using the finite displacement method [48]. We displace each atom in the primitive cell by ± 0.01 Å, and calculate the forces induced on all the atoms in the supercell. From the forces we construct the dynamical matrix, which is diagonalised to obtain the Γ-point phonons of the 2×2 cell (or equivalently the Γ-point and zone boundary phonons of the primitive cell). The eigenvalues of the dynamical matrix correspond to the

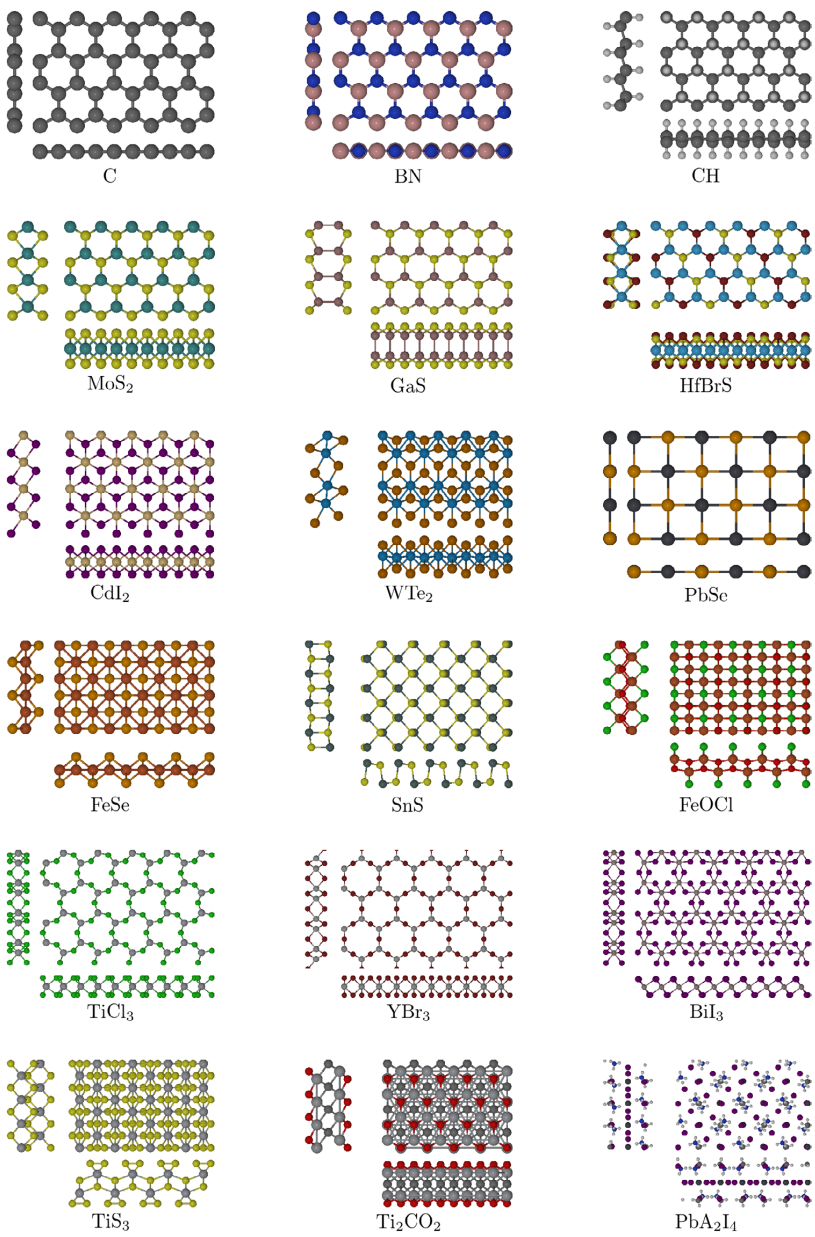

Figure 4. Examples of crystal structure prototypes currently included in the C2DB.

square of the mass-renormalised phonon frequencies, $\tilde{\omega}$. Negative eigenvalues are equivalent to imaginary frequencies and signal a saddle point.

Our procedure explicitly tests for stability against local distortions of periodicities up to 2×2 and thus provides a necessary, but not sufficient condition for dynamic stability. We stress, however, that even in cases where a material would spontaneously relax into a structure with periodicity larger than 2×2, the Γ-point dynamical matrix of the 2×2 cell could exhibit negative eigenvalues. Our test is thus more stringent than it might seem at first glance. In principle, a rigorous test for dynamic stability would require the calculation of the full phonon band structure. Mathematically, the instabilities missed by our approach are those that result in imaginary phonons in the interior of the BZ but *not* at the zone boundary. Physically, such modes could be out of plane buckling or charge density wave-driven reconstructions with periodicities of several unit cells. In general, however, these types of

instabilities are typically rather weak (as measured by the magnitude of the imaginary frequency) as compared to more local distortions such as the T to T′ distortion considered below. Moreover, they could well be a special property of the isolated monolayer and become stabilised by the ubiquitous interactions of the 2D material with its environment, e.g. substrates. This is in fact supported by the full phonon calculations by Mounet *et al* for $\sim$ 250 isolated monolayers predicted to be easily exfoliable from experimentally known layered bulk phases [18]. Indeed, most of the instabilities revealed by their calculations are of the type described above and would thus be missed by our test. However, these instabilities cannot be too critical as the monolayers are known to be stable in the vdW bonded layered bulk structure.

As an example, figure 6 compares the dynamical stability of a subset of transition metal dichalcogenides and -oxides in the T and T′ phases (CdI_2 and WTe_2 prototypes). The two upper panels show the smallest eigenvalue of the Γ-point dynamical matrix of the 2×2 cell. Only materials above the dashed line are considered dynamically stable (for this example we do not consider the sign of the elastic constants which could further reduce the set of dynamically stable materials). Since the unit cell of the T′ phase contains that of the T phase it is likely that a material initially set up in the T′ phase relaxes back to the T phase. To identify these cases, and thereby avoid the presence of duplicates in the database, the third panel shows the root mean square distance (RMSD) between the structures obtained after relaxations starting in the T- and T′ phase, respectively. Structures below the dashed line are considered identical. The color of each symbol refers to the four different potential energy surfaces illustrated at the bottom of the figure.

2.4.1. Stability criteria

To assess the stability of the materials in the C2DB, we turn to the set of experimentally synthesised/exfoliated monolayers. For these materials, the calculated energy above the convex hull and minimum eigenvalue of the dynamical matrix are shown on figure 7. It is clear that all but five known monolayers have a hull energy below 0.2 eV/atom, and three of these have only been synthesised on a metal substrate. Turning to the dynamical stability, all but one of the experimentally known monolayers have a minimum eigenvalue of the dynamical matrix above -2 eV Å^{-2}, and 70% have a minimum eigenvalue above -1×10^{-5} eV Å^{-2}.

Guided by these considerations, we assign each material in the C2DB a stability level (low, medium or high) for both dynamical and thermodynamic stability, as illustrated in table 2. For ease of reference, we also define the overall stability level of a given material as the lower of the dynamical and thermodynamic stability levels. If a material has 'low' overall stability (marked by bold in the table), we consider it unstable and do not carry out the rest of the workflow. Materials

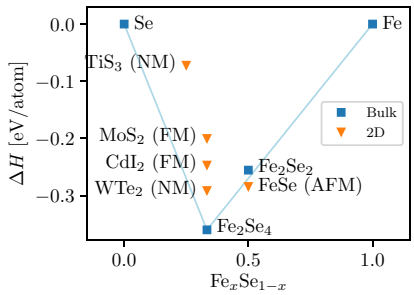

Figure 5. Convex hull for Fe_xSe_{1-x}. The convex hull as defined by the bulk phases is represented by the blue lines. Blue squares denote bulk binary reference phases while orange triangles represent 2D materials. The labels for the 2D materials refer to the crystal prototype and magnetic order.

with 'high' overall stability are considered likely to be stable and thus potentially synthesisable. Materials in the 'medium' stability category, while unlikely to be stable as freestanding monolayers, cannot be discarded and might be metastable and possible to synthesise under the right conditions. For example, freestanding silicene has a heat of formation of 0.66 eV/atom, but can be grown on a silver substrate. Likewise, the T′ phase of MoS_2 (WTe_2 prototype) has an energy of 0.27 eV/atom higher than the thermodynamically stable H phase, but can be stabilised by electron doping.

2.5. Elastic constants

The elastic constants of a material are defined by the generalised Hooke's law,

$$\sigma_{ij} = C_{ijkl}\varepsilon_{kl} \tag{2}$$

where σ_{ij}, C_{ijkl} and ε_{kl} are the stress, stiffness and strain tensors, respectively, and where we have used the Einstein summation convention. In two dimensions, the stress and strain tensors have three independent components, namely planar stress/strain in the x and y directions, as well as shear stress/strain. The stiffness tensor is a symmetric linear map between these two tensors, and therefore has up to six independent components. Disregarding shear deformations, the relationship between planar strain and stress is

$$\begin{bmatrix}\sigma_{xx}\\ \sigma_{yy}\end{bmatrix} = \begin{bmatrix}C_{11} & C_{12}\\ C_{12} & C_{22}\end{bmatrix}\begin{bmatrix}\epsilon_{xx}\\ \epsilon_{yy}\end{bmatrix}. \tag{3}$$

For all materials in the C2DB, we calculate the planar elastic stiffness coefficients C_{11}, C_{22}, and C_{12}. These are calculated using a central difference approximation to the derivative of the stress tensor: the material is strained along one of the coordinate axes, x or y, and the stress tensor is calculated after the ions have relaxed. We use strains of $\pm 1\%$ which we have found to be sufficiently large to eliminate effects of numerical

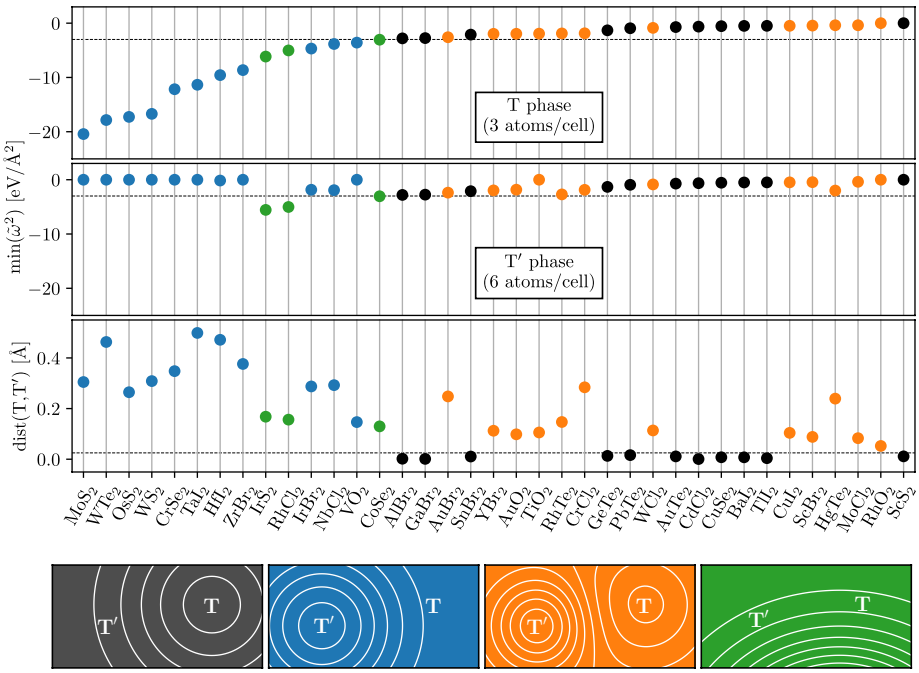

Figure 6. Dynamical stability of a set of transition metal dichalcogenides and -oxides in the T and T′ phases (CdI_2 and WTe_2 prototypes), respectively. The first and second panels show the minimum eigenvalue of the Γ-point dynamical matrix of the 2×2 unit cell (containing 12 and 24 atoms for the T and T′ phase, respectively. The lower panel shows the root mean square distance (RMSD) between the relaxed structures. The color indicates whether the material is dynamically stable in the T phase (black), the T′ phase (blue), both phases (orange) or neither of the phases (green).

noise and sufficiently small to stay within the linear response regime.

Table 3 shows the calculated planar stiffness coefficients of a set of 2D materials. As can be seen the values from the C2DB are in very good agreement with previously published PBE results. For the isotropic materials MoS_2, WSe_2 and WS_2, C_{11} and C_{22} should be identical, and we see a variation of up to 0.6%. This provides a test of how well converged the values are with respect to numerical settings.

2.6. Magnetic anisotropy

The energy dependence on the direction of magnetisation, or magnetic anisotropy (MA), arises from spin–orbit coupling (SOC). According to the magnetic force theorem [96] this can be evaluated from the eigenvalue differences such that the correction to the energy becomes

$$\Delta E(\hat{\mathbf{n}}) = \sum_{\mathbf{k}n} f(\varepsilon^{\hat{\mathbf{n}}}_{\mathbf{k}n})\varepsilon^{\hat{\mathbf{n}}}_{\mathbf{k}n} - \sum_{\mathbf{k}n} f(\varepsilon^{0}_{\mathbf{k}n})\varepsilon^{0}_{\mathbf{k}n}, \quad (4)$$

where $\varepsilon^{\hat{\mathbf{n}}}_{\mathbf{k}n}$ and $f(\varepsilon^{\hat{\mathbf{n}}}_{\mathbf{k}n})$ are the eigenenergies and occupation numbers, respectively, obtained by diagonalising the Kohn–Sham Hamiltonian including SOC in a basis of collinear spinors aligned along the direction $\hat{\mathbf{n}}$, while $\varepsilon^{0}_{\mathbf{k}n}$ and $f(\varepsilon^{0}_{\mathbf{k}n})$ are the bare Kohn–Sham eigenenergies and occupation numbers without SOC.

For all magnetic materials we have calculated the energy difference between out-of-plane and in-plane magnetisation $E_{\mathrm{MA}}(i) = \Delta E(\hat{\mathbf{z}}) - \Delta E(i)$, $(i = \hat{\mathbf{x}}, \hat{\mathbf{y}})$. Negative values of $E_{\mathrm{MA}}(i)$ thus indicate that there is an out-of-plane easy axis of magnetisation.

Calculations for the ground state have been performed with plane-wave cutoff and energetic convergence threshold set to 800 eV and 0.5 meV/atom respectively. For all calculations we have used a Γ-centered Monkhorst–Pack k-point with a density of $20/\mathrm{\AA}^{-1}$. The SOC contribution is introduced via a non-self-consistent diagonalisation of the Kohn–Sham Hamiltonian evaluated in the projector-augmented wave formalism [97].

2.7. Projected density of states

The projected density of states (PDOS) is a useful tool for identifying which atomic orbitals comprise a band. It is defined as

$$\rho^{S}_{l}(\varepsilon) = \sum_{a \in S} \sum_{\mathbf{k}n} \sum_{m} |\langle \phi^{a}_{l,m} | \psi_{\mathbf{k}n} \rangle|^2 \delta(\varepsilon - \varepsilon_{\mathbf{k}n}), \quad (5)$$

where $\psi_{\mathbf{k}n}$ are the Kohn–Sham wave functions with eigenvalues $\varepsilon_{\mathbf{k}n}$ and $\phi^{a}_{l,m}$ are the spin-paired Kohn–Sham orbitals of atomic species S with angular momentum l (s, p, d, f). We sum over all atoms belonging to species S so every atomic species has one

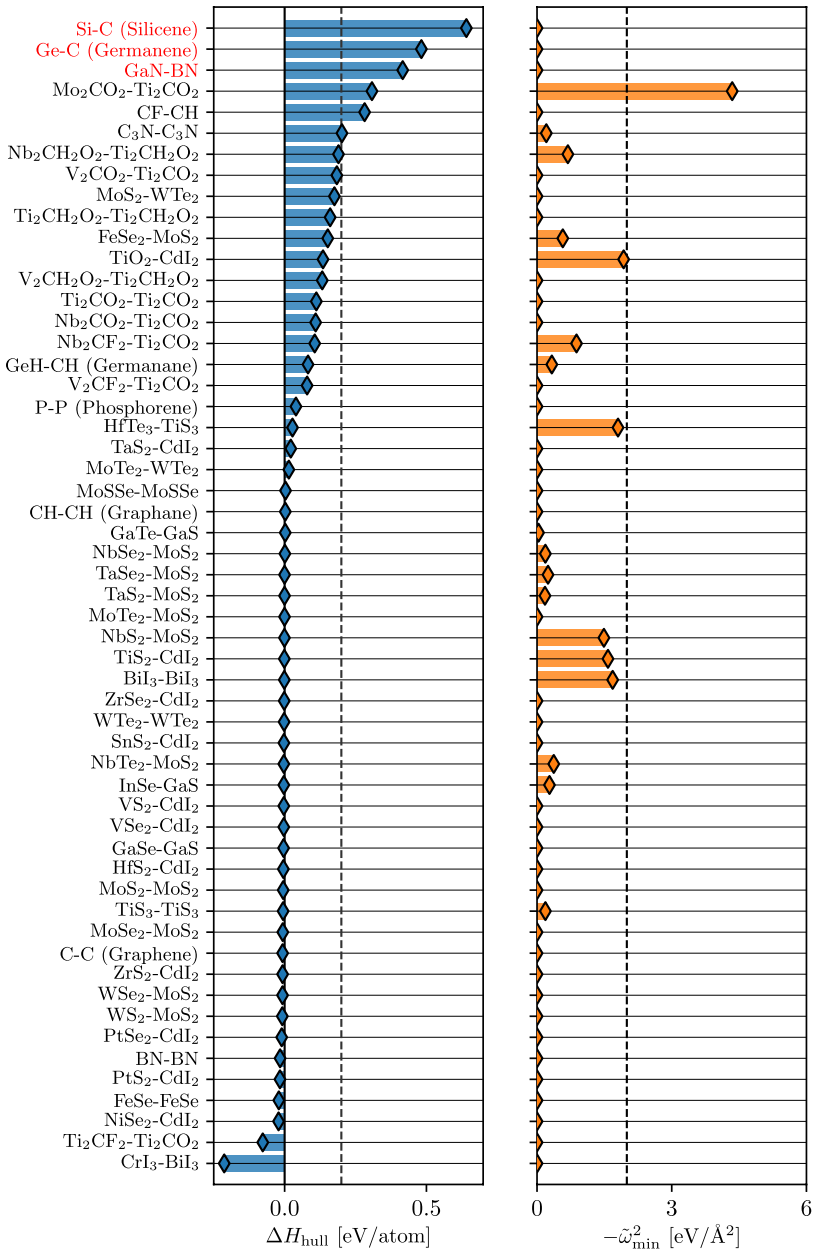

Figure 7. The calculated energy above the convex hull and minimum eigenvalue of the dynamical matrix (evaluated at the Γ-point for the 2 × 2 cell) for the 55 materials in the C2DB that have been synthesised or exfoliated in monolayer form, see [6, 9, 10, 12, 49–94]. The three materials highlighted in red have only been synthesised on metallic substrates. The black dashed lines indicate the thresholds used to categorise the thermodynamic and dynamic stability of materials in the C2DB.

entry per angular momentum channel. In the PAW formalism this can be approximated as

$$\rho_i^S(\varepsilon) = \sum_{a\in S}\sum_{\mathbf{k}n}\sum_{m} |\langle \tilde{p}^a_{l,m}|\tilde{\psi}_{\mathbf{k}n}\rangle|^2 \delta(\varepsilon - \varepsilon_{\mathbf{k}n}) \tag{6}$$

where $\tilde{\psi}_{\mathbf{k}n}$ are the pseudo wave functions and $\tilde{p}^a_{l,m}$ are the PAW projectors associated with the atomic orbitals $\phi^a_{l,m}$. The PDOS is calculated from equation (6) using linear tetrahedron interpolation [98] (LTI) of energy eigenvalues obtained from a ground state calculation with a k-point sampling of $36/\text{Å}^{-1}$. In contrast to other techniques for calculating the PDOS using smearing, the PDOS yielded by the LTI method returns exactly zero at energies with no states. Examples of PDOS

Table 2. The materials in the C2DB distributed over the nine stability categories defined by the three levels (high, medium and low) of dynamical stability (columns) and thermodynamic stability (rows). The overall stability of the materials is defined as the lower of the two separate stability scales. Materials with low overall stability (bold) are considered unstable.

Thermodynamic stability (eV/atom)	Dynamic stability (eVÅ^{-2})			
	$\lvert\tilde{\omega}^2_{\text{min}}\rvert > 2$ or $C_{ii} < 0$	$10^{-5} < \lvert\tilde{\omega}^2_{\text{min}}\rvert < 2, C_{ii} > 0$	$\lvert\tilde{\omega}^2_{\text{min}}\rvert < 10^{-5}, C_{ii} > 0$	Total
$\Delta H > 0.2$	**6.0%**	**4.2%**	**1.7%**	**12.0%**
$\Delta H < 0.2$	**14.9%**	10.9%	6.4%	32.2%
$\Delta H_{\text{hull}} < 0.2$	**11.4%**	24.1%	20.3%	55.8%
Total	**32.3%**	39.2%	28.5%	

Table 3. Planar elastic stiffness coefficients (in N m^{-1}) calculated at the PBE level. The results of this work are compared to previous calculations from the literature and the mean absolute deviation (MAD) is shown.

	C_{11} (N m^{-1})		C_{22} (N m^{-1})		C_{12} (N m^{-1})	
	C2DB	Literature	C2DB	Literature	C2DB	Literature
P (phosphorene)	101.9	105.2 [95]	25.1	26.2 [95]	16.9	18.4 [95]
MoS_2	131.4	132.6 [19]	131.3	132.6 [19]	32.6	32.7 [19]
WSe_2	120.6	119.5 [19]	121.3	119.5 [19]	22.8	22.7 [19]
WS_2	146.3	145.3 [19]	146.7	145.3 [19]	32.2	31.5 [19]
MAD	1.7	—	1.4	—	0.6	—

are shown in figure 9 (right) for respectively the ferromagnetic metal VO_2 and the semiconductor WS_2 in the H phase (MoS_2 prototype).

2.8. Band structures

Electronic band structures are calculated along the high symmetry paths shown in figure 8 for the five different types of 2D Bravais lattices. The band energies are computed within DFT using three different xc-functionals, namely PBE, HSE06, and GLLBSC. These single-particle approaches are complemented by many-body G_0W_0 calculations for materials with a finite gap and up to four atoms in the unit cell (currently around 250 materials). For all methods, SOC is included by non-selfconsistent diagonalisation in the full basis of Kohn–Sham eigenstates. Band energies always refer to the vacuum level defined as the asymptotic limit of the Hartree potential, see figure 12. Below we outline the employed methodology while section 3.2.1 provides an overview and comparison of the band energies obtained with the different methods.

2.8.1. PBE band structure

The electron density is determined self-consistently on a uniform k-point grid of density 12.0/Å^{-1}. From this density, the PBE band structure is computed non-selfconsistently at 400 k-points distributed along the band path (see figure 8). Examples of PBE band structures are shown in figure 9 for the ferromagnetic metal VO_2 and the semiconductor WS_2 both in the MoS_2 prototype structure. The expectation value of the out-of-plane spin component, $\langle\chi_{n\mathbf{k}\sigma}|\hat{S}_z|\chi_{n\mathbf{k}\sigma}\rangle$, is evaluated for each spinorial wave function, $\chi_{n\mathbf{k}\sigma} = (\psi_{n\mathbf{k}\uparrow}, \psi_{n\mathbf{k}\downarrow})$, and is indicated by the color of the band. For materials with inversion symmetry, the SOC cannot induce band splitting, meaning that $\langle\chi_{n\mathbf{k}\sigma}|\hat{S}_z|\chi_{n\mathbf{k}\sigma}\rangle$ is ill-defined and no color coding is used. The band structure without SOC is indicated by a dashed grey line. We have compared our PBE + SOC band gaps of 29 different monolayers with those obtained with the VASP code in [41] and find a mean absolute deviation of 0.041 eV.

2.8.2. HSE band structure

The band structure is calculated non-selfconsistently using the range-separated hybrid functional HSE06 [99] on top of a PBE calculation with k-point density 12.0/Å^{-1} and 800 eV plane wave cutoff. We have checked for selected systems that the HSE band structure is well converged with these settings. The energies along the band path are obtained by spline interpolation from the uniform k-point grid. As an example, the HSE band structure of WS_2 is shown in the left panel of figure 10 (black line) together with the PBE band structure (grey dashed). The PBE band gap increases from 1.52 eV to 2.05 eV with the HSE06 functional in good agreement with earlier work reporting band gaps of 1.50 eV (PBE) and 1.90 eV (HSE) [100] and 1.55 eV (PBE) and 1.98 eV (HSE) [101], respectively. A more systematic comparison of our results with the HSE + SOC band gaps obtained with the VASP code in [41] for 29 monolayers yield a mean absolute deviation of 0.14 eV. We suspect this small but non-zero deviation is due to differences in the employed PAW potentials and the non-selfconsistent treatment of the HSE in our calculations.

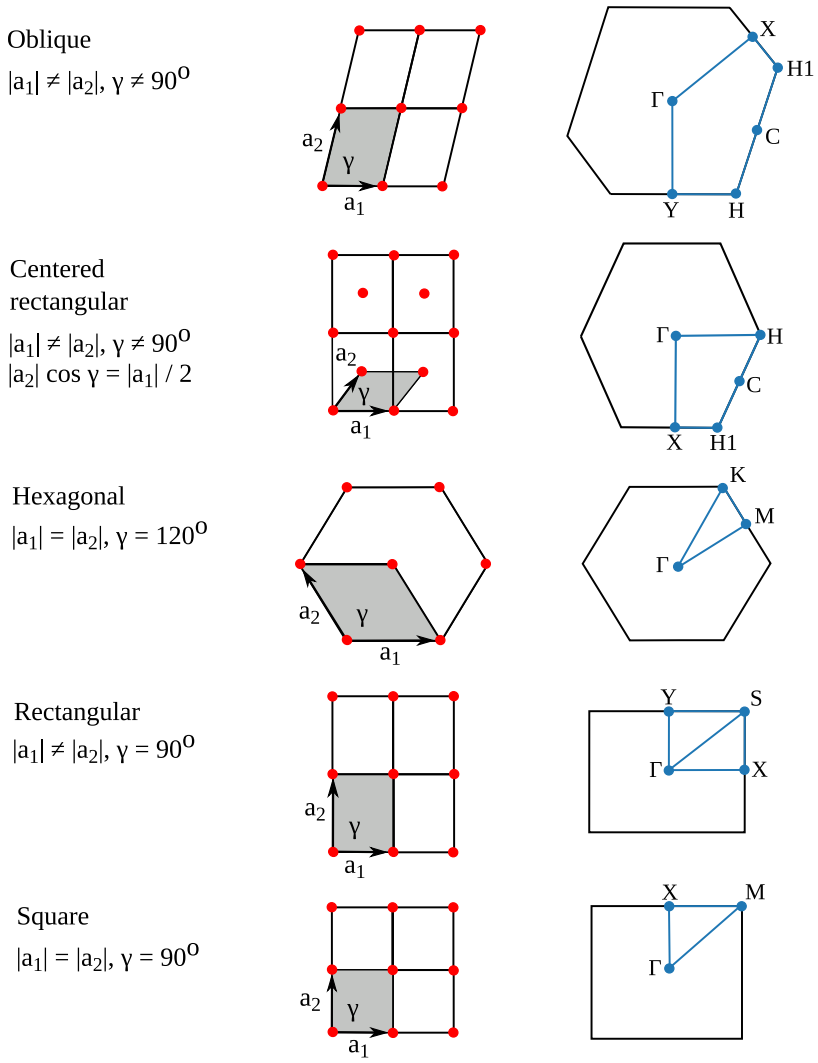

Figure 8. Overview of the five 2D Bravais lattices and corresponding Brillouin zones. The unit vectors $\mathbf{a}_1$ and $\mathbf{a}_2$ are shown together with the angle between them γ. The primitive unit cell is indicated in gray. High symmetry points of the BZ and the path along which the band structure is evaluated, are indicated in blue.

2.8.3. GLLBSC fundamental gap

For materials with a finite PBE band gap, the fundamental gap (i.e. the difference between the ionisation potential and electron affinity) also sometimes referred to as the quasiparticle gap, is calculated self-consistently using the GLLBSC [102] xc-functional with a Monkhorst–Pack *k*-point grid of density 12.0/Å^{-1}. The GLLBSC is an orbital-dependent exact exchange-based functional, which evaluates the fundamental gap as the sum of the Kohn–Sham gap and the xc-derivative discontinuity, $E_{\mathrm{gap}} = \varepsilon^{\mathrm{KS}}_{\mathrm{gap}} + \Delta_{\mathrm{xc}}$. The method has been shown to yield excellent quasiparticle band gaps at very low computational cost for both bulk [102, 103] and 2D semiconductors [36].

In the exact Kohn–Sham theory, $\varepsilon^{\mathrm{KS}}_{\mathrm{v}}$ should equal the exact ionisation potential and thus Δ_{xc} should be used to correct only the conduction band energies [104]. Unfortunately, we have found that in practice this procedure leads to up-shifted band energies (compared with the presumably more accurate G_0W_0 results, see figure 20). Consequently, we store only the fundamental gap and Δ_{xc} in the database. However, as will be shown in section 3.2.1 the center of the gap is in fact reasonably well described by PBE suggesting that efficient and fairly accurate predictions of the absolute

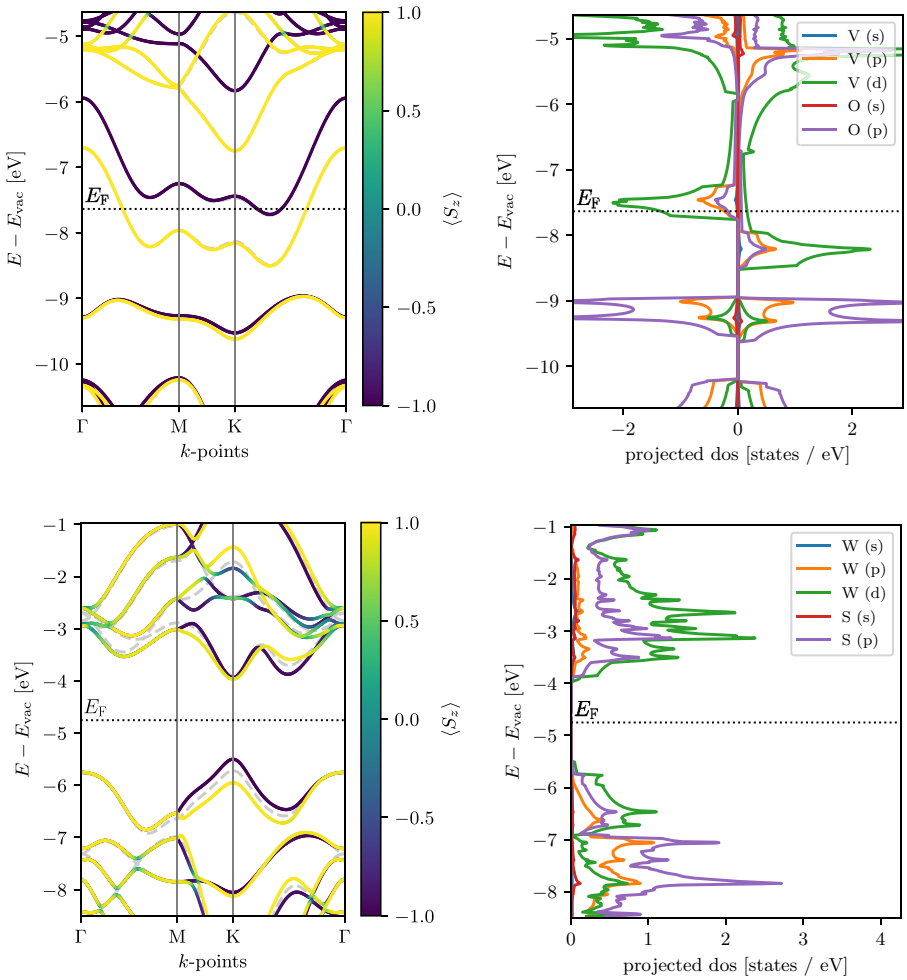

Figure 9. Band structure (left) and projected density of states (right) for VO_2 (top) and WS_2 (bottom) in the MoS_2 prototype, calculated with the PBE xc-functional. The z-component of the spin is indicated by the color code on the band structure.

band edge energies can be obtained by a symmetric GLLBSC correction of the PBE band edges.

2.8.4. G_0W_0 band structure

For materials with finite PBE band gap the quasiparticle (QP) band structure is calculated using the G_0W_0 approximation on top of PBE following our earlier work [105, 106]. Currently, this resource demanding step is performed only for materials with up to four atoms in the unit cell. The number of plane waves and the number of unoccupied bands included in the calculation of the non-interacting density response function and the GW self-energy are always set equal. The individual QP energies are extrapolated to the infinite basis set limit from calculations at plane wave cutoffs of 170, 185 and 200 eV, following the standard $1/N_G$ dependence [107, 108], see figure 11 (right). The screened Coulomb interaction is represented on a non-linear real frequency grid ranging from 0 eV to 230 eV and includes around 250 frequency points. The exchange contribution to the self-energy is calculated using a Wigner–Seitz truncation scheme [109] for a more efficient treatment of the long range part of the exchange potential. For the correlation part of the self-energy, a 2D truncation of the Coulomb interaction is used [110, 111]. We stress that the use of a truncated Coulomb interaction is essential to avoid unphysical screening from periodically repeated layers which otherwise leads to significant band gap reductions.

Importantly, the use of a truncated Coulomb interaction leads to much slower k-point convergence because of the strong q-dependence of the 2D dielectric function around $q = 0$. We alleviate this problem by using an analytical expression for the screened interaction when performing the BZ integral around $q = 0$ [106]. This allows us to obtain well converged results with a relatively low k-point density of 5.0/Å^{-1} (corresponding to

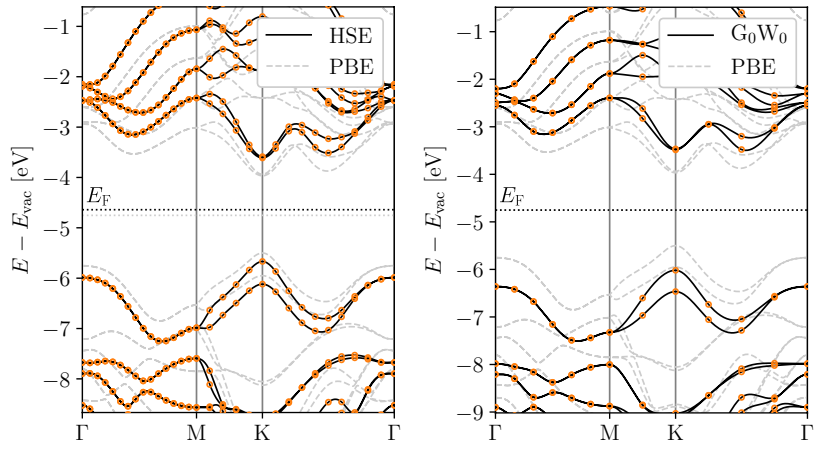

Figure 10. Band structure of WS_2 calculated with the HSE06 functional (left) and G_0W_0 (right). For comparison the PBE result is also shown (grey dashed). Spin–orbit coupling (SOC) is included in all calculations. The band energies refer to the vacuum level. The points show the calculated eigenvalues from which the band structure is interpolated. The relatively coarse k-point grid used for G_0W_0 is justified by the analytical treatment of the screened interaction $W(q)$ around $q = 0$, see figure 11.

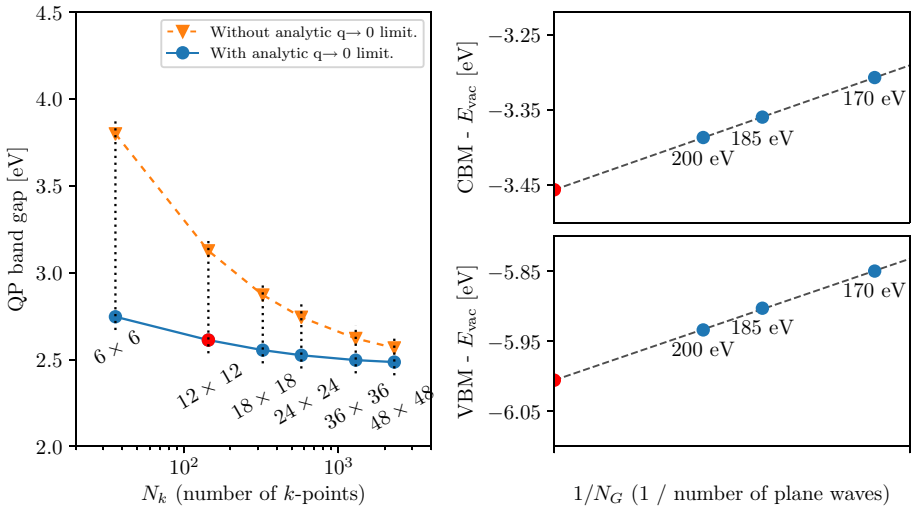

Figure 11. Left: Convergence of the QP band gap of MoS_2 as a function of k-point sampling with and without the analytical treatment of $W(q)$ around $q = 0$. It is clear that the analytical treatment of the screened interaction significantly improves the k-point convergence. Right: The convergence of the CBM and VBM versus the number of plane waves. The band energies are obtained by extrapolation of three calculations performed with PW cutoff up to 200 eV. In all panels, the red dot indicates the data point calculated by the workflow and available in the C2DB.

12×12 k-points for MoS_2). For example, with this setting the G_0W_0 band gap of MoS_2 is converged to within 0.05 eV, see figure 11 (left). In comparison, standard BZ sampling with no special treatment of the $q = 0$ limit, requires around 40×40 k-points to reach the same accuracy.

Figure 10 (right) shows the PBE and G_0W_0 band structures of WS_2 (including SOC). The G_0W_0 self-energy opens the PBE band gap by 1.00 eV and the HSE gap by 0.47 eV, in good agreement with previous studies [112]. We note in passing that our previously published G_0W_0 band gaps for 51 monolayer TMDCs [36] are in good agreement with the results obtained using the workflow described here. The mean absolute error between the two data sets is around 0.1 eV and can be ascribed to the use of PBE rather than LDA as starting point and the use of the analytical expression for W around $q = 0$.

A detailed comparison of our results with previously published G_0W_0 data is not meaningful because

Table 4. Comparison between calculated and experimental band gaps for four freestanding monolayers. The experimental values have been corrected for substrate screening. MAD refers to the mean absolute deviation between the predicted values and the measured values.

	Band gap (eV)				
Material	PBE	HSE06	GLLBSC	G_0W_0	Experiment
MoS_2	1.58	2.09	2.21	2.53	2.50 [125]
$MoSe_2$	1.32	1.80	1.88	2.12	2.31 [126]
WS_2	1.53	2.05	2.16	2.53	2.72 [127]
P (phosphorene)	0.90	1.51	1.75	2.03	2.20 [124]
MAD w.r.t. experiment	1.10	0.57	0.43	0.15	—

of the rather large differences in the employed implementations/parameter settings. In particular, most reported calculations do not employ a truncated Coulomb interaction and thus suffer from spurious screening effects, which are then corrected for in different ways. Moreover, they differ in the amount of vacuum included the supercell, the employed *k*-point grids and basis sets, the in-plane lattice constants, and the DFT starting points. For example, published values for the QP band gap of monolayer MoS_2 vary from from 2.40 to 2.90 eV [113–120] (see [119] for a detailed overview). The rather large variation in published GW results for 2D materials is a result of the significant numerical complexity of such calculations and underlines the importance of establishing large and consistently produced benchmark data sets like the present.

For bulk materials, self-consistency in the Green's function part of the self-energy, i.e. the GW_0 method, has been shown to increase the G_0W_0 band gaps and improve the agreement with experiments [121]. The trend of band gap opening is also observed for 2D materials [106, 120, 120, 122], however, no systematic improvement with respect to experiments has been established [122]. For both bulk and 2D materials, the fully self-consistent GW self-energy systematically overestimates the band gap [121, 122] due to the neglect of vertex corrections [122, 123]. In G_0W_0 the neglect of vertex corrections is partially compensated by the smaller band gap of the non-interacting Kohn–Sham Green's function compared to the true interacting Green's function. In this case, the vertex corrections corrections will affect mainly the absolute position of the bands relative to vacuum while the effect on the band gap is relatively minor [122].

In table 4 we compare calculated band gaps from C2DB with experimental band gaps for three monolayer TMDCs and phosphorene. The experimental data has been corrected for substrate interactions [122, 124], but not for zero-point motion, which is expected to be small (<0.1 eV). The G_0W_0 results are all within 0.2 eV of the experiments. A further (indirect) test of the G_0W_0 band gaps against experimental values is provided by the comparison of our BSE spectra against experimental photoluminescence data in table 7, where we have used a G_0W_0 scissors operator. Finally, we stress that the employed PAW potentials are not norm-conserving, and this can lead to errors for bands with highly localised states (mainly 4*f* and 3*d* orbitals), as shown in [108]. Inclusion of vertex corrections and use of norm conserving potentials will be the focus of future work on the C2DB.

2.9. Band extrema

For materials with a finite band gap, the positions of the valence band maximum (VBM) and conduction band minimum (CBM) within the BZ are identified together with their energies relative to the vacuum level. The latter is defined as the asymptotic value of the electrostatic potential, see figure 12. The PBE electrostatic potential is used to define the vacuum level in the non-selfconsistent HSE and G_0W_0 calculations. For materials with an out-of-plane dipole moment, a dipole correction is applied during the selfconsistent DFT calculation, and the vacuum level is defined as the average of the asymptotic electrostatic potentials on the two sides of the structure. The PBE vacuum level shift is also stored in the database.

2.10. Fermi surface

The Fermi surface is calculated using the PBE xc-functional including SOC for all metallic compounds in the database. Based on a ground state calculation with a *k*-point density of at least $20/\text{Å}^{-1}$, the eigenvalues are interpolated with quadratic splines and plotted within the first BZ. Figure 13 (left) shows an example of the Fermi surface for VO_2-MoS_2 with color code indicating the out-of-plane spin projection $\langle S_z \rangle$. The band structure refers to the ferromagnetic ground state of VO_2-MoS_2, which has a magnetic moment of 0.70 μ_B per unit cell, characterised by alternating spin-polarised lobes with $\langle S_z \rangle = \pm 1$.

2.11. Effective masses

For materials with a finite PBE gap, the effective electron and hole masses are calculated from the PBE eigenvalues; initially these are calculated on an ultrafine *k*-point mesh of density $45.0/\text{Å}^{-1}$ uniformly distributed inside a circle of radius $0.015\ \text{Å}^{-1}$ centered at the VBM and CBM, respectively. The radius is chosen to be safely above the noise level of the calculated eigenvalues but still within the harmonic regime; it corresponds to a spread of eigenvalues of about 1 meV within the circle for an effective mass of 1 m_0. For each band within an energy window of 100 meV above/below the CBM/VBM, the band

curvature is obtained by fitting a third order polynomial. Even though the masses represent the second derivative of the band energies, we have found that the inclusion of 3rd order terms stabilises the fitting procedure and yields masses that are less sensitive to the details of the employed k-point grids. For each band the mass tensor is diagonalised to yield heavy and light masses in case of anisotropic band curvatures. The masses (in two directions) and the energetic splitting of all bands within 100 meV of the band extremum are calculated both with and without SOC and stored in the database. Other approaches exist for calculating effective masses, such as $\mathbf{k}\cdot\mathbf{p}$ perturbation theory (see e.g. [128] and references therein); the present scheme was chosen for its simplicity and ease of application to a wide range of different materials.

In addition to the effective masses at the VBM and CBM, the exciton reduced mass is calculated by applying the above procedure to the direct valence-conduction band transition energies, $\varepsilon_{v-c}(\mathbf{k}) = \varepsilon_c(\mathbf{k}) - \varepsilon_v(\mathbf{k})$. For direct band gap materials the exciton reduced mass is related to the electron and hole masses by $1/\mu_{ex} = 1/m_e^* + 1/m_h^*$, but in the more typical case of indirect band gaps, this relation does not hold.

As an example, figure 14 shows a zoom of the band structure of SnS-GeSe around the VBM and CBM (upper and lower panels). The second order fits to the band energies (extracted from the fitted 3rd order polynomial) are shown by red dashed lines. It can be seen that both the conduction and valence bands are anisotropic leading to a heavy and light mass direction (left and right panels, respectively). The valence band is split by the SOC resulting in two bands separated by ~ 10 meV and with slightly different curvatures. The conduction band exhibits a non-trivial band splitting in one of the two directions. The peculiar band splitting is due to a Rashba effect arising from the combination of spin–orbit coupling and the finite perpendicular electric field created by the permanent dipole of the SnS structure where Sn and S atoms are displaced in the out of plane direction leading to a sizable vacuum level difference of 1.13 eV, see figure 12.

Table 5 shows a comparison between selected effective masses from the C2DB and previously published data also obtained with the PBE xc-correlation functional and including SOC. Overall, the agreement is very satisfactory.

2.12. Work function

For metallic compounds, the work function is obtained as the difference between the Fermi energy and the asymptotic value of the electrostatic potential in the vacuum region, see figure 12. The work function is determined for both PBE and HSE band structures (both including SOC) on a uniform k-point grid of density $12.0/\text{Å}^{-1}$. Since the SOC is evaluated non-selfconsistently, the Fermi energy is adjusted afterwards based on a charge neutrality condition.

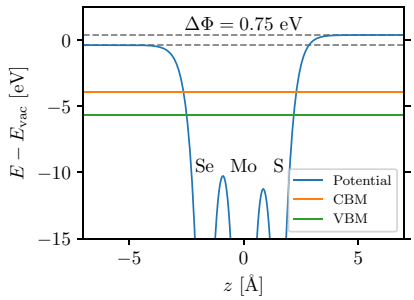

Figure 12. Electrostatic potential profile perpendicular to monolayer MoSSe (averaged in plane). The position of the VBM and CBM are indicated together with the splitting of the vacuum levels caused by the out-of-plane dipole moment of the MoSSe layer.

2.13. Deformation potentials

For semiconductors, the deformation potentials quantify the shift in band edge energies (VBM or CBM) upon a linear deformation of the lattice. The uniaxial absolute deformation potential along axis i ($i = x, y$) is defined as [129, 130]

$$D_{ii}^{\alpha} = \frac{\Delta E_{\alpha}}{\varepsilon_{ii}}, \quad \alpha = \text{VBM, CBM} \tag{7}$$

where ΔE_{α} is the energy shift upon strain and ε_{ii} are the strains in the i-directions.

The deformation potentials are important physical quantities as they provide an estimate of the strength of the (acoustic) electron-phonon interaction, see section 3.2.2. Moreover, they are obviously of interest in the context of strain-engineering of band gaps and they can be used to can be used to infer an error bar on the band gap or band edge positions due to a known or estimated error bar on the lattice constant.

The calculation of D_{ii}^{α} is based on a central difference approximation to the derivative. A strain of $\pm$ 1% is applied separately in the x and y directions and the ions are allowed to relax while keeping the unit cell fixed. Calculations are performed with the PBE xc-functional, a plane wave cutoff of 800 eV, and a k-point density of $12/\text{Å}^{-1}$.

The change in band energy, ΔE_{α}, is measured relative to the vacuum level. In cases with nearly degenerate bands, care must be taken to track the correct bands as different bands might cross under strain. In this case, we use the expectation value $\langle \hat{S}_z \rangle$ to follow the correct band under strain. Figure 15 shows how the band structure of MoS_2 changes as a function of strain. Both the VBM and the CBM shift down (relative to the vacuum level) when tensile strain is applied in the x direction, but the conduction band shows a much larger shift, leading to an effective band gap closing under tensile strain.

Table 6 shows a comparison between the deformation potentials in the C2DB, and literature values obtained using similar methods. There is generally

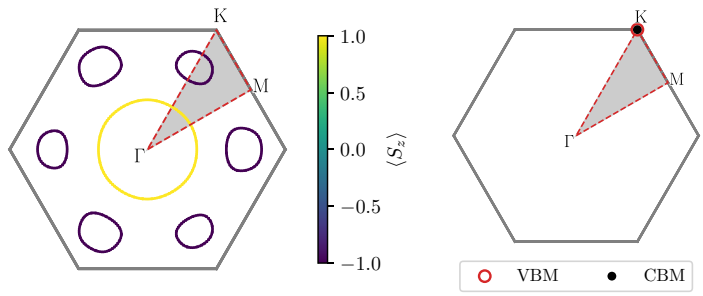

Figure 13. Left: Brillouin zone and Fermi surface calculated with PBE and spin–orbit coupling for VO_2 in the MoS_2 crystal structure. The Fermi surface is colored by the spin projection along the z-axis. Right: Brillouin zone, valence band maximum (VBM) and conduction band minimum (CBM) for WS_2 in the MoS_2 crystal structure. The grey areas in both plots mark the irreducible Brillouin zone.

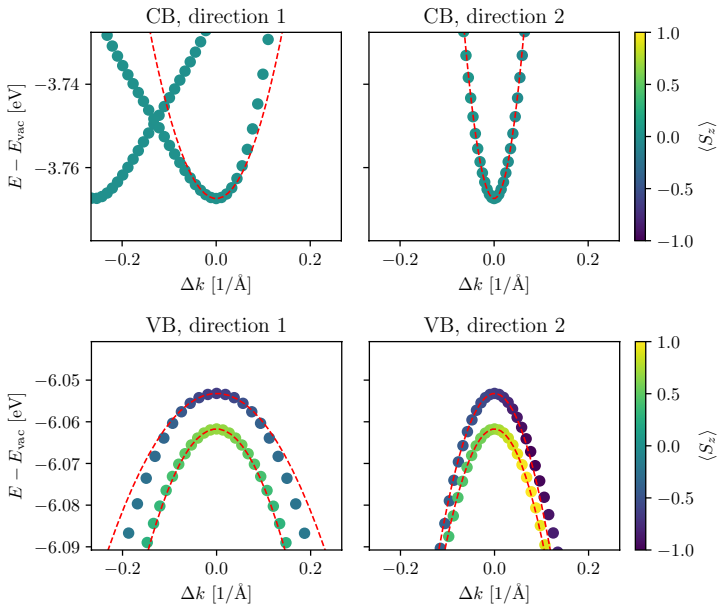

Figure 14. Zoom of the band structure of SnS in the GeSe crystal structure around the conduction and valence band extrema (upper and lower panels). Second order fits used to determine the effective masses are shown by red dashed lines. The peculiar band splitting in the conduction band minimum (upper left panel) is caused by a Rashba effect arising from the combination of spin–orbit coupling and the finite perpendicular electric field created by the asymmetric SnS structure.

Table 5. Calculated PBE effective masses (in units of m_0), for the highest valence band and lowest conduction band, for different 2D materials. All C2DB values are calculated including spin–orbit coupling.

		Electron mass (m_0)		Hole mass (m_0)	
Material	k-point	C2DB	Literature	C2DB	Literature
MoS_2	K	0.42	0.44 [128]	0.53	0.54 [128]
WSe_2	K	0.46	0.40 [128]	0.35	0.36 [128]
Phosphorene (zig-zag)	Γ	1.24	1.24 [95]	6.56	6.48 [95]
Phosphorene (armchair)	Γ	0.14	0.13 [95]	0.13	0.12 [95]
MAD		0.02	—	0.03	—

Table 6. Absolute deformation potentials (in eV) of the VBM and CBM for different materials. All results are based on the PBE xc-functional.

		Valence band		Conduction band	
Material	k-point	C2DB	Ref. [131]	C2DB	Ref. [131]
$MoSe_2$	K	−1.43	−1.86	−5.57	−5.62
WS_2	K	−1.25	−1.59	−6.66	−6.76
WSe_2	K	−1.21	−1.43	−6.21	−6.35
hBN	K	−1.57	−1.63	−4.55	−4.62
MAD		0.26	—	0.14	—

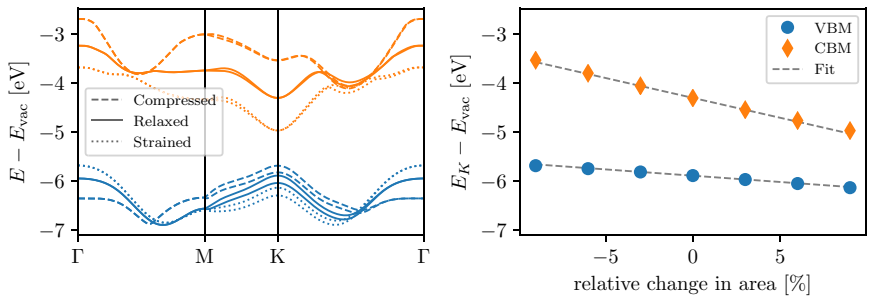

Figure 15. Left: Valence- and conduction bands of MoS_2 for ±4.5% biaxial strain. Right: Energies of the VBM and CBM at the K point as function of strain. The symbols are the results of full DFT calculations, while the dashed lines are obtained from the deformation potentials evaluated at ±1% strain.

good agreement, and part of the discrepancy can be ascribed to the fact that, in contrast to [131], our numbers include spin–orbit coupling.

2.14. Plasma frequencies

The dielectric response of a 2D material is described by its 2D polarisability, α^{2D} (see section 2.15 for a general introduction of this quantity). For metals, it can be separated into contributions from intraband and interband transitions, i.e. $\alpha^{2D} = \alpha^{2D,intra} + \alpha^{2D,inter}$. We have found that local field effects (LFEs) are negligible for the intraband component, which consequently can be treated separately and evaluated as an integral over the Fermi surface. Specifically, this leads to the Drude expression for the polarisability in the long wave length limit $\alpha^{2D,intra}(\omega) = -\omega_{P,2D}^2/(2\pi\omega^2)$ where $\omega_{P,2D}$ is the 2D plasma frequency, which in atomic units is given by

$$\omega_{P,2D}^2 = \frac{4\pi}{A}\sum_{sn\mathbf{k}} |\hat{\mathbf{q}}\cdot\mathbf{v}_{sn\mathbf{k}}|^2 \delta(\varepsilon_{sn\mathbf{k}} - \varepsilon_F), \qquad (8)$$

where $\mathbf{v}_{sn\mathbf{k}} = \langle sn\mathbf{k}|\hat{\mathbf{p}}/m_0|sn\mathbf{k}\rangle$ is a velocity matrix element (with m_0 the electron mass), $\hat{\mathbf{q}} = \mathbf{q}/q$ is the polarisation direction, $s, n, \mathbf{k}$ denote spin, band and momentum indices, and A is the supercell area. The 2D plasma frequency is related to the conventional 3D plasma frequency by $\omega_{P,2D}^2(\omega) = \omega_{P,3D}^2(\omega)L/2$ where L is the supercell height.

The plasma frequency defined above determines the intraband response of the 2D metal to external fields. In particular, it determines the dispersion relation of plasmon excitations in the metal. The latter are defined by the condition $\varepsilon^{2D}(\omega_P) = 1 + 2\pi q\alpha^{2D}(\omega_P) = 0$, where q is the plasmon wave vector. Neglecting interband transitions (the effect of which is considered in section 3.2.4), the 2D plasmon dispersion relation becomes

$$\omega_P(q) = \omega_{P,2D}\sqrt{q}. \qquad (9)$$

The plasma frequencies, $\omega_{P,2D}$, for polarisation in the x and y directions, respectively, are calculated for all metals in the C2DB using the linear tetrahedron method [98] to interpolate matrix elements and eigenvalues based on a PBE band structure calculation with a k-point density of $20/\text{Å}^{-1}$.

2.15. Electronic polarisability

The polarisability tensor α_{ij} is defined by

$$P_i(\mathbf{q},\omega) = \sum_j \alpha_{ij}(\mathbf{q},\omega)E_j(\mathbf{q},\omega), \qquad (10)$$

where P_i is the i'th component of the induced polarisation averaged over a unit cell and E_j is the j'th component of the macroscopic electric field. Using that $P_i = (D_i - E_i)/(4\pi) = \sum_j(\epsilon_{ij} - \delta_{ij})E_j/(4\pi)$ one observes that $\alpha_{ij} = (\epsilon_{ij} - \delta_{ij})/(4\pi)$, where ϵ_{ij} is the dielectric function. In contrast to the dielectric function, whose definition for a 2D material is not straightforward [119], the polarisability allows for a natural generalisation to 2D by considering the induced dipole moment per unit area,

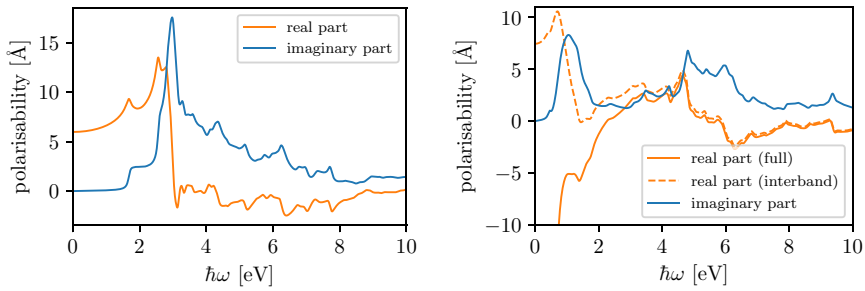

Figure 16. Real and imaginary part of the RPA in-plane polarisability of monolayer MoS_2 in the H phase (left) and the metallic monolayer NbS_2 in the T phase (right). For metals, the real part is shown both with and without the intraband contributions.

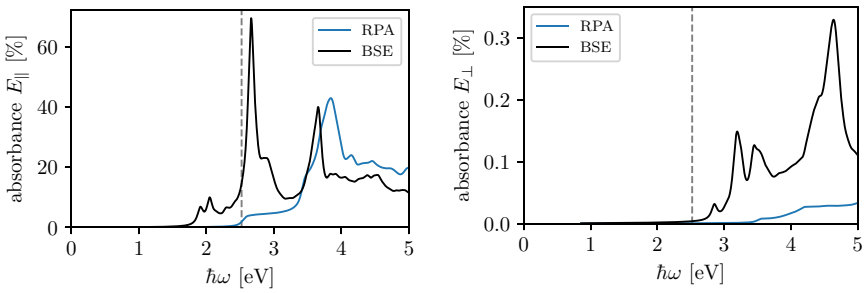

Figure 17. Optical absorbance of MoS_2 obtained with the RPA and BSE methods. Left: Electric field polarisation parallel to the layer. The lowest energy part of the BSE spectrum is composed of two excitonic peaks separated by 0.15 eV, which originates from the spin–orbit splitting in the valence band at K. Right: Electric field polarised perpendicular to the layer.

$$P_i^{2D}(\mathbf{q},\omega) = \sum_j \alpha_{ij}^{2D}(\mathbf{q},\omega)E_j(\mathbf{q},\omega). \tag{11}$$

Since the P_i is a full unit cell average and P_i^{2D} is integrated in the direction orthogonal to the slab, we have $P_i^{2D} = LP_i$ and $\alpha_{ij}^{2D} = L\alpha_{ij}$, where L is the length of the unit cell in the direction orthogonal to the slab.

In the following, we focus on the longitudinal components of the polarisability and dielectric tensors, which are simply denoted by α and ϵ. These are related to the density-density response function, χ, via the relations

$$\alpha^{2D}(\mathbf{q},\omega) = \frac{L}{4\pi}(\epsilon(\mathbf{q},\omega) - 1), \tag{12}$$

$$\epsilon^{-1}(\mathbf{q},\omega) = 1 + \langle v_c(\mathbf{q})\chi(\omega)\rangle_{\mathbf{q}}, \tag{13}$$

where v_c is the Coulomb interaction and

$$\langle v_c\chi(\omega)\rangle_{\mathbf{q}} = \frac{1}{V}\int_{\text{Cell}} d\mathbf{r}d\mathbf{r}'d\mathbf{r}'' v_c(\mathbf{r},\mathbf{r}')\chi(\mathbf{r}',\mathbf{r}'',\omega)e^{-i\mathbf{q}(\mathbf{r}-\mathbf{r}'')}, \tag{14}$$

where Cell is the supercell with volume V. The response function, χ, satisfies the Dyson equation [132] $\chi = \chi^{\text{irr}} + \chi^{\text{irr}}v_c\chi$, where χ^{irr} is the irreducible density-density response function. In the random phase approximation (RPA) χ^{irr} is replaced by the non-interacting response function, χ^0, whose plane wave representation is given by [133, 134]

$$\chi^0_{\mathbf{GG}'}(\mathbf{q},\omega) = \frac{1}{\Omega}\sum_{\mathbf{k}\in\text{BZ}}\sum_{mn}(f_{n\mathbf{k}} - f_{m\mathbf{k}+\mathbf{q}}) \times \frac{\langle\psi_{n\mathbf{k}}|e^{-i(\mathbf{q}+\mathbf{G})\cdot\mathbf{r}}|\psi_{m\mathbf{k}+\mathbf{q}}\rangle\langle\psi_{m\mathbf{k}+\mathbf{q}}|e^{i(\mathbf{q}+\mathbf{G}')\cdot\mathbf{r}}|\psi_{n\mathbf{k}}\rangle}{\hbar\omega + \varepsilon_{n\mathbf{k}} - \varepsilon_{m\mathbf{k}+\mathbf{q}} + i\eta}, \tag{15}$$

where $\mathbf{G}, \mathbf{G}'$ are reciprocal lattice vectors and Ω is the crystal volume.

For all materials in the database, we calculate the polarisability within the RPA for both in-plane and out-of-plane polarisation in the optical limit $\mathbf{q} \to 0$. For metals, the interband contribution to the polarisability is obtained from equation (15) while the intraband contribution is treated separately as described in section 2.14. The single-particle eigenvalues and eigenstates used in equation (15) are calculated with PBE, a k-point density of $20/\text{Å}^{-1}$ (corresponding to a k-point grid of 48×48 for MoS_2 and 60×60 for graphene), and 800 eV plane wave cutoff. The Dyson equation is solved using a truncated Coulomb potential [105, 111] to avoid spurious interactions from neighboring images. We use the tetrahedron method to interpolate the eigenvalues and eigenstates and a peak broadening of $\eta = 50$ meV. Local field effects are accounted for by including $\mathbf{G}$-vectors up to 50 eV. For the band summation we include 5 times as many unoccupied bands as occupied bands, which roughly corresponds to an

energy cutoff of 50 eV. The calculations are performed without spin–orbit coupling.

In figure 16 we show the real and imaginary part of α^{2D} for the semiconductor MoS_2. The PBE band gap of this material is 1.6 eV and we see the onset of dissipation at that energy. We also see that the initial structure of Im α is a constant, which is exactly what would be expected from the density of states in a 2D material with parabolic dispersion. Finally, we note that the static polarisability Re $\alpha|_{\omega=0} \approx 6$Å, which can easily be read off the figure. The polarisability is also shown for the metallic 1T-NbS_2 where we display the real part with and without the intraband Drude contribution $\omega_{P,2D}^2/(\hbar\omega + i\eta)^2$.

2.16. Optical absorbance

The power absorbed by a 2D material under illumination of a monochromatic light field with polarisation $\hat{\mathbf{e}}$ is quantified by the dimensionless absorbance:

$$\mathrm{Abs}(\omega) = 4\pi\omega\alpha^{2D}(q\hat{\mathbf{e}} \to 0, \omega)/c, \qquad (16)$$

where c is the speed of light. In section 2.15 we gave a prescription for evaluating α^{2D} in the RPA. However, absorption spectra of 2D semiconductors often display pronounced excitonic effects, which are not captured by the RPA. The Bethe–Salpeter equation (BSE) is a well-known method capable of describing excitonic effects and has been shown to provide good agreement with experimental absorption spectra for a wide range of materials [135].

For materials with finite band gap and up to four atoms per unit cell, we have calculated the RPA and the BSE absorption spectra for electric fields polarised parallel and perpendicular to the layers. The calculations are performed on top of PBE eigenstates and eigenvalues with spin–orbit coupling included and all unoccupied band energies shifted by a constant in order to reproduce the G_0W_0 quasiparticle gap (the scissors operator method). If the G_0W_0 gap is not available we use the GLLBSC gap for non-magnetic materials and the HSE gap for magnetic materials (since GLLBSC is not implemented in GPAW for spin-polarised systems). The screened interaction entering the BSE Hamiltonian is calculated within the RPA using a non-interacting response function evaluated from equation (15) with local field effects (i.e. **G**-vectors) included up to 50 eV and 5 times as many unoccupied bands as occupied bands for the sum over states. We apply a peak broadening of $\eta = 50$ meV and use a truncated Coulomb interaction. The BSE Hamiltonian is constructed from the four highest occupied and four lowest unoccupied bands on a k-point grid of density of $20/\text{Å}^{-1}$, and is diagonalised within the Tamm–Dancoff approximation. We note that the Tamm–Dancoff approximation has been found to be very accurate for bulk semiconductors [136]. For monolayer MoS_2 we have checked that it reproduces the full solution of the BSE, but its general validity for 2D materials, in particular those with small band gaps, should be more thoroughly tested.

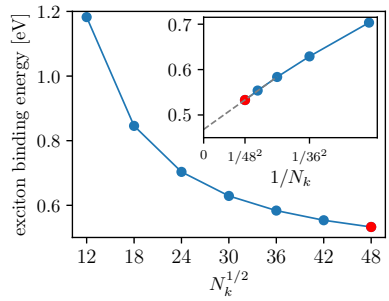

Figure 18. Convergence of the binding energy of the lowest exciton in monolayer MoS_2 obtained from a BSE calculation as a function of k-point mesh. The quasiparticle energies entering the BSE Hamiltonian are obtained from a fully converged PBE calculation with a scissors operator applied to match the G_0W_0 band gap. The red point represents the k-point sampling applied in the database, which is seen to overestimate the extrapolated exciton binding energy by ∼0.06 eV (inset).

In figure 17 we show the optical absorption spectrum of MoS_2 obtained with the electric field polarised parallel and perpendicular to the layer, respectively. Both RPA and BSE spectra are shown (the in-plane RPA absorbance equals the imaginary part of the RPA polarisability, see figure 16 (left), apart from the factor $4\pi\omega$ and the scissors operator shift). The low energy part of the in-plane BSE spectrum is dominated by a double exciton peak (the so-called A and B excitons) and is in excellent agreement with experiments [55].

In general, calculations of electronic excitations of 2D materials converge rather slowly with respect to k-points due to the non-analytic behavior of the dielectric function in the vicinity of $q = 0$ [119, 137, 138]. In figure 18 we show the k-point dependence of the binding energy of the A exciton in MoS_2 obtained as the difference between the direct band gap and the position of the first peak in figure 17. We observe a strong overestimation of the exciton binding energy at small k-point samplings, which converges slowly to a value of ∼0.5 eV at large k-point samplings. For 48×48 k-points, corresponding to the k-point sampling used for the BSE calculations in the database, the exciton binding energy is 0.53 eV, whereas a $1/N_k^2$ extrapolation to infinite k-point sampling gives 0.47 eV (see inset in figure 18). In general, the exciton binding energy decreases with increasing k-point sampling, and thus the exciton binding energies reported in the C2DB might be slightly overestimated. However, since G_0W_0 band gaps also decrease when the k-point sampling is increased (see figure 11) the two errors tend to cancel such that the absolute position of the absorption peak from BSE-G_0W_0 converges faster than the band gap or exciton binding energy alone.

Table 7. Comparison between calculated and experimental positions of the first excitonic peak for four different transition metal dichalcogenide monolayers and phosphorene.

	Energy of the first bright exciton (eV)	
Material	BSE@PBE-G_0W_0	Experiment
MoS_2	2.00	1.83 [140], 1.86 [141], 1.87 [142]
$MoSe_2$	1.62	1.57 [140], 1.57 [143], 1.58 [144]
WS_2	2.07	1.96 [141], 2.02 [144]
WSe_2	1.71	1.64 [142], 1.66 [143]
P (phosphorene)	1.45	1.45 [145], 1.75 [146]
MAD w.r.t. experiment	0.066	—

The BSE-G_0W_0 method has previously been shown to provide good agreement with experimental photoluminescence and absorption measurements on 2D semiconductors. In table 7 we show that our calculated position of the first excitonic peak agree well with experimental observations for four different TMDCs and phosphorene. Experimentally, the monolayers are typically supported by a substrate, which may alter the screening of excitons. However the resulting decrease in exciton binding energies is largely cancelled by a reduced quasiparticle gap such that the positions of the excitons are only slightly red-shifted as compared with the case of pristine monolayers [139].

3. Database overview

Having described the computational workflow, we now turn to the content of the database itself. We first present a statistical overview of all the materials in the C2DB (i.e. without applying any stability filtering) by displaying their distribution over crystal structure prototypes and their basic properties. We also provide a short list with some of the most stable materials, which to our knowledge have not been previously studied. Next, the predicted stability of the total set of materials is discussed and visualised in terms of the descriptors for thermodynamic and dynamic stability introduced in section 2.4.1. In section 3.2 we analyse selected properties in greater detail focusing on band gaps and band alignment, effective masses and mobility, magnetic properties, plasmons, and excitons. Throughout the sections we explore general trends and correlations in the data and identify several promising materials with interesting physical properties.

3.1. Materials

In table 8 we list the major classes of materials currently included in the database. The materials are grouped according to their prototype, see section 2.2.2. For each prototype we list the corresponding space group, the total number of materials, and the number of materials satisfying a range of different conditions. The atomic structure of some of the different prototypes were shown in figure 4. The vast majority of the 2D materials that have been experimentally synthesised in monolayer form are contained in the C2DB (the 55 materials in figure 7 in addition to seven metal-organic perovskites). These materials are marked in the database and a literature reference is provided. Additionally, 80 of the monolayers in the C2DB could potentially be exfoliated from experimentally known layered bulk structures [16–19]. These materials are also marked and the ID of the bulk compound in the relevant experimental crystal structure database is provided.

To illustrate how all the materials are distributed in terms of stability, we show the energy above the convex hull plotted against $\tilde{\omega}^2_{\mathrm{min}}$ in figure 19. It can be seen that the structures naturally sort themselves into two clusters according to the dynamic stability. The points have been colored according to the three levels for dynamic stability introduced in section 2.4. The lower panel shows the distribution of the materials in the grey region on a linear scale. While most of the experimentally known materials (red and black dots) have high dynamic stability, a significant part of them fall into the medium stability category. The marginal distributions on the plot show that the more dynamically stable materials are also more thermodynamically stable. The mean energy above the convex hull is 0.12 eV for the materials with high dynamical stability, while it is 0.25 eV for the others.

In table 9 we show the key properties of a selected set of stable materials, distributed across a variety of different crystal structure prototypes. To our knowledge, these materials are not experimentally known, and they are therefore promising candidates further study and experimental synthesis.

3.2. Properties: example applications

In the following sections we present a series of case studies focusing on different properties of 2D materials including band gaps and band alignment, effective masses and mobility, magnetic order, plasmons and excitons. The purpose is not to provide an in-depth nor material specific analysis, but rather to explore trends and correlations in the data and showcase some potential applications of the C2DB. Along the way, we report some of the novel candidate materials revealed by this analysis, which could be interesting to explore closer in the future.

Table 8. Overview of the materials currently in the C2DB. The table shows the number of compounds listed by their crystal structure prototype and selected properties. $E_{gap} > 0$ and 'direct gap' refer to the PBE values, 'high stability' refers to the stability scale defined in section 2.4.1, and the last three columns refer to the magnetic state, see section 2.1. In this overview, separate magnetic phases of the same structure are considered different materials.

		Number of materials						
Prototype	Symmetry	Total	$E_{gap} > 0$	Direct gap	High stability	NM	FM	AFM
C	P6/mmm	4	4	3	1	4	0	0
CH	P$\bar{3}$m1	8	7	6	1	8	0	0
CH_2Si	P3m1	2	2	2	1	2	0	0
BN	P$\bar{3}$m2	10	9	5	1	10	0	0
GaS	P$\bar{3}$m2	125	34	95	8	100	18	7
FeSe	P4/nmm	103	13	90	26	74	18	11
GeSe	P3m1	20	19	5	6	20	0	0
PbSe	P4/mmm	44	6	38	1	33	8	3
P	Pmna	9	9	0	1	9	0	0
MoS_2	P$\bar{3}$m2	241	85	176	53	156	85	0
CdI_2	P$\bar{3}$m1	315	95	231	90	218	80	17
WTe_2	$P2_1/m$	75	29	48	34	57	13	5
FeOCl	Pmmn	443	92	385	65	328	63	52
MoSSe	P3m1	9	6	6	5	8	1	0
C_3N	P6/mmm	25	1	24	0	25	0	0
YBr_3	P6/mmm	57	11	51	0	21	24	12
$TiCl_3$	P$\bar{3}$2m	69	35	51	2	32	23	14
BiI_3	P$\bar{3}$m1	123	69	66	15	48	54	21
TiS_3	Pmmn	34	8	28	5	31	2	1
$MnTe_3$	$P2_1/m$	29	3	27	1	22	4	3
Cr_3WS_8	Pmm2	35	34	18	8	35	0	0
$CrWS_4$	Pmm2	18	17	7	8	18	0	0
Ti_2CO_2	P$\bar{3}$m1	28	8	20	12	19	6	3
$Ti_2CH_2O_2$	P$\bar{3}$m1	13	3	12	3	10	2	1
Ti_3C_2	P$\bar{3}$m2	12	0	12	0	7	5	0
$Ti_3C_2O_2$	P$\bar{3}$m2	26	0	26	0	20	6	0
$Ti_3C_2H_2O_2$	P$\bar{3}$m2	14	0	14	0	10	4	0
PbA_2I_4	P1	27	27	27	0	27	0	0
Sum		1918	626	151	347	1352	416	150

3.2.1. *Band gaps and band alignment*

The band gaps and band edge positions of all semiconductors and insulators in the C2DB have been calculated with the PBE, HSE06, and GLLBSC xc-functionals while G_0W_0 calculations have been performed for the ∼250 simplest materials. The relatively large size of these datasets and the high degree of consistency in the way they are generated (all calculations performed with the same code using same PAW potentials and basis set etc) provide a unique opportunity to benchmark the performance of the different xc-functionals against the more accurate G_0W_0 method.

Figure 20 compares the size and center of the band gaps obtained with the density functionals to the G_0W_0 results. Relative to G_0W_0 the PBE functional underestimates the gaps by 45%, i.e. on average the PBE values must be scaled by 1.83 to reproduce the G_0W_0 results. The HSE06 band gaps are closer to G_0W_0 but are nevertheless systematically underestimated by more than 20%. On the other hand, GLLBSC shows very good performance with band gaps only 2% smaller than G_0W_0 on average. Table 10 shows the mean absolute deviations of the DFT methods relative to G_0W_0. We note that although GLLBSC provides an excellent description of the G_0W_0 band gaps *on average* the spread is sizable with a mean absolute deviation of 0.4 eV.

We note a handful of outliers in figure 20 with large HSE band gaps compared to PBE and G_0W_0. For one of these, namely the ferromagnetic $CoBr_2$-CdI_2, we obtain the band gaps: 0.30 eV (PBE), 3.41 eV (HSE), and 0.91 eV (G_0W_0). For validation, we have performed GPAW and QuantumEspresso calculations with the norm-conserving HGH pseudopotentials and plane wave cutoff up to 1600 eV. The converged band gaps are 0.49 eV (GPAW-HGH-PBE), 0.51 eV (QE-HGH-PBE) and 3.69 eV (GPAW-HGH-HSE), 3.52 eV (QE-HGH-HSE), which are all in reasonable

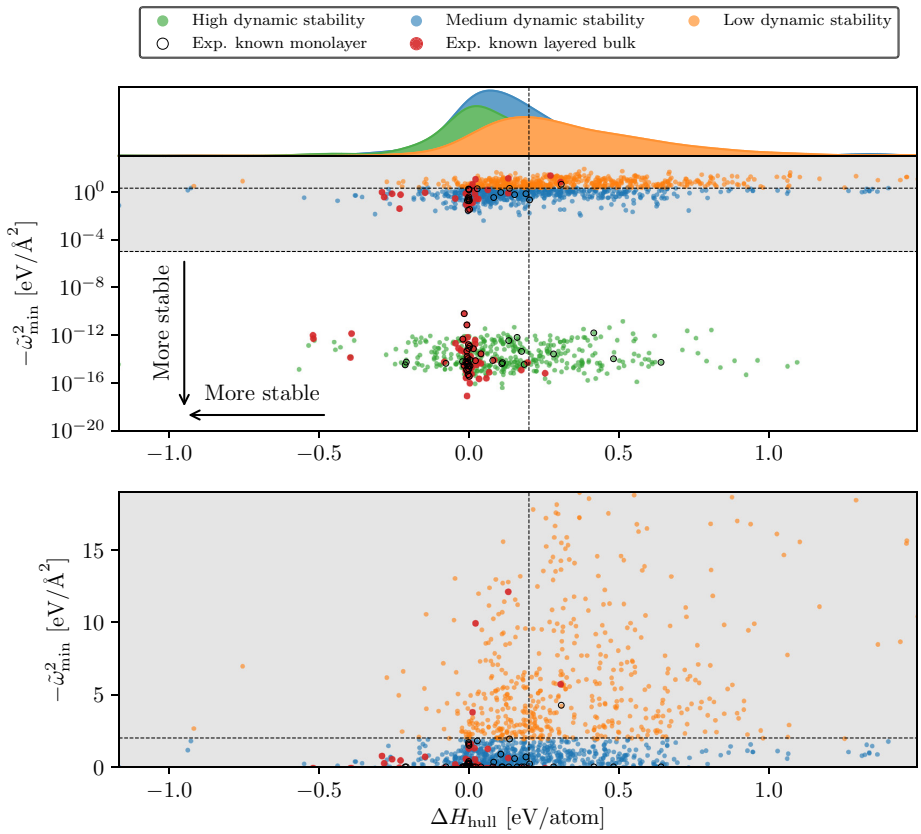

Figure 19. The dynamic stability of the candidate materials as a function of the energy above the convex hull on a log scale (top), and a linear scale (bottom). Experimentally synthesised monolayers are circled in black, while the known layered 3D structures are marked in red. The three different dynamic stability levels are indicated both by the horizontal dashed lines and the color of the points. The upper panel shows the marginal distribution of the energy over the convex hull for the points in each of the three stability levels.

agreement with the C2DB results. It should be interesting to explore the reason for the anomalous behavior of the HSE band gap in these materials.

Compared to the band gaps, the gap centers predicted by PBE and HSE06 are in overall better agreement with the G_0W_0 results. This implies that, on average, the G_0W_0 correction of the DFT band energies is symmetric on the valence and conduction band. In contrast, the GLLBSC predicts less accurate results for the gap center. This suggests that an accurate and efficient prediction of absolute band energies is obtained by combining the GLLBSC band gap with the PBE band gap center.

Next, we consider the band alignment at the interface between different 2D materials. Assuming that the bands line up with a common vacuum level and neglecting hybridisation/charge transfer at the interface, the band alignment is directly given by the VBM and CBM positions relative to vacuum.

We focus on pairs of 2D semiconductors for which the G_0W_0 band alignment is either Type II ($\Delta E > 0$) or Type III ($\Delta E < 0$), see figure 21 (left). Out of approximately 10 000 bilayers predicted to have Type II band alignment by G_0W_0, the PBE and HSE06 functionals predict qualitatively wrong band alignment (i.e. Type III) in 44% and 21% cases, respectively (grey shaded areas). In particular, PBE shows a sizable and systematic underestimation of ΔE as a direct consequence of the underestimation of the band gaps in both monolayers.

3.2.2. *Effective masses and mobilities*

The carrier mobility relates the drift velocity of electrons or holes to the strength of an applied electric field and is among the most important parameters for a semiconductor material. In general, the mobility is a sample specific property which is highly dependent on the sample purity and geometry, and (for 2D materials) interactions with substrate or embedding layers. Here we consider the phonon-limited mobility, which can be considered as the intrinsic mobility of the material, i.e. the mobility that would be measured in the absence of any sample specific- or external scattering sources.

The effective masses of the charge carriers have been calculated both with and without SOC for ∼600 semiconductors. Figure 22 shows the electron mass plotted against the hole mass. The data points are scat-

Table 9. Key properties of selected stable materials in the C2DB, which have not been previously synthesised. The calculated properties are the magnetic state, formation energy, energy above the convex hull, work function, PBE gap and and the nature of the gap (direct or indirect).

Prototype	Formula	Magnetic state	ΔH (eV)	ΔH_{hull} (eV)	Φ (eV)	PBE gap (eV)	Direct gap
BiI_3	VI_3	FM	−0.51	−0.15	5.3		
	$CoCl_3$	NM	−0.65	−0.21		1.13	No
	$CoBr_3$	NM	−0.41	−0.16		0.96	No
	CoI_3	NM	−0.14	−0.14		0.53	No
CdI_2	FeO_2	FM	−1.14	−0.36	7.31		
	$MnSe_2$	FM	−0.47	−0.18	5.09		
	MnS_2	FM	−0.57	−0.12	5.74		
	PdO_2	NM	−0.40	−0.08		1.38	No
	$CaBr_2$	NM	−2.09	−0.02		4.86	No
FeOCl	RhClO	NM	−0.65	−0.18	5.49		
	NiClO	AFM	−0.64	−0.17	6.32		
	NiBrO	AFM	−0.52	−0.16	5.78		
	ScIS	NM	−1.68	−0.14		1.66	Yes
FeSe	CoSe	FM	−0.27	0.02	4.22		
	RuS	NM	−0.38	0.05	4.72		
	MnSe	AFM	−0.50	−0.20		0.90	No
	MnS	AFM	−0.64	−0.19		0.78	No
GaS	AlSe	NM	−0.72	−0.02		2.00	No
	AlS	NM	−0.89	0.00		2.09	No
GeSe	GeSe	NM	−0.19	0.04		2.22	No
	GeS	NM	−0.22	0.05		2.45	No
	GeTe	NM	−0.01	0.09		1.47	No
	SnSe	NM	−0.33	0.10		2.15	No
MoS_2	VS_2	FM	−0.88	−0.02	5.95		
	$ScBr_2$	FM	−1.59	−0.40		0.16	No
	YBr_2	FM	−1.73	−0.23		0.34	No
	$FeCl_2$	FM	−0.67	−0.16		0.35	Yes
	$TiBr_2$	NM	−1.14	−0.04		0.76	No
	$ZrBr_2$	NM	−1.34	−0.04		0.83	No
Ti_2CO_2	Zr_2CF_2	NM	−2.36	−0.08	3.92		
	Hf_2CF_2	NM	−2.26	0.03	3.62		
	Y_2CF_2	NM	−2.50	−0.17		1.12	No
WTe_2	NbI_2	NM	−0.37	0.04	3.01		
	$HfBr_2$	NM	−1.16	−0.18		0.85	No
	$OsSe_2$	NM	−0.17	0.00		0.57	No

tered, with no clear correlation between the electron and hole masses. Overall, the electron masses are generally slightly smaller than the hole masses. The mean electron mass is 0.9 m_0, while the mean hole mass is 1.1 m_0, and 80% of the electron masses are below m_0 while the fraction is only 65% for the holes. This is not too surprising, since, on average, the energetically lower valence band states are expected to be more localised and thus less dispersive than the conduction band states.

The right panel of figure 22 shows the effective mass for electrons and holes plotted as a function of the inverse band gap. It can be seen that there is no clear correlation between the two quantities, which is confirmed by calculating the cross-correlation coefficient: for both electrons and holes it is less than 0.02. This provides empirical evidence against the linear relation between effective masses and inverse band gaps derived from $\mathbf{k} \cdot \mathbf{p}$ perturbation theory. The relation is based on the assumption that the perturbative expansion is dominated by the conduction and valence band and that the momentum matrix element between these states, $\langle u_c | \hat{\mathbf{p}} | u_v \rangle$, does not vary too much as function of the considered parameter (here the type of material). These assumptions clearly do not hold across a large set of different semiconductors. If we focus on a specific class of materials, e.g. sulfides in the MoS_2 structure indicated by the highlighted symbols, we see a slightly improved trend but still with significant fluctuations.

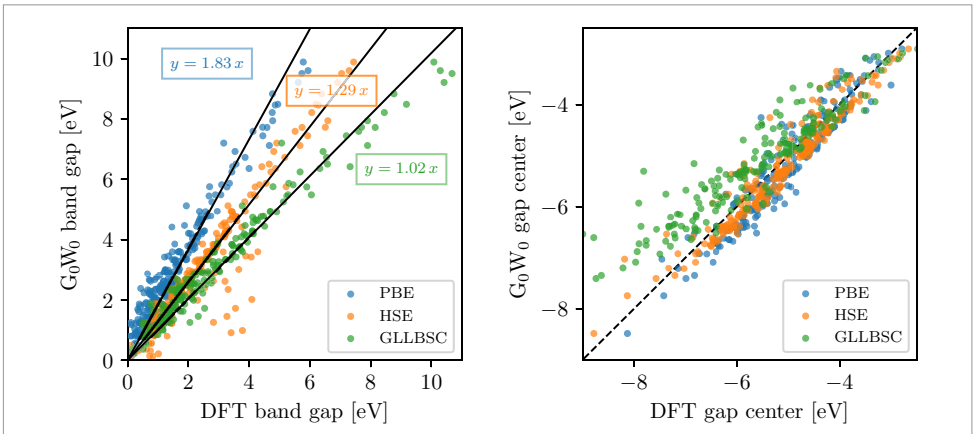

Figure 20. Band gaps (left) and gap centers (right) obtained with different DFT functionals plotted against the G_0W_0 results. The band gaps of PBE (blue), HSE06 (orange), and GLLBSC (green) are fitted linearly to G_0W_0. For the gap centers the bisector is shown.

Table 10. The mean absolute deviation (in eV) of the band gap and band gap center calculated with three different xc-functionals with respect to G_0W_0.

	PBE	HSE06	GLLBSC
MAD w.r.t. G_0W_0 (band gap)	1.49	0.82	0.38
MAD w.r.t. G_0W_0 (gap center)	0.37	0.32	0.76

If one assumes energetically isolated and parabolic bands, the intrinsic mobility limited only by scattering on acoustic phonons can be estimated from the Takagi formula [147],

$$\mu_i = \frac{e\hbar^3 \rho v_i^2}{k_B T m_i^* m_d^* D_i^2}. \quad (17)$$

Here i refers to the transport direction, ρ is the mass density, v_i is the speed of sound in the material, m_i^* is the carrier mass, m_d^* is the equivalent isotropic density-of-state mass defined as $m_d^* = \sqrt{m_x^* m_y^*}$, and D_i is the deformation potential. We stress that the simple Takagi formula is only valid for temperatures high enough that the acoustic phonon population can be approximated by the Rayleigh–Jeans law, $n \approx \hbar\omega_{ac}/k_B T$, but low enough that scattering on optical phonons can be neglected.

For the semiconductors in the C2DB we have found that the denominator of equation (17) varies more than the numerator. Consequently, a small product of deformation potential and effective mass is expected to correlate with high mobility. Figure 23 shows the deformation potential plotted against the carrier mass for the valence and conduction bands, respectively. The shaded area corresponds, somewhat arbitrarily, to the region for which $m_i^* D_i < m_0(1\text{ eV})$. The 2D semiconductors which have been synthesised in monolayer form are indicated with orange symbols while those which have been used in field effect transistors are labeled. Consistent with experimental findings, phosphorene (P) is predicted to be among the materials with the highest mobility for both electrons and holes.

Interestingly, a number of previously unknown 2D materials lie in this shaded region and could be candidates for high mobility 2D semiconductors. Table 11 lists a few selected materials with high intrinsic mobility according to equation (17), which all have 'high' overall stability (see section 2.4.1). In the future, it will be interesting to explore the transport properties of these candidate materials in greater detail.

To put the numbers in table 11 to scale, we consider the well studied example of MoS_2. For this material we obtain an electron mobility of 240 $cm^2\,V^{-1}\,s^{-1}$ while a full *ab initio* calculation found a phonon-limited mobility of 400 $cm^2\,V^{-1}\,s^{-1}$ (in good agreement with experiments on hBN encapsulated MoS_2 [148]), with the acoustic phonon contribution corresponding to a mobility of 1000 $cm^2\,V^{-1}\,s^{-1}$. Similarly, for the series MX_2 (M = W, Mo, X = S, Se), we calculate room-temperature electron mobilities between 200 $cm^2\,V^{-1}\,s^{-1}$ and 400 $cm^2\,V^{-1}\,s^{-1}$, which are all within 50% of the *ab initio* results [149]. Presumably, as in the case for MoS_2, the good quantitative agreement is partly a result of error cancellation between an overestimated acoustic phonon scattering and the neglect of optical phonon scattering. Importantly, however, the relative ordering of the mobilities of the four MX_2 monolayers is correctly predicted by equation (17) for all but one pair (MoS_2 and WSe_2) out of the six pairs. These results illustrate that equation (17) should only be used for 'order of magnitude' estimates of the mobility but that relative comparisons of mobilities in different materials are probably reliable.

3.2.3. *Magnetic properties*

Recently, a single layer of CrI_3 was reported to exhibit ferromagnetic order with a Curie temperature of 45 K [12]. This comprises the first example of a pure 2D material exhibiting magnetic order and there is

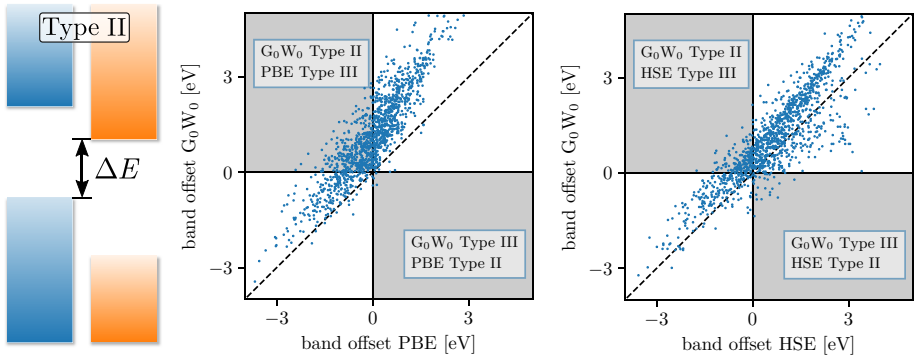

Figure 21. Band alignment at heterobilayers, assuming that the bands line up with a common vacuum level. The left panel shows the definition of the band offset ΔE. The middle and right panels show randomly selected bilayer combinations with Type II ($\Delta E > 0$) or Type III ($\Delta E < 0$) band alignment. The black line indicates the bisector, the grey areas indicate qualitatively wrong DFT band alignments compared to G_0W_0.

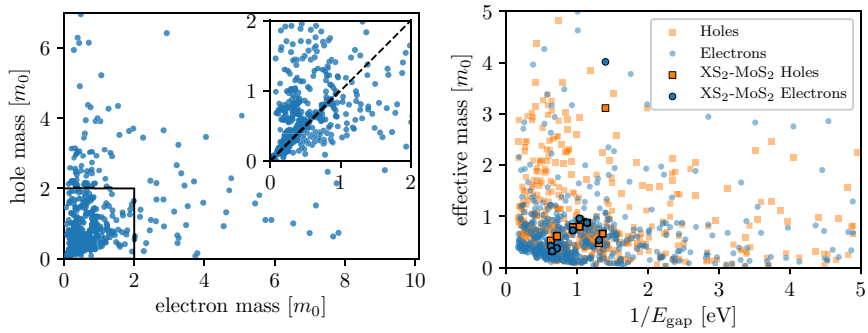

Figure 22. (left) Effective electron mass versus hole mass. On average holes are slightly heavier than electrons. (right) Effective carrier mass versus the inverse band gap. The linear correlation between the two quantities, expected from $\mathbf{k} \cdot \mathbf{p}$ perturbation theory, is seen not to hold in general. Materials with the formula XS_2 in the MoS_2 crystal structure are highlighted.

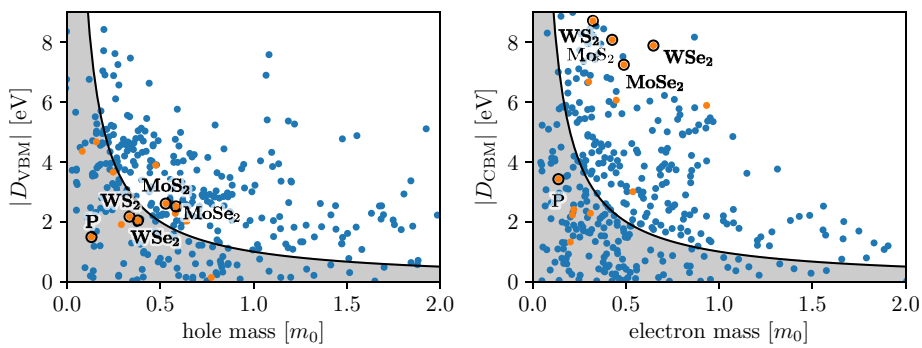

Figure 23. The deformation potential of the materials plotted against the carrier effective masses for the valence band (left) and the conduction band (right). The shaded region in each panel indicates a region of interest in the search for high-mobility semiconductors. The 2D materials which have previously been synthesised in monolayer form are highlighted in orange and selected structures for which mobilities have been measured are labelled.

Table 11. Key transport properties of selected materials with high intrinsic room-temperature mobility according to equation (17). All the materials shown have 'high' overall stability as defined in section 2.4.1. μ_{high} is the larger value of the mobilities in the x or y directions, m^* is the corresponding effective mass, and μ_{high}/μ_{low} is the ratio of the mobilities in the two directions.

Carrier	Formula	Prototype	PBE gap (eV)	μ_{high} ($cm^2\,V^{-1}\,s^{-1}$)	m^* (m_0)	$\frac{\mu_{high}}{\mu_{low}}$
Holes	PbS_2	MoS_2	1.39	30 000	0.62	1.4
	OsO_2	WTe_2	0.17	23 000	0.23	3.0
	$ZrCl_2$	MoS_2	0.98	12 000	0.43	1.1
	WSSe	MoSSe	1.40	5500	0.37	1.0
Electrons	$PtTe_2$	CdI_2	0.30	9600	0.17	1.3
	GaO	GaS	1.56	7200	0.32	1.0
	NiS_2	CdI_2	0.58	6000	0.29	1.5
	$RuTe_2$	WTe_2	0.64	4600	1.55	8.5

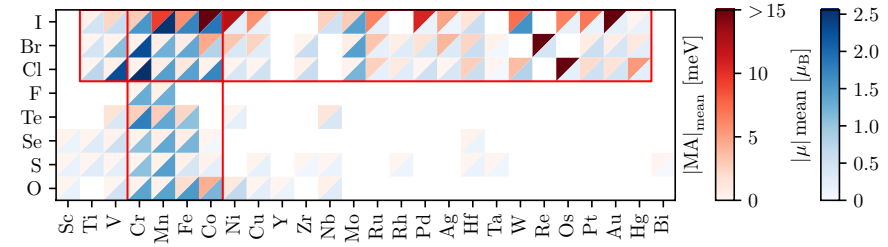

Figure 24. Absolute magnetic anisotropy (red) and magnetic moment (blue) averaged over all materials in the C2DB with a given composition. The two red boxes highlight the halides and 3*d* metals, respectively.

currently an intense search for new 2D materials with magnetic order persisting above room temperature [150–152].

For 2D materials, magnetic order will only persist at finite temperatures in the presence of magnetic anisotropy (MA). Indeed, by virtue of the Mermin–Wagner theorem, magnetic order is impossible in 2D unless the rotational symmetry of the spins is broken [153]. A finite MA with an out of plane easy axis breaks the assumption behind the Mermin–Wagner theorem and makes magnetic order possible at finite temperature. The critical temperature for magnetic order in 2D materials will thus have a strong dependence on the anisotropy.

The MA originates from spin–orbit coupling and is here defined as the energy difference between in-plane and out-of-plane orientation of the magnetic moments, see equation (4). With our definition, a negative MA corresponds to an out-of-plane easy axis. We note that most of the materials in the C2DB are nearly isotropic in-plane. Consequently, if the easy axis lies in the plane, the spins will exhibit an approximate in-plane rotational symmetry, which prohibits magnetic order at finite temperatures. Since spin–orbit coupling becomes large for heavy elements, we generally expect to find larger MA for materials containing heavier elements. In general the magnitude of the MA is small. For example, for a monolayer of CrI_3 with a Curie temperature of 45 K [12] we find a MA of –0.85 meV per Cr atom in agreement with previous calculations [154]. Although small, the MA is, however, crucial for magnetic order to emerge at finite temperature.

In figure 24 we show the magnitude of the magnetic anisotropy (red triangles) and the magnetic moment per metal atom (blue triangles) averaged over all materials with a given chemical composition. The plot is based on data for around 1200 materials in the medium to high stability categories (see table 2) out of which around 350 are magnetic. It is interesting to note that while the magnetic moment is mainly determined by the metal atom, the MA depends strongly on the non-metal atom. For example, the halides (Cl, Br, I) generally exhibit much larger MAs than the chalcogenides (S, Se, Te). Overall, iodine (I) stands out as the most significant element for a large MA while the 3*d* metals Cr, Mn, Fe, Co are the most important elements for a large magnetic moment. Since the MA is driven by spin–orbit coupling (SOC) and the spin is mainly located on the metal atom, one would expect a large MA to correlate with a heavy metal atom. However, it is clear from the figure that it is not essential that the spin-carrying metal atom should also host the large SOC. For example, we find large MA for several 3*d* metal-iodides despite of the relatively weak SOC on the 3*d* metals. This shows that the MA is governed by a rather complex interplay between the spins, orbital hybridisation and crystal field.

A selection of materials predicted to have high overall stability (see section 2.4.1) and high out-of-plane magnetic anisotropy (MA < -0.3 meV/

Table 12. Selection of magnetic materials with a negative MA per magnetic atom. The prototype, the magnetic moment of the magnetic atom, the energy gap calculated with PBE xc-functional and the magnetic state are also shown. The experimentally synthesised ferromagnetic monolayer CrI_3 is highlighted.

Formula	Prototype	Magnetic moment (μ_B)	PBE gap (eV)	MA (meV/atom)	Magnetic state	ΔH_{hull} (eV/atom)
OsI_3	BiI_3	0.9	0.0	−3.17	FM	0.18
CrTe	FeSe	2.6	0.0	−1.85	AFM	0.15
$FeCl_3$	BiI_3	1.0	0.01	−1.84	FM	−0.08
FeTe	FeSe	1.9	0.0	−1.06	FM	0.08
$MnTe_2$	CdI_2	2.7	0.0	−0.94	FM	−0.10
$FeBr_3$	BiI_3	1.0	0.04	−0.88	FM	−0.04
CrI_3	**BiI_3**	**3.0**	**0.90**	**−0.85**	**FM**	**−0.21**
MnTe	FeSe	3.8	0.69	−0.75	AFM	−0.15
NiO	PbSe	1.1	0.0	−0.53	FM	0.05
FeBrO	FeOCl	1.1	0.0	−0.47	FM	−0.05
CrISe	FeOCl	3.0	0.0	−0.45	FM	−0.10
$MnSe_2$	CdI_2	2.8	0.0	−0.40	FM	−0.18
CrIS	FeOCl	3.0	0.35	−0.36	FM	−0.10
MnO_2	CdI_2	3.0	1.13	−0.36	FM	0.02
VCl_3	BiI_3	2.0	0.0	−0.35	FM	−0.01
MnSe	FeSe	3.7	0.90	−0.31	AFM	−0.20
CrSe	FeSe	2.0	0.0	−0.31	AFM	0.12

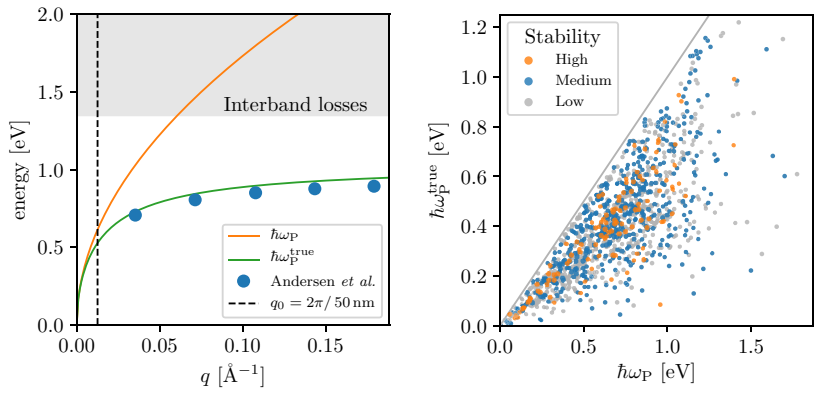

Figure 25. (left) Plasmon dispersion relations for the unscreened (i.e. intraband) and true plasmons, $\hbar\omega_P$ and $\hbar\omega_P^{true}$, respectively, for NbS_2 in the H phase (the MoS_2 crystal structure prototype). This is compared to the full first principles calculations of the plasmons in NbS_2 by Andersen *et al* (data points) [159]. (right) The in-plane averaged true plasmon frequency versus the unscreened plasmon frequency for all metals in C2DB at a plasmon wavelength of $\lambda_P = 50$ nm corresponding to q_0 in the left panel. The data points are colored by the overall stability level as defined in section 2.4.1, and the straight line corresponds to $\hbar\omega_P = \hbar\omega_P^{true}$.

magnetic atom) is listed in table 12. We find several semiconductors with anisotropies comparable to CrI3 and some metals with higher values. If we also look at materials with medium overall stability, we find semiconductors with anisotropies up to 2 meV/atom. It is likely that some of these materials will have Curie temperatures similar to, or even higher than, CrI_3.

In addition to the MA, the critical temperature depends sensitively on the magnetic exchange couplings. We are presently developing a workflow for systematic calculation of exchange coupling constants, which will allow us to estimate the Curie temperature of all the magnetically ordered 2D materials. The database contains several 2D materials with antiferromagnetic order. As a note of caution, we mention that the magnetic interactions in AFM materials typically arise from the super-exchange mechanism, which is poorly described by PBE and requires a careful verification using a PBE + U scheme [155].

3.2.4. *Plasmons*

The unique optical properties of 2D materials make them highly interesting as building blocks for nanophotonic applications [156, 157]. Many of these applications involve electron rich components which can capture, focus, and manipulate light via plasmons or plasmon-polaritons. Graphene sheets can host plasmons that are long lived, can be easily tuned via electrostatic or chemical doping, and can be used to confine light to extremely small volumes [158].

Table 13. Selection of 2D metals with high plasmon energies ω_P^{true} for a plasmon wavelength of $\lambda_P = 50$ nm. The interband screening $\alpha^{2D,inter}$ at $\omega = 0$ and the in-plane averaged 2D plasma frequency $\omega_{P,2D}$, which are required to reproduce ω_P^{true}, are also reported.

Prototype	Formula	Magnetic state	ω_P^{true} (eV)	$\alpha^{2D,inter}$ (Å)	$\omega_{P,2D}$ (eV Å$^{0.5}$)
TiS_3	$TaSe_3$	NM	0.99	12.54	12.48
FeOCl	PdClS	NM	0.93	4.13	9.52
FeOCl	NiClS	NM	0.90	5.60	9.66
CdI_2	TaS_2	NM	0.82	5.59	8.79
FeOCl	ZrIS	NM	0.75	7.68	8.43
CdI_2	NbS_2	NM	0.73	8.2	8.42
FeOCl	ZrClS	NM	0.73	13.6	9.35
TiS_3	TaS_3	NM	0.73	34.22	12.44
PbSe	NiO	FM	0.72	2.9	7.16

However, due to the limited charge carrier density achievable in graphene, its plasmons are limited to the mid-infrared regime. Here we show that some metallic monolayers support plasmons with significantly higher energies than graphene and could potentially push 2D plasmonics into the optical regime.

Figure 25 (left) shows the plasmon dispersion for monolayer NbS_2 in the MoS_2 crystal structure. The effect of interband transitions on the plasmon is significant as can be seen by comparison to the pure intraband plasmon ($\hbar\omega_P$). The true plasmon energies are obtained from the poles of the (long wave length limit) dielectric function including the interband transitions, $\epsilon = 1 + 2\pi q(\alpha^{2D,intra} + \alpha^{2D,inter})$, yielding $\omega_P^{true} = \omega_{P,2D} q^{1/2}[1 + 2\pi q \alpha^{2D,inter}(\omega_P^{true})]^{-1/2}$. For simplicity we ignore the frequency dependence of the interband polarisability, i.e. we set $\alpha^{2D,inter}(\omega_P^{true}) \approx \alpha^{2D,inter}(\omega = 0)$, which should be valid for small plasmon energies (far from the onset of interband transitions). The validity of this approximation is confirmed by comparing to the full *ab initio* calculations of Andersen *et al* (blue dots) which include the full q- and ω-dependence [159]. The figure shows that interband screening generally reduces the plasmon energy and becomes increasingly important for larger q.

Figure 25 (right) shows the in-plane averaged true plasmon energy of all metals in the C2DB plotted against the intraband plasmon energy at a fixed plasmon wavelength of $\lambda_P = 50$ nm (corresponding to q_0 at the dashed vertical line in the left panel). For comparison, the plasmon energy of freestanding graphene at this wavelength and for the highest achievable doping level ($E_F = \pm 0.5$ eV relative to the Dirac point) is around 0.4 eV. The data points are colored according to the overall stability level as defined in section 2.4.1. Table 13 shows a selection of the 2D metals with 'high' overall stability (see section 2.4.1) and large plasmon frequencies. We briefly note the interesting band structures of the metals in the FeOCl prototype (not shown) which exhibits band gaps above or below the partially occupied metallic band(s), which is likely to lead to reduced losses in plasmonic applications [160]. A detailed study of the plasmonic properties of the lead candidate materials will be published elsewhere. However, from figure 25 (right) it is already clear that several of the 2D metals have plasmon energies around 1 eV at $\lambda_P = 50$ nm, which significantly exceeds the plasmon energies in highly doped graphene.

3.2.5. Excitons

Two-dimensional materials generally exhibit pronounced many-body effects due to weak screening and strong quantum confinement. In particular, exciton binding energies in monolayers are typically an order of magnitude larger than in the corresponding layered bulk phase and it is absolutely crucial to include excitonic effects in order to reproduce experimental absorption spectra.

The electronic screening is characterised by the in-plane 2D polarisability, see equation (12). For a strictly 2D insulator, the screened Coulomb potential can be written as $W^{2D}(q) = v_c^{2D}(q)/\epsilon^{2D}(q)$ with $\epsilon^{2D}(q) = 1 + 2\pi\alpha^{2D}q$ and $v_c^{2D}(q) = 2\pi/q$ is the 2D Fourier transform of the Coulomb interaction. The q-dependence of ϵ^{2D} indicates that the screening is non-local, i.e. it cannot be represented by a q-independent dielectric constant, and that Coulomb interactions tend to be weakly screened at large distances (small q vectors) [119, 161, 162]. This is in sharp contrast to the case of 3D semiconductors/insulators where screening is most effective at large distances where its effect can be accounted for by a q-independent dielectric constant. For a two-band model with isotropic parabolic bands, the excitons can be modeled by a 2D Hydrogen-like (Mott–Wannier) Hamiltonian where the Coulomb interaction is replaced by $W = 1/\epsilon r$ and the electron mass is replaced by a reduced excitonic mass μ_{ex} derived from the curvature of conduction and valence bands. It has previously been shown that the excitonic Rydberg series of a 2D semiconductor can be accurately reproduced by this model if the dielectric constant, ϵ, is obtained by averaging $\epsilon^{2D}(q)$ over the extent of the exciton in reciprocal space [163]. For the lowest exciton ($n = 1$), the binding energy can then be expressed as

$$E_B = \frac{8\mu_{ex}}{(1 + \sqrt{1 + 32\pi\alpha^{2D}\mu_{ex}/3})^2}. \qquad (18)$$

It has furthermore been demonstrated that this expression gives excellent agreement with a numerical solution of the Mott–Wannier model employing the full q-dependent dielectric function, $\epsilon^{2D}(q) = 1 + 2\pi\alpha^{2D}q$, for 51 transition metal dichalcogenides [163]. We note that the previous calculations were based on LDA and we generally find that the PBE values for α^{2D} obtained in the present work are 10–20% smaller compared with LDA.

In figure 26, we compare the binding energy of the lowest exciton obtained from BSE-PBE with G_0W_0 scissors operator and the Mott–Wannier model equation (18), respectively. Results are shown for the 194

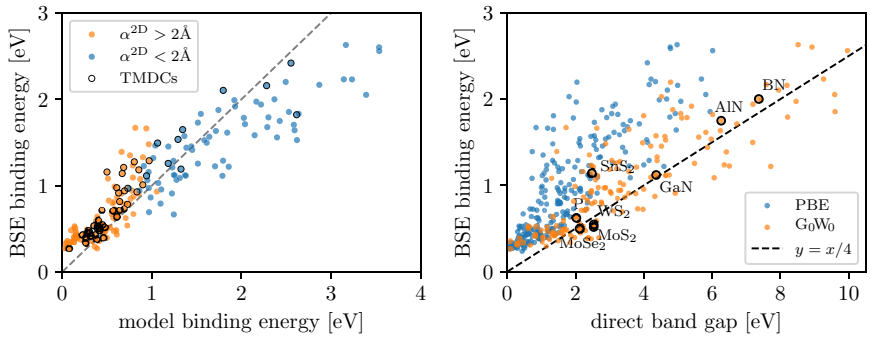

Figure 26. (left) Binding energy of the lowest exciton in 194 semiconducting monolayers calculated from the Bethe–Salpeter equation (BSE) and the screened 2D Mott–Wannier model equation (18). The colors of the symbols indicate if screening in the material is weak ($\alpha^{2D} < 2$Å). The transition metal dichalcogenides (TMDCs) are highlighted with black circles. (right) The exciton binding energy as a function of the direct band gap, with selected materials labelled.

non-magnetic semiconductors out of the total set of ~ 250 materials for which BSE calculations have been performed. We focus on the optically active zero-momentum excitons and compute the exciton masses by evaluating the curvature of the band energies at the *direct gap*, see section 2.11. For anisotropic materials we average the heavy and light exciton masses as well as the x and y components of the polarisability, α^{2D}, to generate input parameters for the isotropic model equation (18).

Although a clear correlation with the BSE results is observed, it is also evident that the Mott–Wannier model can produce significant errors. The mean absolute deviation between BSE and the model is 0.28 eV for all materials and 0.20 eV for the subset of transition metal dichalcogenides (TMDCs). Furthermore, the Mott–Wannier model seems to overestimate E_B for more strongly bound excitons while the opposite trend is seen for weakly bound excitons. As explained below these trends are a consequence of systematic errors in the Mott–Wannier model which can be traced to two distinct sources.

(i) *Weak screening*: If α^{2D} is small (on the order of 1 Å), the exciton becomes strongly localised and the orbital character of the states comprising the exciton plays a significant role. In general, the Mott–Wannier model tends to overestimate the exciton binding energy in this case as can be seen from the relatively large deviation of points with model binding energies >2.0 eV in figure 26. The overestimated binding energy results from the homogeneous electron and hole distributions implicitly assumed in the Mott–Wannier model. In reality, the short range variation of the electron and hole distributions is determined by the shape of the conduction and valence band states. In general these will differ leading to a reduced spatial overlap of the electron and hole and thus a lower Coulomb interaction. For example, $SrCl_2$ in the CdI_2 prototype ($\alpha^{2D} = 0.68$ Å) has a BSE binding energy of 2.1 eV and a model binding energy of 3.4 eV. From the PDOS of this material (see the C2DB webpage) it is evident that the electron and hole are mainly residing on the Sr and Cl atoms, respectively.

(ii) *Breakdown of the parabolic band approximation*: Materials with small band gaps often exhibit hyperbolic rather than parabolic band structures in the vicinity of the band gap. This typically happens in materials with small band gaps such as BSb in the BN prototype. In figure 26 these materials can be identified as the cluster of points with model binding energies <0.25 eV and BSE binding energies >0.25 eV. A similar situation occurs if the conduction and valence bands flatten out away from the band gap region. In both of these cases, the excitons tend to be delocalised over a larger area in the Brillouin zone than predicted by the parabolic band approximation of the Mott–Wannier model. Typically, such delocalisation will result in larger binding energies than predicted by the model. For example, FeI_2 in the CdI_2 prototype exhibits shallow band minima in a ring around the Γ-point and has a BSE binding energy of 1.1 eV and a model binding energy of 0.5 eV because the model assumes that the exciton will be located in the vicinity of the shallow minimum (and thus more delocalised in real space). A detailed inspection reveals that such break down of the parabolic band approximation is responsible for most of the cases where the model underestimates the binding energy.

Other sources of errors come from contributions to the exciton from higher/lower lying bands, i.e. break down of the two-band approximation, and anisotropic exciton masses not explicitly accounted for by equation (18).

Based on this comprehensive and unbiased assessment of the Mott–Wannier model, we conclude that while the model can be useful for understand-

ing trends and qualitative properties of excitons, its quantitative accuracy is rather limited when applied to a broad set of materials without any parameter tuning. For quantitative estimates α^{2D} should not be too small (certainly not less than 2 Å) and the the validity of the effective mass approximation should be carefully checked by inspection of the band structure.

It has been argued that there should exist a robust and universal scaling between the exciton binding energy and the quasiparticle band gap of 2D semiconductors, namely $E_B \approx E_{gap}/4$ [164]. This scaling relation was deduced empirically based on BSE-GW calculations for around 20 monolayers and explained from equation (18) and the relation $\alpha^{2D} \propto 1/E_{gap}$ from $\mathbf{k}\cdot\mathbf{p}$ perturbation theory. Another work observed a similar trend [165] but explained it from the $1/E_{gap}$ dependence of the exciton effective mass expected from $\mathbf{k}\cdot\mathbf{p}$ perturbation theory. Based on our results we can completely refute the latter explanation (see figure 22 (right)). In figure 26 (right) we show the exciton binding energy plotted versus the direct PBE and G_0W_0 band gaps, respectively. While there is a correlation, it is by no means as clear as found in [164].

4. Conclusions and outlook

The C2DB is an open database with calculated properties of two-dimensional materials. It currently contains more than 1500 materials distributed over 32 different crystal structures. A variety of structural, elastic, thermodynamic, electronic, magnetic and optical properties are computed following a high-throughput, semi-automated workflow employing state of the art DFT and many-body methods. The C2DB is growing continuously as new structures and properties are being added; thus the present paper provides a snapshot of the present state of the database. The C2DB can be browsed online using simple and advanced queries, and it can be downloaded freely at https://c2db.fysik.dtu.dk/ under a Creative Commons license.

The materials in the C2DB comprise both experimentally known and not previously synthesised structures. They have been generated in a systematic fashion by combinatorial decoration of different 2D crystal lattices. The full property workflow is performed only for structures that are found to be dynamically stable and have a negative heat of formation. We employ a liberal stability criterion in order not to exclude potentially interesting materials that could be stabilised by external means like substrate interactions or doping even if they are unstable in freestanding form. As an important and rather unique feature, the C2DB employs beyond-DFT methods, such as the many-body GW approximation, the random phase approximation (RPA) and the Bethe–Salpeter equation (BSE). Such methods are essential for obtaining quantitatively accurate descriptions of key properties like band gaps and optical spectra. This is particularly important for 2D materials due the weak dielectric screening in reduced dimensions, which tends to enhance many-body effects. For maximal transparency and reproducibility of the data in the C2DB, all relevant parameters have been provided in this paper. Additionally, all scripts used to generate the data are freely available for download under a GPL license.

Beyond its obvious use as a look-up table, the C2DB offers access to numerous well documented, high-quality calculations, making it ideally suited for benchmarking and comparison of different codes and methodologies. The large set of different available properties makes the C2DB interesting as a playground for exploring structure-property relations and for applying and advancing machine learning approaches in materials science. Moreover, the C2DB should be useful as a stepping stone towards the development of theoretical models for more complex 2D structures such as van der Waals heterostructures (see below).

As reported in this work, based on the combinatorial screening approach, we have identified a number of new, potentially synthesisable 2D materials with interesting properties including ferromagnets with large magnetic anisotropy, semiconductors with high intrinsic carrier mobility, and metals with plasmons in the visible frequency range. These predictions are all based on the computed properties of the perfect crystalline materials. While the pristine crystal constitutes an important baseline reference it remains an idealised model of any real material. In the future, it would be interesting to extend the database to monolayers with adsorbed species and/or point defects. Not only would this allow for a more realistic assessment of the magnetic and (opto)electronic properties, it would also facilitate the design and discovery of 2D materials for e.g. battery electrodes and (electro)catalysis [166, 167].

The C2DB should also be useful as a platform for establishing parametrisations of computationally less expensive methods such as tight-binding models [168] and $\mathbf{k}\cdot\mathbf{p}$ perturbation theory [128]. Such methods are required e.g. for device modeling, description of magnetic field effects, and van der Waals heterostructures. The database already provides band structures, spin orbit-induced band splittings, and effective masses, which can be directly used to determine model parameters. It would be straightforward to complement these with momentum matrix elements at band extrema for modeling of optical properties and construction of full $\mathbf{k}\cdot\mathbf{p}$ Hamiltonians. Similarly, the spread functional required as input for the construction of Wannier functions e.g. by the ASE [38] or the Wannier90 [169] packages, could be easily and systematically produced. This would enable direct construction of minimal basis set Hamiltonians and would allow for the calculation of Born charges and piezoelectric coefficients as well as certain topological invariants [170]. A workflow to calculate exchange couplings of magnetic 2D materials is currently being developed with the aim of predicting magnetic phase transitions and critical temperatures.

Of specific interest is the modeling of the electronic and optical properties of vdW heterostructures. Due to lattice mismatch or rotational misalignment between stacked 2D layers, such structures are difficult or even impossible to treat by conventional *ab initio* techniques. Different simplified models have been proposed to describe the electronic bands, including tight-binding Hamiltonians derived from strained lattice configurations [171] and perturbative treatments of the interlayer coupling [172]. In both cases, the data in the C2DB represents a good starting point for constructing such models. The effect of dielectric screening in vdW heterostructures can be incorporated e.g. by the quantum electrostatic heterostructure (QEH) model [173] which computes the dielectric function of the vdW heterostructure from the polarisabilities of the isolated monolayers. The latter are directly available in the C2DB, at least in the long wavelength limit.

Finally, it would be relevant to supplement the current optical absorbance spectra by other types of spectra, such as Raman spectra, infrared absorption or XPS, in order to assist experimentalists in characterising their synthesised samples. The automatic first-principles calculation of such spectra is, however, not straightforward and will require significant computational investments.

Acknowledgments

The Center for Nanostructured Graphene is sponsored by the Danish National Research Foundation, Project DNRF103. The project also received funding from the European Unions Horizon 2020 research and innovation programme under Grant Agreement No. 676580 with The Novel Materials Discovery (NOMAD) Laboratory, a European Center of Excellence. This work was also supported by a research grant (9455) from VILLUM FONDEN. This project has received funding from the European Research Council (ERC) under the European Union's Horizon 2020 research and innovation programme (grant agreement No 773122, LIMA).

ORCID iDs

Sten Haastrup https://orcid.org/0000-0003-3696-0356
Mohnish Pandey https://orcid.org/0000-0002-1715-0617
Thorsten Deilmann https://orcid.org/0000-0003-4165-2446
Nicki F Hinsche https://orcid.org/0000-0002-0176-6038
Morten N Gjerding https://orcid.org/0000-0002-5256-660X
Kristian S Thygesen https://orcid.org/0000-0001-5197-214X

References

[1] Ferrari A C *et al* 2015 Science and technology roadmap for graphene, related two-dimensional crystals and hybrid systems *Nanoscale* **7** 4598–810
[2] Bhimanapati G R *et al* 2015 Recent advances in two-dimensional materials beyond graphene *Acs Nano* **9** 11509–39
[3] Huang C, Wu S, Sanchez A M, Peters J J, Beanland R, Ross J S, Rivera P, Yao W, Cobden D H and Xu X 2014 Lateral heterojunctions within monolayer mose2–wse2 semiconductors *Nat. Mater.* **13** 1096–101
[4] Geim A K and Grigorieva I V 2013 Van der waals heterostructures *Nature* **499** 419–25
[5] Molle A, Goldberger J, Houssa M, Xu Y, Zhang S-C and Akinwande D 2017 Buckled two-dimensional xene sheets *Nat. Mater.* **16** 163–9
[6] Bianco E, Butler S, Jiang S, Restrepo O D, Windl W and Goldberger J E 2013 Stability and exfoliation of germanane: a germanium graphane analogue *Acs Nano* **7** 4414–21
[7] Wang Q H, Kalantar-Zadeh K, Kis A, Coleman J N and Strano M S 2012 Electronics and optoelectronics of two-dimensional transition metal dichalcogenides *Nat. Nanotechnol.* **7** 699–712
[8] Naguib M, Mashtalir O, Carle J, Presser V, Lu J, Hultman L, Gogotsi Y and Barsoum M W 2012 Two-dimensional transition metal carbides *ACS Nano* **6** 1322–31
[9] Ci L *et al* 2010 Atomic layers of hybridized boron nitride and graphene domains *Nat. Mater.* **9** 430–5
[10] Al Balushi Z Y *et al* 2016 Two-dimensional gallium nitride realized via graphene encapsulation *Nat. Mater.* **15** 1166
[11] Lin S-H and Kuo J-L 2014 Towards the ionic limit of two-dimensional materials: monolayer alkaline earth and transition metal halides *Phys. Chem. Chem. Phys.* **16** 20763–71
[12] Huang B *et al* 2017 Layer-dependent ferromagnetism in a van der Waals crystal down to the monolayer limit *Nature* **546** 270
[13] Dattatray J *et al* 2012 Gas and gase ultrathin layer transistors *Adv. Mater.* **24** 3549–54
[14] Hu P, Wen Z, Wang L, Tan P and Xiao K 2012 Synthesis of few-layer gase nanosheets for high performance photodetectors *Acs Nano* **6** 5988–94
[15] Dou L *et al* 2015 Atomically thin two-dimensional organic-inorganic hybrid perovskites *Science* **349** 1518–21
[16] Ashton M, Paul J, Sinnott S B and Hennig R G 2017 Topology-scaling identification of layered solids and stable exfoliated 2d materials *Phys. Rev. Lett.* **118** 106101
[17] Cheon G, Duerloo K-A N, Sendek A D, Porter C, Chen Y and Reed E J 2017 Data mining for new two-and one-dimensional weakly bonded solids and lattice-commensurate heterostructures *Nano Lett.* **17** 1915–23
[18] Mounet N, Gibertini M, Schwaller P, Merkys A, Castelli I E, Cepellotti A, Pizzi G and Marzari N 2018 Novel two-dimensional materials from high-throughput computational exfoliation of experimentally known compounds *Nat. Nanotechnol.* **13** 246–52
[19] Choudhary K, Kalish I, Beams R and Tavazza F 2017 High-throughput identification and characterization of two-dimensional materials using density functional theory *Sci. Rep.* **7** 5179
[20] Jain A, Persson K A and Ceder G 2016 Research update: the materials genome initiative: data sharing and the impact of collaborative *ab initio* databases *APL Mater.* **4** 053102
[21] Thygesen K S and Jacobsen K W 2016 Making the most of materials computations *Science* **354** 180–1
[22] Jain A, Ong S P, Hautier G, Chen W, Richards W D, Dacek S, Cholia S, Gunter D, Skinner D, Ceder G and Persson K A 2013 The materials project: a materials genome approach to accelerating materials innovation *APL Mater.* **1** 011002
[23] Curtarolo S *et al* 2012 Aflow: an automatic framework for high-throughput materials discovery *Comput. Mater. Sci.* **58** 218–26
[24] Saal J E, Kirklin S, Aykol M, Meredig B and Wolverton C 2013 Materials design and discovery with high-throughput density

functional theory: the open quantum materials database (oqmd) *JOM* **65** 1501–9
[25] Kirklin S, Saal J E, Meredig B, Thompson A, Doak J W, Aykol M, Ruehl S and Wolverton C 2015 The open quantum materials database (oqmd): assessing the accuracy of dft formation energies *NPJ Comput. Mater.* **1** 15010
[26] http://nomad-repository.eu; https://nomad-coe.eu
[27] Lejaeghere K *et al* 2016 Reproducibility in density functional theory calculations of solids *Science* **351** aad3000
[28] Hautier G, Fischer C C, Jain A, Mueller T and Ceder G 2010 Finding nature's missing ternary oxide compounds using machine learning and density functional theory *Chem. Mater.* **22** 3762–7
[29] Ghiringhelli L M, Vybiral J, Levchenko S V, Draxl C and Scheffler M 2015 Big data of materials science: critical role of the descriptor *Phys. Rev. Lett.* **114** 105503
[30] Ward L and Wolverton C 2017 Atomistic calculations and materials informatics: a review *Curr. Opin. Solid State Mater. Sci.* **21** 167–76
[31] Şahin H, Cahangirov S, Topsakal M, Bekaroglu E, Akturk E, Senger R T and Ciraci S 2009 Monolayer honeycomb structures of group-IV elements and III–V binary compounds: first-principles calculations *Phys. Rev.* B **80** 155453
[32] Ciraci S and Cahangirov S 2017 *2D Materials: Properties and Devices* ed P Avouris *et al* (Cambridge: Cambridge University Press) pp 472–84
[33] Ataca C, Sahin H and Ciraci S 2012 Stable, single-layer mx2 transition-metal oxides and dichalcogenides in a honeycomb-like structure *J. Phys. Chem.* C **116** 8983–99
[34] Lebègue S, Björkman T, Klintenberg M, Nieminen R M and Eriksson O 2013 Two-dimensional materials from data filtering and *ab initio* calculations *Phys. Rev.* X **3** 031002
[35] Miro P, Audiffred M and Heine T 2014 An atlas of two-dimensional materials *Chem. Soc. Rev.* **43** 6537–54
[36] Rasmussen F A and Thygesen K S 2015 Computational 2d materials database: electronic structure of transition-metal dichalcogenides and oxides *J. Phys. Chem.* C **119** 13169–83
[37] Enkovaara J E *et al* 2010 Electronic structure calculations with gpaw: a real-space implementation of the projector augmented-wave method *J. Phys.: Condens. Matter* **22** 253202
[38] Larsen A *et al* 2017 The atomic simulation environment—a python library for working with atoms *J. Phys.: Condens. Matter* **29** 273002
[39] Cordero B, Gomez V, Platero-Prats A E, Reves M, Echeverria J, Cremades E, Barragan F and Alvarez S 2008 Covalent radii revisited *Dalton Trans.* **37** 2832–8
[40] Larsen P M 2017 Structural analysis algorithms for nanomaterials *PhD Thesis* Department of Physics, DTU
[41] Özçelik V O, Azadani J G, Yang C, Koester S J and Low T 2016 Band alignment of two-dimensional semiconductors for designing heterostructures with momentum space matching *Phys. Rev.* B **94** 035125
[42] Togo A 2009 Spglib https://atztogo.github.io/spglib/
[43] Pandey M and Jacobsen K W 2015 Heats of formation of solids with error estimation: the mbeef functional with and without fitted reference energies *Phys. Rev.* B **91** 235201
[44] Stevanović V, Lany S, Zhang X and Zunger A 2012 Correcting density functional theory for accurate predictions of compound enthalpies of formation: fitted elemental-phase reference energies *Phys. Rev.* B **85** 115104
[45] Anisimov V and Gunnarsson O 1991 Density-functional calculation of effective coulomb interactions in metals *Phys. Rev.* B **43** 7570
[46] Kuhar K, Crovetto A, Pandey M, Thygesen K S, Seger B, Vesborg P C K, Hansen O, Chorkendorff I and Jacobsen K W 2017 Sulfide perovskites for solar energy conversion applications: computational screening and synthesis of the selected compound lays3 *Energy Environ. Sci.* **10** 2579–93
[47] Zhou Y *et al* 2018 Antiferromagnetic order in epitaxial fese films on srtio 3 *Phys. Rev. Lett.* **120** 097001
[48] Alfe D 2009 Phon: a program to calculate phonons using the small displacement method *Comput. Phys. Commun.* **180** 2622–33
[49] Novoselov K S, Geim A K, Morozov S V, Jiang D, Zhang Y, Dubonos S V, Grigorieva I V and Firsov A A 2004 Electric field effect in atomically thin carbon films *Science* **306** 666–9
[50] Sone J, Yamagami T, Aoki Y, Nakatsuji K and Hirayama H 2014 Epitaxial growth of silicene on ultra-thin ag (1 1 1) films *New J. Phys.* **16** 095004
[51] Dávila M, Xian L, Cahangirov S, Rubio A and Le Lay G 2014 Germanene: a novel two-dimensional germanium allotrope akin to graphene and silicene *New J. Phys.* **16** 095002
[52] Li L, Yu Y, Ye G J, Ge Q, Ou X, Wu H, Feng D, Chen X H and Zhang Y 2014 Black phosphorus field-effect transistors *Nat. Nanotechnol.* **9** 372
[53] Yang S *et al* 2017 C3n—a 2d crystalline, hole-free, tunable-narrow-bandgap semiconductor with ferromagnetic properties *Adv. Mater.* **29** 1605625
[54] Kappera R, Voiry D, Yalcin S E, Branch B, Gupta G, Mohite A D and Chhowalla M 2014 Phase-engineered low-resistance contacts for ultrathin MoS 2 transistors *Nat. Mater.* **13** 1128
[55] Mak K F, Lee C, Hone J, Shan J and Heinz T F 2010 Atomically thin MoS 2: a new direct-gap semiconductor *Phys. Rev. Lett.* **105** 136805
[56] Tonndorf P *et al* 2013 Photoluminescence emission and raman response of monolayer MoS 2, mose 2 and wse 2 *Opt. Express* **21** 4908–16
[57] Lu A-Y *et al* 2017 Janus monolayers of transition metal dichalcogenides *Nat. Nanotechnol.* **12** 744
[58] Naylor C H *et al* 2016 Monolayer single-crystal 1T-mote2 grown by chemical vapor deposition exhibits weak antilocalization effect *Nano Lett.* **16** 4297–304
[59] Wang Y *et al* 2017 Structural phase transition in monolayer mote 2 driven by electrostatic doping *Nature* **550** 487
[60] Okada M, Sawazaki T, Watanabe K, Taniguch T, Hibino H, Shinohara H and Kitaura R 2014 Direct chemical vapor deposition growth of WS_2 atomic layers on hexagonal boron nitride *ACS Nano* **8** 8273–7
[61] Fei Z, Palomaki T, Wu S, Zhao W, Cai X, Sun B, Nguyen P, Finney J, Xu X and Cobden D H 2017 Edge conduction in monolayer wte 2 *Nat. Phys.* **13** 677
[62] Xi X, Zhao L, Wang Z, Berger H, Forró L, Shan J and Mak K F 2015 Strongly enhanced charge-density-wave order in monolayer nbse 2 *Nat. Nanotechnol.* **10** 765
[63] Wang X, Lin J, Zhu Y, Luo C, Suenaga K, Cai C and Xie L 2017 Chemical vapor deposition of trigonal prismatic nbs 2 monolayers and 3r-polytype few-layers *Nanoscale* **9** 16607–11
[64] Zhang M *et al* 2015 Controlled synthesis of zrs2 monolayer and few layers on hexagonal boron nitride *J. Am. Chem. Soc.* **137** 7051–4
[65] Mañas-Valero S, García-López V, Cantarero A and Galbiati M 2016 Raman spectra of zrs2 and zrse2 from bulk to atomically thin layers *Appl. Sci.* **6** 264
[66] Xu K, Wang Z, Wang F, Huang Y, Wang F, Yin L, Jiang C and He J 2015 Ultrasensitive phototransistors based on few-layered hfs2 *Adv. Mater.* **27** 7881–7
[67] Fu W *et al* 2016 Controlled synthesis of atomically thin 1t-tas2 for tunable charge density wave phase transitions *Chem. Mater.* **28** 7613–8
[68] Ryu H *et al* 2018 Persistent charge-density-wave order in single-layer tase2 *Nano Lett.* **8** 689–94
[69] Zhao W, Dong B, Guo Z, Su G, Gao R, Wang W and Cao L 2016 Colloidal synthesis of VSe 2 single-layer nanosheets as novel electrocatalysts for the hydrogen evolution reaction *Chem. Commun.* **52** 9228–31
[70] Feng J, Sun X, Wu C, Peng L, Lin C, Hu S, Yang J and Xie Y 2011 Metallic few-layered VS2 ultrathin nanosheets: high two-dimensional conductivity for in-plane supercapacitors *J. Am. Chem. Soc.* **133** 17832–8
[71] Wang Y *et al* 2015 Monolayer ptse2, a new semiconducting transition-metal-dichalcogenide, epitaxially grown by direct selenization of pt *Nano Lett.* **15** 4013–8
[72] Zhao Y, Qiao J, Yu P, Hu Z, Lin Z, Lau S P, Liu Z, Ji W and Chai Y 2016 Extraordinarily strong interlayer interaction in 2d layered pts2 *Adv. Mater.* **28** 2399–407

[73] Wan C et al 2015 Flexible n-type thermoelectric materials by organic intercalation of layered transition metal dichalcogenide tis 2 Nat. Mater. 14 622
[74] Shao Y et al 2017 Epitaxial fabrication of two-dimensional nise2 on ni (1 1 1) substrate Appl. Phys. Lett. 111 113107
[75] Tongay S et al 2014 Monolayer behaviour in bulk res 2 due to electronic and vibrational decoupling Nat. Commun. 5 3252
[76] Oyedele A D et al 2017 Pdse2: pentagonal two-dimensional layers with high air stability for electronics J. Am. Chem. Soc. 139 14090–7
[77] Zhou L et al 2018 InSe monolayer: synthesis, structure and ultra-high second-harmonic generation 2D Mater. 5 025019
[78] Del Pozo-Zamudio O et al 2015 Photoluminescence of two-dimensional gate and gase films 2D Mater. 2 035010
[79] Zhou Y, Nie Y, Liu Y, Yan K, Hong J, Jin C, Zhou Y, Yin J, Liu Z and Peng H 2014 Epitaxy and photoresponse of two-dimensional gase crystals on flexible transparent mica sheets Acs Nano 8 1485–90
[80] Island J O, Buscema M, Barawi M, Clamagirand J M, Ares J R, Sánchez C, Ferrer I J, Steele G A, van der Zant H S and Castellanos-Gomez A 2014 Ultrahigh photoresponse of few-layer tis3 nanoribbon transistors Adv. Opt. Mater. 2 641–5
[81] Wang Y-Q et al 2016 Tunable electronic structures in wrinkled 2d transition-metal-trichalcogenide (tmt) hfte3 films Adv. Electron. Mater. 2 1600324
[82] Song C-L, Wang Y-L, Jiang Y-P, Li Z, Wang L, He K, Chen X, Ma X-C and Xue Q-K 2011 Molecular-beam epitaxy and robust superconductivity of stoichiometric fese crystalline films on bilayer graphene Phys. Rev. B 84 020503
[83] Liu H-J et al 2016 A metal–insulator transition of the buried mno2 monolayer in complex oxide heterostructure Adv. Mater. 28 9142–51
[84] Cai L, McClellan C J, Koh A L, Li H, Yalon E, Pop E and Zheng X 2017 Rapid flame synthesis of atomically thin moo3 down to monolayer thickness for effective hole doping of wse2 Nano Lett. 17 3854–61
[85] Xu S et al 2015 van der Waals epitaxial growth of atomically thin Bi2Se3 and thickness-dependent topological phase transition Nano Lett. 15 2645–51
[86] Kong D, Dang W, Cha J J, Li H, Meister S, Peng H, Liu Z and Cui Y 2010 Few-layer nanoplates of Bi2Se3 and Bi2Te3 with highly tunable chemical potential Nano Lett. 10 2245–50
[87] Mashtalir O, Lukatskaya M R, Zhao M-Q, Barsoum M W and Gogotsi Y 2015 Amine-assisted delamination of Nb2C mxene for Li-ion energy storage devices Adv. Mater. 27 3501–6
[88] Liu F, Zhou J, Wang S, Wang B, Shen C, Wang L, Hu Q, Huang Q and Zhou A 2017 Preparation of high-purity V2C mxene and electrochemical properties as Li-ion batteries J. Electrochem. Soc. 164 A709–13
[89] Lukatskaya M R, Mashtalir O, Ren C E, Dall'Agnese Y, Rozier P, Taberna P L, Naguib M, Simon P, Barsoum M W and Gogotsi Y 2013 Cation intercalation and high volumetric capacitance of two-dimensional titanium carbide Science 341 1502–5
[90] Melchior S A, Raju K, Ike I S, Erasmus R M, Kabongo G, Sigalas I, Iyuke S E and Ozoemena K I 2018 High-voltage symmetric supercapacitor based on 2d titanium carbide (mxene, ti2ctx)/carbon nanosphere composites in a neutral aqueous electrolyte J. Electrochem. Soc. 165 A501–11
[91] Liu G, Li Z, Hasan T, Chen X, Zheng W, Feng W, Jia D, Zhou Y and Hu P 2017 Vertically aligned two-dimensional sns 2 nanosheets with a strong photon capturing capability for efficient photoelectrochemical water splitting J. Mater. Chem. A 5 1989–95
[92] Li J, Guan X, Wang C, Cheng H-C, Ai R, Yao K, Chen P, Zhang Z, Duan X and Duan X 2017 Synthesis of 2d layered bii3 nanoplates, bii3/wse2van der Waals heterostructures and their electronic, optoelectronic properties Small 13 1701034
[93] Elias D C et al 2009 Control of grapheneś properties by reversible hydrogenation: evidence for graphane Science 323 610–3
[94] Nair R R et al 2010 Fluorographene: a two-dimensional counterpart of teflon Small 6 2877–84
[95] Wang L, Kutana A, Zou X and Yakobson B I 2015 Electro-mechanical anisotropy of phosphorene Nanoscale 7 9746–51
[96] Wang X, Wang D S, Ruqian W and Freeman A J 1996 Validity of the force theorem for magnetocrystalline anisotropy J. Magn. Magn. Mater. 159 337–41
[97] Olsen T 2016 Designing in-plane heterostructures of quantum spin hall insulators from first principles: 1 T-MoS 2 with adsorbates Phys. Rev. B 94 235106
[98] MacDonald A H, Vosko S H and Coleridge P T 1979 Extensions of the tetrahedron method for evaluating spectral properties of solids J. Phys. C: Solid State Phys. 12 2991–3002
[99] Heyd J, Scuseria G E and Ernzerhof M 2003 Hybrid functionals based on a screened coulomb potential J. Chem. Phys. 118 8207–15
[100] Kośmider K and Fernández-Rossier J 2013 Electronic properties of the MoS 2-WS 2 heterojunction Phys. Rev. B 87 075451
[101] Kang J, Tongay S, Zhou J, Li J and Wu J 2013 Band offsets and heterostructures of two-dimensional semiconductors Appl. Phys. Lett. 102 012111
[102] Kuisma M, Ojanen J, Enkovaara J and Rantala T T 2010 Kohn–Sham potential with discontinuity for band gap materials Phys. Rev. B 82 115106
[103] Castelli I E, Olsen T, Datta S, Landis D D, Dahl S, Thygesen K S and Jacobsen K W 2012 Computational screening of perovskite metal oxides for optimal solar light capture Energy Environ. Sci. 5 5814–9
[104] Baerends E 2017 From the Kohn–Sham band gap to the fundamental gap in solids. an integer electron approach Phys. Chem. Chem. Phys. 19 15639–56
[105] Hüser F, Olsen T and Thygesen K S 2013 Quasiparticle GW calculations for solids, molecules and two-dimensional materials Phys. Rev. B 87 235132
[106] Rasmussen F A, Schmidt P S, Winther K T and Thygesen K S 2016 Efficient many-body calculations for two-dimensional materials using exact limits for the screened potential: band gaps of MoS_2, *h*-BN, and phosphorene Phys. Rev. B 94 155406
[107] Tiago M L, Ismail-Beigi S and Louie S G 2004 Effect of semicore orbitals on the electronic band gaps of Si, Ge and GaAs within the GW approximation Phys. Rev. B 69 125212
[108] Klimeš J, Kaltak M and Kresse G 2014 Predictive GW calculations using plane waves and pseudopotentials Phys. Rev. B 90 075125
[109] Sundararaman R and Arias T A 2013 Regularization of the coulomb singularity in exact exchange by wigner-seitz truncated interactions: towards chemical accuracy in nontrivial systems Phys. Rev. B 87 165122
[110] Ismail-Beigi S 2006 Truncation of periodic image interactions for confined systems Phys. Rev. B 73 233103
[111] Rozzi C A, Varsano D, Marini A, Gross E K U and Rubio A 2006 Exact coulomb cutoff technique for supercell calculations Phys. Rev. B 73 205119
[112] Lee J, Huang J, Sumpter B G and Yoon M 2017 Strain-engineered optoelectronic properties of 2d transition metal dichalcogenide lateral heterostructures 2D Mater. 4 021016
[113] Ramasubramaniam A 2012 Large excitonic effects in monolayers of molybdenum and tungsten dichalcogenides Phys. Rev. B 86 115409
[114] Cheiwchanchamnangij T and Lambrecht W R L 2012 Quasiparticle band structure calculation of monolayer, bilayer and bulk MoS_2 Phys. Rev. B 85 205302
[115] Komsa H-P and Krasheninnikov A V 2012 Effects of confinement and environment on the electronic structure and exciton binding energy of MoS_2 from first principles Phys. Rev. B 86 241201
[116] Molina-Sánchez A, Sangalli D, Hummer K, Marini A and Wirtz L 2013 Effect of spin–orbit interaction on the optical spectra of single-layer, double-layer and bulk MoS_2 Phys. Rev. B 88 045412
[117] Shi H, Pan H, Zhang Y-W and Yakobson B I 2013 Quasiparticle band structures and optical properties of strained monolayer MoS_2 and WS_2 Phys. Rev. B 87 155304
[118] Conley H J, Wang B, Ziegler J I, Haglund R F, Pantelides S T and Bolotin K I 2013 Bandgap engineering of strained monolayer and bilayer MoS2 Nano Lett. 13 3626–30

[119] Hüser F, Olsen T and Thygesen K S 2013 How dielectric screening in two-dimensional crystals affects the convergence of excited-state calculations: monolayer MoS 2 *Phys. Rev.* B **88** 245309
[120] Qiu D Y, Felipe H and Louie S G 2016 Screening and many-body effects in two-dimensional crystals: monolayer MoS 2 *Phys. Rev.* B **93** 235435
[121] Shishkin M and Kresse G 2007 Self-consistent g w calculations for semiconductors and insulators *Phys. Rev.* B **75** 235102
[122] Schmidt P S, Patrick C E and Thygesen K S 2017 Simple vertex correction improves g w band energies of bulk and two-dimensional crystals *Phys. Rev.* B **96** 205206
[123] Shishkin M, Marsman M and Kresse G 2007 Accurate quasiparticle spectra from self-consistent GW calculations with vertex corrections *Phys. Rev. Lett.* **99** 246403
[124] Wang X, Jones A M, Seyler K L, Tran V, Jia Y, Zhao H, Wang H, Yang L, Xu X and Xia F 2015 Highly anisotropic and robust excitons in monolayer black phosphorus *Nat. Nanotechnol.* **10** 517
[125] Klots A *et al* 2014 Probing excitonic states in suspended two-dimensional semiconductors by photocurrent spectroscopy *Sci. Rep.* **4** 6608
[126] Ugeda M M *et al* 2014 Giant bandgap renormalization and excitonic effects in a monolayer transition metal dichalcogenide semiconductor *Nat. Mater.* **13** 1091
[127] Hill H M, Rigosi A F, Rim K T, Flynn G W and Heinz T F 2016 Band alignment in MoS_2/WS_2 transition metal dichalcogenide heterostructures probed by scanning tunneling microscopy and spectroscopy *Nano Lett.* **16** 4831–7
[128] Kormanyos A, Burkard G, Gmitra M, Fabian J, Zolyomi V, Drummond N D and Falko V 2015 k.p theory for two-dimensional transition metal dichalcogenide semiconductors *2D Mater.* **2** 022001
[129] Van De Walle C and Martin R 1989 Absolute deformation potentials—formulation and *ab initio* calculations for semiconductors *Phys. Rev. Lett.* **62** 2028–31
[130] Resta R, Colombo L and Baroni S 1990 Absolute deformation potentials in semiconductors *Phys. Rev.* B **41** 12358–61
[131] Wiktor J and Pasquarello A 2016 Absolute deformation potentials of two-dimensional materials *Phys. Rev.* B **94** 245411
[132] Marques M, Ullrich C, Nogueira F, Rubio A and Gross E 2006 Time-dependent density functional theory (https://doi.org/10.1007/B11767107)
[133] Hybertsen M S and Louie S G 1987 *Ab initio* static dielectric matrices from the density-functional approach. I. Formulation and application to semiconductors and insulators *Phys. Rev.* B **35** 5585–601
[134] Yan J, Mortensen J J, Jacobsen K W and Thygesen K S 2011 Linear density response function in the projector augmented wave method: applications to solids, surfaces and interfaces *Phys. Rev.* B **83** 245122
[135] Onida G, Reining L and Rubio A 2002 Electronic excitations: density-functional versus many-body Greeńs-function approaches *Rev. Mod. Phys.* **74** 601–59
[136] Sander T, Maggio E and Kresse G 2015 Beyond the tamm-dancoff approximation for extended systems using exact diagonalization *Phys. Rev.* B **92** 045209
[137] Latini S, Olsen T and Thygesen K S 2015 Excitons in van der Waals heterostructures: the important role of dielectric screening *Phys. Rev.* B **92** 245123
[138] Da Jornada F H, Qiu D Y and Louie S G 2017 Nonuniform sampling schemes of the Brillouin zone for many-electron perturbation-theory calculations in reduced dimensionality *Phys. Rev.* B **95**
[139] Drueppel M, Deilmann T, Krueger P and Rohlfing M 2017 Diversity of trion states and substrate effects in the optical properties of an MoS_2 monolayer *Nat. Commun.* **8** 2117
[140] Mouri S, Zhang W, Kozawa D, Miyauchi Y, Eda G and Matsuda K 2017 Thermal dissociation of inter-layer excitons in MoS_2 /$MoSe_2$ hetero-bilayers *Nanoscale* **9** 6674–9
[141] Chen H, Wen X, Zhang J, Wu T, Gong Y, Zhang X, Yuan J, Yi C, Lou J, Ajayan P M, Zhuang W, Zhang G and Zheng J 2016 Ultrafast formation of interlayer hot excitons in atomically thin MoS 2 /WS 2 heterostructures *Nat. Commun.* **7** 1–8
[142] Fang H *et al* 2014 Strong interlayer coupling in van der Waals heterostructures built from single-layer chalcogenides *Proc. Natl Acad. Sci.* **111** 6198–202
[143] Wilson N R, Nguyen P V, Seyler K, Rivera P, Marsden A J, Laker Z P, Constantinescu G C, Kandyba V, Barinov A, Hine N D, Xu X and Cobden D H 2017 Determination of band offsets, hybridization and exciton binding in 2D semiconductor heterostructures *Sci. Adv.* **3** e1601832
[144] Ceballos F, Bellus M Z, Chiu H-Y and Zhao H 2015 Probing charge transfer excitons in a MoSe2-WS_2 van der Waals heterostructure *Nanoscale* **7** 17523–8
[145] Liu H, Neal A T, Zhu Z, Luo Z, Xu X, Tománek D and Ye P D 2014 Phosphorene: an unexplored 2D semiconductor with a high hole mobility *ACS Nano* **8** 4033–41
[146] Yang J, Xu R, Pei J, Myint Y W, Wang F, Wang Z, Zhang S, Yu Z and Lu Y 2015 Optical tuning of exciton and trion emissions in monolayer phosphorene *Light Sci. Appl.* **4** 1–7
[147] Takagi S, Toriumi A and Iwase M 1994 On the universality of inversion layer mobility in Si MOSFET's: part I-effects of substrate impurity concentration *IEEE Trans. Electron Dev.* **41** 2357–62
[148] Cui X *et al* 2015 Multi-terminal transport measurements of MoS_2 using a van der Waals heterostructure device platform *Nat. Nanotechnol.* **10** 534–40
[149] Jin Z, Li X, Mullen J T and Kim K W 2014 Intrinsic transport properties of electrons and holes in monolayer transition-metal dichalcogenides *Phys. Rev.* B **90** 045422
[150] Gong C *et al* 2017 Discovery of intrinsic ferromagnetism in two-dimensional van der Waals crystals *Nature* **546** 265–9
[151] Bonilla M *et al* 2018 Strong room-temperature ferromagnetism in VSe2 monolayers on van der Waals substrates *Nat. Nanotechnol.* 13 289–93
[152] Huang C, Du Y, Wu H, Xiang H, Deng K and Kan E 2018 Prediction of intrinsic ferromagnetic ferroelectricity in a transition-metal halide monolayer *Phys. Rev. Lett.* **120** 147601
[153] Mermin N D and Wagner H 1966 Absence of ferromagnetism or antiferromagnetism in one- or two-dimensional isotropic Heisenberg models *Phys. Rev. Lett.* **17** 1133–6
[154] Lado J L and Fernández-Rossier J 2017 On the origin of magnetic anisotropy in two dimensional CrI_3 *2D Mater.* **4** 035002
[155] Olsen T 2017 Assessing the performance of the random phase approximation for exchange and superexchange coupling constants in magnetic crystalline solids *Phys. Rev.* B **96** 125143
[156] Low T, Chaves A, Caldwell J D, Kumar A, Fang N X, Avouris P, Heinz T F, Guinea F, Martin-Moreno L and Koppens F 2017 Polaritons in layered two-dimensional materials *Nat. Mater.* **16** 182
[157] Gjerding M N, Petersen R, Pedersen T, Mortensen N A and Thygesen K S 2017 Layered van der Waals crystals with hyperbolic light dispersion *Nat. Commun.* **8** 320
[158] Chen J *et al* 2012 Optical nano-imaging of gate-tunable graphene plasmons *Nature* **487** 77
[159] Andersen K and Thygesen K S 2013 Plasmons in metallic monolayer and bilayer transition metal dichalcogenides *Phys. Rev.* B **88** 155128
[160] Gjerding M N, Pandey M and Thygesen K S 2017 Band structure engineered layered metals for low-loss plasmonics *Nat. Commun.* **8** 15133
[161] Cudazzo P, Tokatly I V and Rubio A 2011 Dielectric screening in two-dimensional insulators: implications for excitonic and impurity states in graphane *Phys. Rev.* B **84** 085406
[162] Chernikov A, Berkelbach T C, Hill H M, Rigosi A, Li Y, Aslan O B, Reichman D R, Hybertsen M S and Heinz T F 2014 Exciton binding energy and nonhydrogenic rydberg series in monolayer WS 2 *Phys. Rev. Lett.* **113** 076802

[163] Olsen T, Latini S, Rasmussen F and Thygesen K S 2016 Simple screened hydrogen model of excitons in two-dimensional materials *Phys. Rev. Lett.* **116** 056401
[164] Jiang Z, Liu Z, Li Y and Duan W 2017 Scaling universality between band gap and exciton binding energy of two-dimensional Semiconductors *Phys. Rev. Lett.* **118** 266401
[165] Choi J-H, Cui P, Lan H and Zhang Z 2015 Linear scaling of the exciton binding energy versus the band gap of two-dimensional materials *Phys. Rev. Lett.* **115** 066403
[166] Seh Z W, Fredrickson K D, Anasori B, Kibsgaard J, Strickler A L, Lukatskaya M R, Gogotsi Y, Jaramillo T F and Vojvodic A 2016 Two-dimensional molybdenum carbide (mxene) as an efficient electrocatalyst for hydrogen evolution *ACS Energy Lett.* **1** 589–94
[167] Xie J, Zhang H, Li S, Wang R, Sun X, Zhou M, Zhou J, Lou X W D and Xie Y 2013 Defect-rich MoS2 ultrathin nanosheets with additional active edge sites for enhanced electrocatalytic hydrogen evolution *Adv. Mater.* **25** 5807–13
[168] Ridolfi E, Le D, Rahman T, Mucciolo E and Lewenkopf C 2015 A tight-binding model for MoS2 monolayers *J. Phys.: Condens. Matter* **27** 365501
[169] Mostofi A A, Yates J R, Lee Y-S, Souza I, Vanderbilt D and Marzari N 2008 Wannier90: a tool for obtaining maximally-localised wannier functions *Comput. Phys. Commun.* **178** 685–99
[170] Taherinejad M, Garrity K F and Vanderbilt D 2014 Wannier center sheets in topological insulators *Phys. Rev.* B **89** 115102
[171] Bokdam M, Amlaki T, Brocks G and Kelly P J 2014 Band gaps in incommensurable graphene on hexagonal boron nitride *Phys. Rev.* B **89** 201404
[172] Tritsaris G A, Shirodkar S N, Kaxiras E, Cazeaux P, Luskin M, Plecháč P and Cancès E 2016 Perturbation theory for weakly coupled two-dimensional layers *J. Mater. Res.* **31** 959–66
[173] Andersen K, Latini S and Thygesen K S 2015 Dielectric genome of van der Waals heterostructures *Nano Lett.* **15** 4616–21

6.2 Paper II

Stark shift and electric-field-induced dissociation of excitons in monolayer MoS_2 and hBN/MoS_2 heterostructures

PHYSICAL REVIEW B **94**, 041401(R) (2016)

Stark shift and electric-field-induced dissociation of excitons in monolayer MoS_2 and hBN/MoS_2 heterostructures

Sten Haastrup,[1] Simone Latini,[2,1] Kirill Bolotin,[3,4] and Kristian S. Thygesen[2,1]
[1]*Department of Physics, Center for Atomic-Scale Materials Design (CAMD), Technical University of Denmark, 2800 Kgs. Lyngby, Denmark*
[2]*Department of Physics, Center for Nanostructured Graphene (CNG), Technical University of Denmark, 2800 Kgs. Lyngby, Denmark*
[3]*Department of Physics, Vanderbilt University, Nashville Tennessee 37240, USA*
[4]*Department of Physics, Freie University, 14195 Berlin, Germany*
(Received 11 February 2016; published 1 July 2016)

Efficient conversion of photons into electrical current in two-dimensional semiconductors requires, as a first step, the dissociation of the strongly bound excitons into free electrons and holes. Here we calculate the dissociation rates and energy shift of excitons in monolayer MoS_2 as a function of an applied in-plane electric field. The dissociation rates are obtained as the inverse lifetime of the resonant states of a two-dimensional hydrogenic Hamiltonian which describes the exciton within the Mott-Wannier model. The resonances are computed using complex scaling, and the effective masses and screened electron-hole interaction defining the hydrogenic Hamiltonian are computed from first principles. For field strengths above 0.1 V/nm the dissociation lifetime is shorter than 1 ps, which is below the lifetime associated with competing decay mechanisms. Interestingly, encapsulation of the MoS_2 layer in just two layers of hexagonal boron nitride (hBN), enhances the dissociation rate by around one order of magnitude due to the increased screening. This shows that dielectric engineering is an effective way to control exciton lifetimes in two-dimensional materials.

DOI: 10.1103/PhysRevB.94.041401

Two-dimensional (2D) semiconductors, such as single- and few-layer transition-metal dichalcogenides, are presently being intensively researched due to their extraordinary electronic and optical properties which include strong light-matter interactions, spin-valley coupling, and easily tunable electronic states [1–14]. One of the hallmarks of the 2D semiconductors is the presence of strongly bound excitons with binding energies reaching up to 30% of the band gap. These large binding energies are mainly a result of the reduced dielectric screening in two dimensions [15–19]. Although such strongly bound excitons are highly interesting from a fundamental point of view (for example, in the context of Bose-Einstein condensates [20]) they are problematic for many of the envisioned applications of 2D materials, such as photodetectors and solar cells which rely on efficient conversion of photons into electrical currents. This is because the strong attraction between the electron and the hole makes it difficult to dissociate the excitons into free carriers.

Photocurrent measurements on suspended MoS_2 samples have found that the photocurrent produced by below-band-gap photons is strongly dependent on the applied voltage indicating that the electric field plays an important role in the generation of free carriers [21]. One way to increase the photoresponse could be to embed the active 2D material into a van der Waals heterostructure [22–24]. This embedding would enhance the screening of the electron-hole interaction without altering the overall shape of the band structure of the material. The effects of this increased screening on the exciton dissociation are studied in this Rapid Communication.

In general, rigorous calculations of exciton binding energies require a many-body approach, such as the Bethe-Salpeter equation (BSE) which directly finds the (real) poles of the interacting response function, corresponding to the neutral excitation energies of the system [25,26]. Such calculations are computationally demanding and typically only used to study excitations from the ground state, i.e., not in the presence of external fields. We mention, however, that the BSE has been used to study field-induced exciton dissociation in carbon nanotubes by fitting the BSE absorption spectrum to the Fano line shape [27]. In this Rapid Communication we take a different approach using that, under certain simplifying circumstances, the calculation of the many-body excitonic state can be reformulated as an effective hydrogenic Hamiltonian whose eigenvalues and eigenstates represent the exciton binding energies and the envelope wave function describing the relative electron-hole motion. This is the so-called Mott-Wannier model which has been instrumental in the description of excitons in inorganic bulk semiconductors. A 2D version of the Mott-Wannier model has recently been shown to yield exciton binding energies in good agreement with BSE calculations and experiments for both freestanding [15,16,18,19,28] and supported [15,28,29] transition-metal dichalcogenide layers. The dissociation rate of the exciton is then obtained by complex scaling, which is a formally exact technique to compute resonance energies and lifetimes. By employing a recently developed quantum-classical method for calculating the dielectric function of general van der Waals heterostructures, we predict the effect of embedding the MoS_2 in hBN on the screened electron-hole interaction and exciton dissociation rate.

When an in-plane constant electric field is applied to an exciton, it will eventually decay into a free electron and hole. This effect belongs to a class first studied by Keldysh [30] and Franz [31], who examined how the optical properties of semiconductors change in the presence of a static electric field. The application of a constant electric field changes the exciton from a bound state to a resonance with a finite lifetime equal to the inverse dissociation rate.

The literature on resonances in quantum physics is vast, and we will not go into the topic here but simply mention a few important facts. First, it should be understood that even the definition of a resonance is nontrivial. The reason for this can be understood from *Howland's razor* which states that no satisfactory definition of a resonance can depend only on the structure of a single operator on an abstract Hilbert space [32]. To illustrate the content of the statement consider the Stark effect in hydrogen: Let $\hat{H}(\epsilon) = -\frac{1}{2}\Delta - 1/r + \epsilon x$. It can be shown that $\hat{H}(\epsilon)$ is unitarily equivalent to $\hat{H}(\epsilon')$ for all nonzero ϵ and ϵ's. Since we expect the properties of the resonances and, in particular, their lifetimes to depend on field strength ϵ, this example shows that the resonance cannot be viewed only as a property of the operator $\hat{H}(\epsilon)$. Instead the notion of resonance is only meaningful when the real-space geometry of the given system and relevant boundary conditions on the wave functions are considered.

There are generally two approaches used to compute resonances. The so-called indirect methods identify resonances as the poles of the scattering amplitude analytically extended to the complex energy plane [33], whereas the direct methods obtain the resonance states directly as eigenstates of a complex scaled non-Hermitian Hamiltonian [34,35]. In this Rapid Communication we will use the latter approach.

To describe excitons in a 2D semiconductor we use a Mott-Wannier model of the form

$$\left[-\frac{\nabla_{\mathrm{2D}}^2}{2\mu_{\mathrm{ex}}} + W(\mathbf{r})\right]F(\mathbf{r}) = E_{\mathrm{b}}F(\mathbf{r}), \tag{1}$$

where μ_{ex} is the exciton effective mass $\mu_{\mathrm{ex}}^{-1} = m_{\mathrm{e}}^{-1} + m_{\mathrm{h}}^{-1}$, W is the screened electron-hole interaction, $\mathbf{r}$ is an in-plane position vector, and E_{b} denotes the exciton binding energy. In principle there should be an exchange term included here, but a full *ab initio* solution of the BSE has shown that the exchange term decreases the binding energy of the lowest exciton in MoS_2 by less than 4% [15], and the term can therefore be neglected.

The screened electron-hole interaction is obtained as the inverse Fourier transform of $[\epsilon_{\mathrm{2D}}(\mathbf{q})q]^{-1}$, where $\epsilon_{\mathrm{2D}}(\mathbf{q})$ is the static dielectric function of the 2D material and $1/q$ is the in-plane 2D Fourier transform of $1/r$. In the small-q limit, we can approximate ϵ as a linear function of q [16–19] so that

$$\epsilon_{\mathrm{2D}}(\mathbf{q}) = 1 + 2\pi\alpha q, \tag{2}$$

with α being the polarizability of the material. An analytic expression can then be obtained for the screened electron-hole interaction [17],

$$W(\mathbf{r}) = \frac{1}{4\alpha}[Y_0(x) - H_0(x)]_{x=r/2\pi\alpha}, \tag{3}$$

where Y_0 is a Bessel function of the second kind and H_0 is a Struve function. For later use we note that both of these functions are analytic on the entire complex plane away from $z = 0$.

The expression (3) for the screened interaction relies on a first-order expansion of $\epsilon_{\mathrm{2D}}(q)$ around $q = 0$; the validity of this approximation has been demonstrated for a number of freestanding 2D semiconductors [16,18,19] and recently for MoS_2 embedded in a few layers of hBN [15]. As a rule of thumb, the linear screening approximation [Eq. (2)] remains valid for intralayer excitons in van der Waals heterostructures as long as the in-plane exciton radius is large compared to the thickness of the heterostructure [15]. For thicker slabs, the linear approximation breaks down, and the fully q-dependent $\epsilon_{\mathrm{2D}}(\mathbf{q})$ must be used to obtain $W(r)$. We follow the common practice of using the static dielectric function for evaluating the screened interaction of the Mott-Wannier model. For details on how we calculate the dielectric functions of 2D layers and heterostructures we refer to Ref. [29]. Using these methods, the static dielectric function $\epsilon_{\mathrm{2D}}(q)$ can be calculated, and the slope at $q = 0$ can be determined.

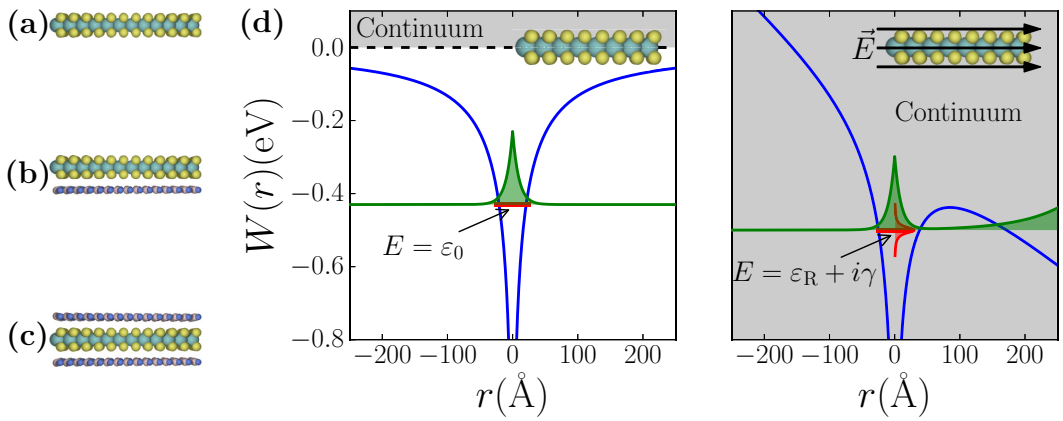

FIG. 1. (a)–(c) The three different structures considered in this Rapid Communication: isolated MoS_2, MoS_2 on a single layer of hBN, and MoS_2 sandwiched between two hBN layers. (d) Illustration of the Mott-Wannier model for monolayer MoS_2 in the absence (left) and presence (right) of an in-plane constant electric field. The exciton potential is shown in blue, the exciton wave function is sketched in green, and the energy is shown in red. When an electric field is applied, the energy of the exciton shifts down, and the sharp energy peak is broadened due to the coupling to the continuum of states.

Here we have considered a MoS_2 layer in three different configurations: isolated, placed on a single layer of *h*BN, and sandwiched between two *h*BN layers. The systems are sketched in Figs. 1(a)–1(c). The distance between the MoS_2 base plane and the *h*BN sheets was 5.1 Å and was chosen as the mean of the interlayer distance in pure MoS_2 and *h*BN. Sensitivity testing showed that varying this distance by 20% results in a variation in the slope of $\epsilon_{2D}(\mathbf{q})$ of less than 2%.

The lattices of MoS_2 and *h*BN are incommensurable, but the quantum-electrostatic heterostructure model introduced in Ref. [29] allows us to obtain the dielectric function of the heterostructure by electrostatic coupling of the response of the individual layers thus avoiding the issue of in-plane lattice mismatch. Table I shows the obtained polarizabilities and corresponding exciton binding energies. As expected, embedding the MoS_2 in *h*BN leads to an increase in screening and a reduction in the binding energy with the calculated results for the binding energy being in good agreement with *ab initio* calculations [15].

Once an in-plane constant electric field is applied to the system, the bound states of the Mott-Wannier Hamiltonian become metastable. The situation is illustrated in Fig. 1(d). In the model we have used, we assume that the band structure and, in particular, the effective mass of the exciton are not altered by the electric field.

Within the so-called direct methods, a resonance is defined as an eigenstate of the Hamiltonian under the boundary condition that only outgoing waves exist outside the scattering region. Such an eigenstate must necessarily have a complex eigenvalue $E = \epsilon_0 - i\gamma$ and a wave function that adopts the asymptotic form $e^{\pm iKx}$ for $x \to \pm\infty$ (focusing on the one-dimensional case for simplicity) where $K = k - i\kappa$ with $k > 0$ (an outgoing wave) and $\kappa > 0$. The latter condition implies that the wave function increases exponentially away from the scattering region. The decay rate of the resonance state, evaluated as the rate of decay of the probability for finding the particle in any finite region of space, is given by $\gamma = k\kappa$. It can be shown that the resonance eigenvalue E is a pole of the analytically continued scattering matrix [36].

To compute the resonance, one could in principle solve the Schrödinger equation with the appropriate boundary conditions. In practice, however, it is more convenient to perform a "complex scaling" of the Hamiltonian, whereby the coordinate $r \to e^{i\theta}r$ and $\nabla \to e^{-i\theta}\nabla$, and then solve for the eigenstates of the resulting (non-Hermitian) operator $\hat{H}_\theta$ with the more standard zero boundary conditions. For $\theta > \tan^{-1}(\gamma/k)$, the complex scaled resonance wave function (that is the wave function evaluated on the line $re^{i\theta}$ after analytic continuation) is an eigenstate of $\hat{H}_\theta$ with eigenvalue E but now decaying exponentially as $r \to \pm\infty$. The resonances thus appear as isolated complex eigenvalues of $\hat{H}_\theta$ with energy independent of θ and a square integrable wave function [37]. The complex scaled wave function of the bound states remain exponentially decaying eigenstates of $\hat{H}_\theta$ with real eigenvalues [34].

The unbound continuum states have a different behavior: If the potentials involved are localized, the asymptotic form of these states as $r \to \infty$ is e^{ikr} with $k, r \in \mathbb{R}$. They are thus finite at infinity but non-normalizable. If this is to remain true after the complex scaling is performed, the transformation $r \to re^{i\theta}$ must be accompanied by the transformation $k \to ke^{-i\theta}$. As the energy of a plane wave is proportional to k^2, the complex scaling operation results in the energy of the continuum states rotating into the complex plane at an angle of 2θ.

We mention that the complex scaling procedure cannot be applied to any potential $V(\mathbf{r})$ [35], but the class of potentials for which the procedure works is large enough to include the bare and the screened Coulomb potential [38] as well as a constant electric field [39].

In Fig. 2 we show an example of the spectrum of the complex-scaled exciton Hamiltonian for isolated MoS_2 in zero field for different values of the scaling parameter θ. The two classes of states, bound and unbound, can clearly be distinguished; for zero field there are no resonances.

For the systems shown in Figs. 2(a)– 2(c) we compute the screened interaction between charges located in the MoS_2 layer using the random phase approximation (RPA) and the local density approximation (LDA) as implemented in the GPAW code [40,41]. The response calculations were done with a 60×60 k-point grid and a 150-eV energy cutoff for $\mathbf{G}$ and $\mathbf{G}'$. The bandstructure obtained from the LDA calculations gives an effective exciton mass for MoS_2 of $0.27m_e$. Once α and μ_{ex} are known, the 2D eigenvalue problem for the complex-scaled Hamiltonian is solved on a real-space grid using radial coordinates. In order to converge the exciton energies, a large simulation cell is needed—significantly larger than the exciton radius, which is around 10 Å for all of the systems considered.

TABLE I. Calculated values for the polarizability (α) and exciton binding energy (E_b) for single-layer MoS_2 in the three configurations shown in Figs. 2(a)–2(c).

Material	α (a.u.)	E_b (eV)
MoS_2	11.1	0.62
MoS_2-*h*BN	13.0	0.55
*h*BN-MoS_2-*h*BN	16.1	0.47

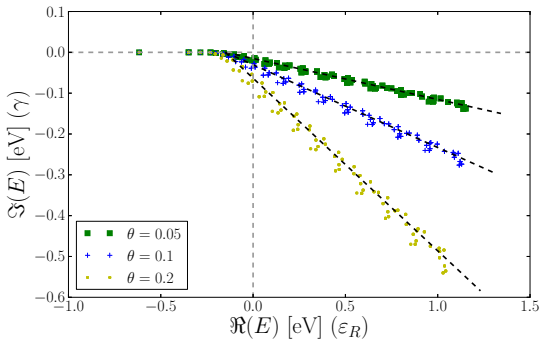

FIG. 2. The different behaviors of bound and continuum states under the complex scaling operation for the potential corresponding to isolated MoS_2. The black dashed lines start at -0.15 eV and have been rotated into the complex plane by -2θ for each of the complex scaling angles. Note that the continuum starts at -0.15 eV and not 0 because of the finite size of the simulation box.

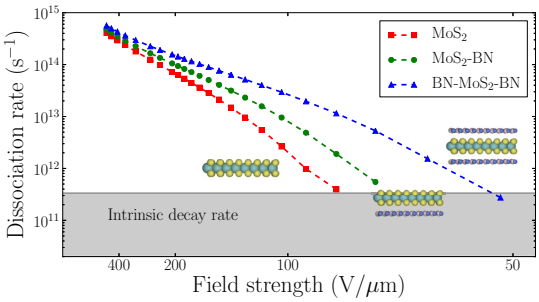

FIG. 3. The dissociation rate of an exciton in the MoS_2 layer as a function of in-plane field strength for the three different structures. The intrinsic decay rate spans between the defect-assisted fast decay of the excitons of 2–5 ps (upper limit) and the much slower radiative recombination of the excitons at room temperature (lower limit).

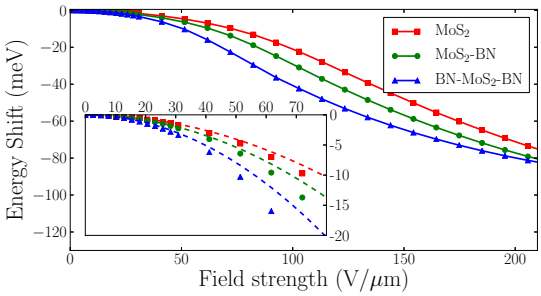

FIG. 4. The Stark shift in the MoS_2 heterostructures. The inset shows the shift for small fields, along with the shift predicted for a 2D hydrogen atom with an effective dielectric constant ϵ_{eff}; see Eq. (4).

As the screened potential has a logarithmic singularity at $r = 0$ while being virtually flat at the edge of the simulation cell, a nonlinear grid is used, which allows us to perform simulations in a disk of radius 250 Å. The Laplacian is represented by a finite-difference stencil. In order to avoid diagonalization of the full Hamiltonian, we used the iterative eigensolver ARPACK.

Figure 3 shows the MoS_2 exciton dissociation rate as a function of in-plane field strength for three different structures. As expected, larger fields lead to shorter lifetimes, and the rate is seen to depend roughly exponentially on $1/E$ for the considered field strengths. It can also be seen that the dissociation rate can be tuned to a high degree by changing the environment of the MoS_2. When MoS_2 is placed on a single layer of boron nitride, the extra screening greatly increases the dissociation rate, and similarly, when the MoS_2 is sandwiched between two layers of BN, the rate is even larger. This is as expected since larger screening results in more weakly bound excitons, which should in turn dissociate more readily. Adding more *h*BN layers on either side is expected to further enhance the screening and hence the dissociation rates, but this has not been pursued here as the linear screening model breaks down in this regime [15].

Along with information about the lifetime of the resonant states, the complex eigenvalue can provide information on the Stark shift of the resonance energy, an effect which is directly observable in optical absorption measurements. Figure 4 shows how the real part of the eigenvalue varies with field strength, and as expected, for small fields we observe a parabolic shift. The breakdown of this parabolic behavior occurs at smallest fields for the most screened excitons.

Recently, it has been shown that excitons in 2D materials can be described by a 2D hydrogen model with an effective dielectric constant [28], which for the linear screening described by Eq. (2) is given by $\epsilon_{\text{eff}} = \frac{1}{2} + \frac{1}{2}\sqrt{1 + 32\pi\alpha\mu/3}$. Based on this model and second-order perturbation theory, the shift can be predicted to be

$$\Delta E = -\frac{21}{64}\frac{\epsilon_{\text{eff}}^4}{\mu^3}E^2. \tag{4}$$

Figure 4 shows that this prediction fits well with our calculations for small fields.

In a real device, the field-induced dissociation of excitons described here is in competition with other decay mechanisms, such as direct radiative recombination [42], defect-assisted recombination [43], and exciton-exciton annihilation [44]. The relative importance of these effects is highly dependent on the temperature of the MoS_2, the presence and concentration of defects, and the exciton density.

At very low temperatures, the direct radiative decay of zero momentum excitons dominates with a characteristic lifetime of ∼200 fs [42,45,46]. At room temperature, most of the excitons have nonvanishing momenta, and the radiative recombination lifetime is ∼1 ns [42,43]. For these systems, defect-assisted recombination therefore becomes an important mechanism with a characteristic lifetime of 2–5 ps [43,47,48]. Exciton-exciton annihilations become important only when the density of excitons in a sample is large; equivalently when the average distance between excitons is small. At a density of 1×10^{12} cm^{-2}, the effective lifetime from annihilation is on the order of 10 ps [44].

The calculations performed here indicate that for field strengths larger than 0.1 V/nm, the dissociation lifetime is shorter than 1 ps in all the systems considered. A potential gradient of this size (0.1 V/nm) over the extent of the exciton (around 2 nm) is realistic to achieve close to the metal-MoS_2 contact region where charge transfer and interface dipole formation driven by Fermi-level mismatch can lead to significant variation of the potential and band energies even in the absence of an applied bias voltage. Under such conditions, the field-induced dissociation is faster than any other decay channel and should therefore dominate as indicated by the fact that in Fig. 3, the data points all lie above the shaded region.

To summarize we have used complex scaling to compute the lifetime of excitons in two-dimensional MoS_2 and MoS_2/hBN structures under an applied static electric field. The exciton was simulated using a 2D Mott-Wannier model which has previously been found to yield a reliable description of the lowest-lying excitonic states in transition-metal dichalcogenides. We found that for field strengths around 0.1 V/nm, the exciton dissociation is larger than the intrinsic exciton decay rate in MoS_2. Moreover, encapsulation in a few layers of *h*BN was found to increase the dissociation rate by an order of magnitude for fixed field strength due to the increased screening provided by the electrons in the *h*BN.

The authors gratefully acknowledge financial support from the Center for Nanostructured Graphene (Project No. DNRF103) financed by the Danish National Research Foundation.

[1] Q. H. Wang, K. Kalantar-Zadeh, A. Kis, J. N. Coleman, and M. S. Strano, Nat. Nanotechnol. **7**, 699 (2012).
[2] K. F. Mak, C. Lee, J. Hone, J. Shan, and T. F. Heinz, Phys. Rev. Lett. **105**, 136805 (2010).
[3] A. Splendiani, L. Sun, Y. Zhang, T. Li, J. Kim, C.-Y. Chim, G. Galli, and F. Wang, Nano Lett. **10**, 1271 (2010).
[4] A. Ramasubramaniam, Phys. Rev. B **86**, 115409 (2012).
[5] D. Y. Qiu, F. H. da Jornada, and S. G. Louie, Phys. Rev. Lett. **111**, 216805 (2013).
[6] M. M. Ugeda, A. J. Bradley, S.-F. Shi, H. Felipe, Y. Zhang, D. Y. Qiu, W. Ruan, S.-K. Mo, Z. Hussain, Z.-X. Shen *et al.*, Nat. Mater. **13** 1091 (2014).
[7] K. He, N. Kumar, L. Zhao, Z. Wang, K. F. Mak, H. Zhao, and J. Shan, Phys. Rev. Lett. **113**, 026803 (2014).
[8] D. Jariwala, V. K. Sangwan, L. J. Lauhon, T. J. Marks, and M. C. Hersam, ACS Nano **8**, 1102 (2014).
[9] M. Bernardi, M. Palummo, and J. C. Grossman, Nano Lett. **13**, 3664 (2013).
[10] O. Lopez-Sanchez, D. Lembke, M. Kayci, A. Radenovic, and A. Kis, Nat. Nanotechnol. **8**, 497 (2013).
[11] J. S. Ross, P. Klement, A. M. Jones, N. J. Ghimire, J. Yan, D. Mandrus, T. Taniguchi, K. Watanabe, K. Kitamura, W. Yao *et al.*, Nat. Nanotechnol. **9**, 268 (2014).
[12] A. Pospischil, M. M. Furchi, and T. Mueller, Nat. Nanotechnol, **9**, 257 (2014).
[13] K. F. Mak, K. He, C. Lee, G. H. Lee, J. Hone, T. F. Heinz, and J. Shan, Nature Mater. **12**, 207 (2013).
[14] A. Chernikov, T. C. Berkelbach, H. M. Hill, A. Rigosi, Y. Li, O. B. Aslan, D. R. Reichman, M. S. Hybertsen, and T. F. Heinz, Phys. Rev. Lett. **113**, 076802 (2014).
[15] S. Latini, T. Olsen, and K. S. Thygesen, Phys. Rev. B **92**, 245123 (2015).
[16] T. C. Berkelbach, M. S. Hybertsen, and D. R. Reichman, Phys. Rev. B **88**, 045318 (2013).
[17] P. Cudazzo, C. Attaccalite, I. V. Tokatly, and A. Rubio, Phys. Rev. Lett. **104**, 226804 (2010).
[18] P. Cudazzo, I. V. Tokatly, and A. Rubio, Phys. Rev. B **84**, 085406 (2011).
[19] O. Pulci, P. Gori, M. Marsili, V. Garbuio, R. Del Sole, and F. Bechstedt, Europhys. Lett. **98**, 37004 (2012).
[20] M. M. Fogler, L. V. Butov, and K. S. Novoselov, Nat. Commun. **5**, 4555 (2014).
[21] A. R. Klots, A. K. M. Newaz, B. Wang, D. Prasai, H. Krzyzanowska, J. Lin, D. Caudel, N. J. Ghimire, J. Yan, B. L. Ivanov, K. A. Velizhanin, A. Burger, D. G. Mandrus, N. H. Tolk, S. T. Pantelides, and K. I. Bolotin, Sci. Rep. **4** 6608 (2014).
[22] H. Terrones, F. López-Urías, and M. Terrones, Sci. Rep. **3** 1549 (2013).
[23] L. Britnell, R. Ribeiro, A. Eckmann, R. Jalil, B. Belle, A. Mishchenko, Y.-J. Kim, R. Gorbachev, T. Georgiou, S. Morozov *et al.*, Science **340**, 1311 (2013).
[24] A. Geim and I. Grigorieva, Nature (London) **499**, 419 (2013).
[25] G. Strinati, Phys. Rev. B **29**, 5718 (1984).
[26] G. Onida, L. Reining, and A. Rubio, Rev. Mod. Phys. **74**, 601 (2002).
[27] V. Perebeinos and P. Avouris, Nano Lett. **7**, 609 (2007).
[28] T. Olsen, S. Latini, F. Rasmussen, and K. S. Thygesen, Phys. Rev. Lett. **116**, 056401 (2016).
[29] K. Andersen, S. Latini, and K. S. Thygesen, Nano Lett. **15**, 4616 (2015).
[30] L. V. Keldysh, J. Exp. Theor. Phys. **33**, 994 (1957).
[31] W. Franz, Z. Naturforschung A **13a**, 484 (1958).
[32] B. Simon, Int. J. Quantum Chem. **14**, 529 (1978).
[33] J. Taylor, *Scattering Theory : The Quantum Theory on Nonrelativistic Collisions* (Wiley, New York, 1972), p. 477.
[34] E. Balslev and J. M. Combes, Commun. Math. Phys. **22**, 280 (1971).
[35] J. Aguilar and J. M. Combes, Commun. Math. Phys. **22**, 269 (1971).
[36] N. Hatano, K. Sasada, H. Nakamura, and T. Petrosky, Prog. Theor. Phys. **119**, 187 (2008).
[37] W. P. Reinhardt, Annu. Rev. Phys. Chem. **33**, 223 (1982).
[38] B. Simon, Ann. Math. **97**, 247 (1973).
[39] I. W. Herbst and B. Simon, Phys. Rev. Lett. **41**, 1759 (1978).
[40] J. J. Mortensen, L. B. Hansen, and K. W. Jacobsen, Phys. Rev. B **71**, 035109 (2005).
[41] J. Enkovaara, C. Rostgaard, J. J. Mortensen, J. Chen, M. Dulak, L. Ferrighi, J. Gavnholt, C. Glinsvad, V. Haikola, H. A. Hansen *et al.*, J. Phys.: Condens. Matter **22**, 253202 (2010).
[42] M. Palummo, M. Bernardi, and J. C. Grossman, Nano Lett. **15**, 2794 (2015).
[43] H. Shi, R. Yan, S. Bertolazzi, J. Brivio, B. Gao, A. Kis, D. Jena, H. G. Xing, and L. Huang, ACS Nano **7**, 1072 (2013).
[44] D. Sun, Y. Rao, G. A. Reider, G. Chen, Y. You, L. Brézin, A. R. Harutyunyan, and T. F. Heinz, Nano Lett. **14**, 5625 (2014).
[45] H. Wang, C. Zhang, W. Chan, C. Manolatou, S. Tiwari, and F. Rana, Phys. Rev. B **93**, 045407 (2016).
[46] C. Poellmann, P. Steinleitner, U. Leierseder, P. Nagler, G. Plechinger, M. Porer, R. Bratschitsch, C. Schueller, T. Korn, and R. Huber, Nature Mater. **14**, 889 (2015).
[47] T. Korn, S. Heydrich, M. Hirmer, J. Schmutzler, and C. Schüller, Appl. Phys. Lett. **99**, 102109 (2011).
[48] D. Lagarde, L. Bouet, X. Marie, C. R. Zhu, B. L. Liu, T. Amand, P. H. Tan, and B. Urbaszek, Phys. Rev. Lett. **112**, 047401 (2014).

6.3 Paper III

Dissociation of two-dimensional excitons in monolayer WSe

nature COMMUNICATIONS

ARTICLE

DOI: 10.1038/s41467-018-03864-y OPEN

Dissociation of two-dimensional excitons in monolayer WSe_2

Mathieu Massicotte[1], Fabien Vialla[1], Peter Schmidt[1], Mark B. Lundeberg[1], Simone Latini[2,3], Sten Haastrup[2], Mark Danovich[4], Diana Davydovskaya[1], Kenji Watanabe[5], Takashi Taniguchi[5], Vladimir I. Fal'ko[3], Kristian S. Thygesen[2,3], Thomas G. Pedersen[6,7] & Frank H.L. Koppens[1,8]

Two-dimensional (2D) semiconducting materials are promising building blocks for optoelectronic applications, many of which require efficient dissociation of excitons into free electrons and holes. However, the strongly bound excitons arising from the enhanced Coulomb interaction in these monolayers suppresses the creation of free carriers. Here, we identify the main exciton dissociation mechanism through time and spectrally resolved photocurrent measurements in a monolayer WSe_2 *p*–*n* junction. We find that under static in-plane electric field, excitons dissociate at a rate corresponding to the one predicted for tunnel ionization of 2D Wannier–Mott excitons. This study is essential for understanding the photoresponse of 2D semiconductors and offers design rules for the realization of efficient photodetectors, valley dependent optoelectronics, and novel quantum coherent phases.

[1] ICFO–Institut de Ciències Fotòniques, The Barcelona Institute of Science and Technology, Castelldefels, Barcelona 08860, Spain. [2] CAMD, Department of Physics, Technical University of Denmark, 2800 Kgs Lyngby, Denmark. [3] Center for Nanostructured Graphene (CNG), Technical University of Denmark, Kongens, Lyngby 2800, Denmark. [4] National Graphene Institute, University of Manchester, Booth St E, Manchester M13 9PL, UK. [5] National Institute for Materials Science, 1-1 Namiki, Tsukuba 305-0044, Japan. [6] Department of Physics and Nanotechnology, Aalborg University, DK-9220 Aalborg East, Denmark. [7] Center for Nanostructured Graphene (CNG), DK-9220 Aalborg Øst, Denmark. [8] ICREA – Institució Catalana de Recerça i Estudis Avancats, 08010 Barcelona, Spain. Correspondence and requests for materials should be addressed to F.H.L.K. (email: frank.koppens@icfo.eu)

As Johan Stark first observed in hydrogen atoms[1], applying an electric field on Coulomb-bound particles shifts their energy levels and eventually leads to their dissociation (Fig. 1a). In condensed matter physics, Wannier–Mott excitons display features analogous to those of hydrogen[2], but with the crucial difference that they recombine if they are not dissociated. Thermal energy is usually sufficient to ionize excitons in 3D semiconductors owing to their small binding energy E_B (typically a few meV). In contrast, quantum confinement effects and reduced Coulomb screening in low-dimensional materials give rise to large exciton binding energy ($E_B > 100$ meV), which prevents thermal or spontaneous dissociation even at elevated temperatures and exciton densities.

In particular, monolayer transition metal dichalcogenides (TMDs) have aroused tremendous interest due to their unique optical properties governed by prominent excitonic features[3–6] and spin- and valley dependent effects[7–11]. These 2D semiconductors provide an exciting testbed for probing the physics arising from many-body Coulomb interactions[6,12]. Recently, all-optical experiments have revealed a wealth of physical phenomena such as exciton[13,14], trion[15,16], and biexciton[17] formation, bandgap renormalization[18], exciton–exciton annihilation[19–25], and optical Stark effect[7,11]. Exciton dissociation, on the other hand, can in principle be assessed through photocurrent measurements since photocurrent directly stems from the conversion of excitons into free carriers. A large number of studies have investigated photodetection performances of 2D TMDs[26–29] and demonstrated their potential as photodetectors and solar cells. However, it is still unclear which dissociation process can overcome the large exciton binding energy and lead to efficient photocurrent generation in these devices. Theoretical studies suggest that strong electric fields may provide the energy required to dissociate the excitons[30–32], but the precise mechanism governing exciton dissociation in 2D TMDs remains to be experimentally investigated.

Here, we address this important issue by monitoring the exciton dissociation and subsequent transport of free carriers in a monolayer TMD *p*–*n* junction through spectrally and temporally resolved photocurrent measurements. Combining these two approaches allow us to assess and correlate two essential excitonic properties under static electric field, namely the Stark shift and the dissociation time. Further, we make use of the extreme thinness of 2D materials and their contamination-free assembly into heterostructures to reliably control the potential landscape experienced by the excitons. By placing the monolayer TMD in close proximity to metallic split gates, we can generate high in-plane electric fields and drive a photocurrent (PC). We find that at low field the photoresponse time of our device is limited by the rate at which excitons tunnel into the continuum through the potential barrier created by their binding energy, a process known as tunnel ionization (Fig. 1a). Tuning the electric field inside the *p*–*n* junction further allows us to disentangle various dynamical processes of excitons and free carriers and to identify the kinetic bottlenecks that govern the performance of TMD-based optoelectronic devices.

Results

Device structure and characterization. Figure 1b, c presents a schematic and optical micrograph of our lateral *p*–*n* junction

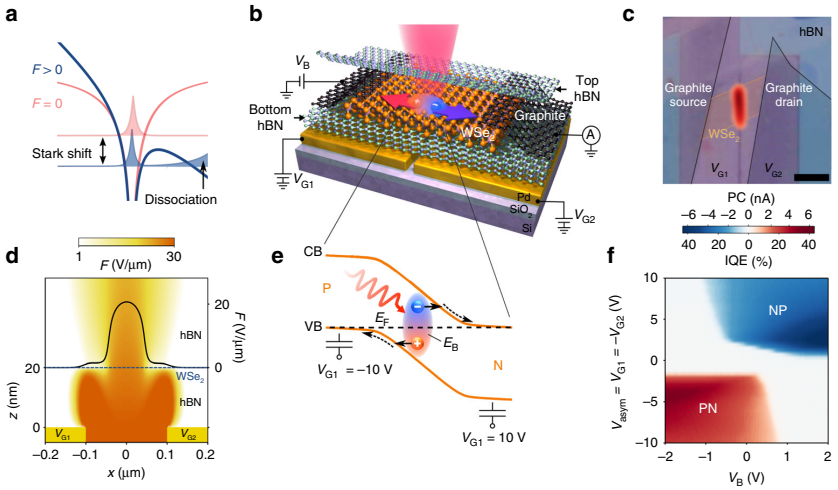

Fig. 1 Photocurrent generation by exciton dissociation in a monolayer WSe_2 *p*–*n* junction. **a** Illustration of a Wannier–Mott exciton in the absence (red) and presence (blue) of a static electric field. The exciton wave functions are represented by the shaded curves while the exciton potentials are shown by the thick solid lines. **b** Schematic of a monolayer WSe_2 device controlled by two local metal gates with voltages V_{G1} and V_{G2}. Two graphite flakes (colored in black) are placed on both sides of the WSe_2 layer (orange) and encapsulated between two hBN flakes (pale blue and green). **c** Optical image of a *p*–*n* junction device overlaid with a spatial PC map. The graphite and WSe_2 flakes are outlined and shaded for clarity. PC is measured at $V_{asym} = V_{G1} = -V_{G2} = -10$ V and $V_B = 0$ V, with a laser power $P = 1$ μW and a photon energy $h\nu = 1.65$ eV. The scale bar is 4 μm. **d** Side view of the electric field distribution F across a device made of hBN (20 nm thick), monolayer WSe_2 (dotted blue line), and hBN (30 nm thick) atop metallic split gates separated by 200 nm (yellow rectangles). The field is calculated for $V_{asym} = -10$ V and $V_B = 0$. The color bar above indicates the magnitude of $\log_{10}(F)$. The in-plane electric field $F(x)$ inside the WSe_2 is shown by the solid black line (right axis). **e** Band diagram of the *p*–*n* junction between $x = -0.1$ and 0.1 μm (cf., Fig. 1d) calculated for $V_{asym} = -10$ V and $V_B = 0$ V. The solid orange lines represent the conduction (CB) and valence band (VB) and the black dotted line corresponds to the Fermi level (E_F). Following resonant optical excitation (red sinusoidal arrow), excitons are generated and dissociated via tunnel ionization (solid black arrows). The resulting free carriers drift out of the junction (dotted black arrows) and generate a photocurrent. **f** PC measured at the junction as a function of V_{asym} and V_B, with a laser power $P = 0.5$ μW and a photon energy $h\nu = 1.65$ eV. The color bar between **c** and **f** displays the magnitude of the PC as well as the internal quantum efficiency, $\mathrm{IQE} = \frac{\mathrm{PC}}{e_0}\frac{h\nu}{AP}$, where $A = 5\%$ is the absorption coefficient

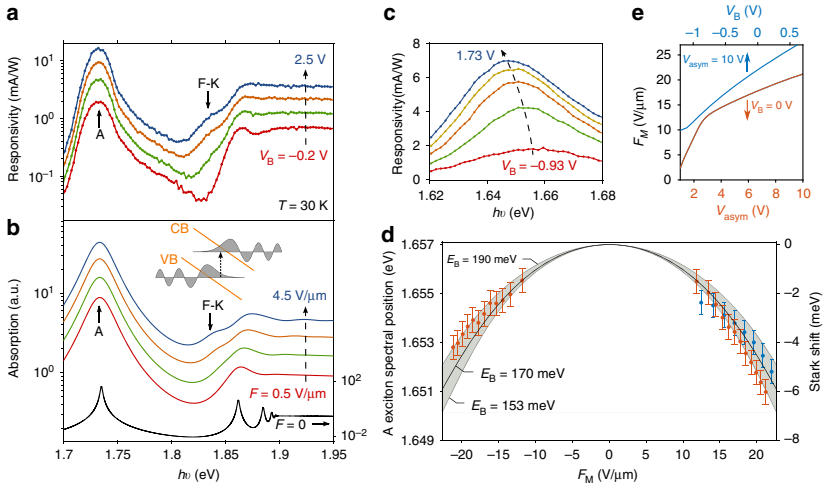

Fig. 2 Electroabsorption and Stark effect in monolayer WSe_2 *p*–*n* junctions. **a** Responsivity (PC/*P*) spectra measured at the *p*–*n* junction of device 3 (Supplementary Fig. 2) for various V_B, with a laser power $P = 1$ μW and $T = 30$ K. The spectra are vertically shifted (by a factor of 1.5) for clarity. **b** Absorption spectra calculated using a Wannier–Mott exciton model at different in-plane electric fields *F*. The solid colored lines (left axis) were calculated with a phenomenological line shape broadening of 15 meV, while the black solid line (right axis) was calculated without broadening. All spectra are vertically shifted for clarity. Inset: Schematics illustrating the sub-bandgap, field-induced absorption increase due to the Franz–Keldysh (F-K) effect. The application of an in-plane field tilts the conduction (CB) and valence band (VB) of the semiconductor (orange lines) and allows the wave functions of the free electrons and holes (gray shaded curves) to leak into the bandgap, which results in an increase of the sub-bandgap absorption (dotted arrow). **c** Responsivity spectra (around the A exciton) measured on device 1 (shown in Fig. 1c) at various V_B, with a laser power $P = 0.5$ μW, $V_{asym} = 10$ V and at room temperature. **d** Position of the A exciton as a function of the calculated F_M for the same values of V_{asym} and V_B as the one shown in **e**. Orange data points correspond to different values of V_{asym} at $V_B = 0$ V, while blue data points represent different values of V_B at $V_{asym} = 10$ V. Error bars correspond to the spectral resolution of our measurements. The calculated Stark shifts (right axis) induced by the F_M are represented by the black solid line ($E_B = 170$ meV) and the gray shaded curves ($E_B = 153$ and 190 meV). The latter values represent the uncertainty bounds of E_B arising from the uncertainty (95% confidence interval) in the measured polarizability. **e** Maximum in-plane electric field F_M calculated as a function of V_{asym} (with $V_B = 0$ V, solid orange line) and as a function of V_B (with $V_{asym} = 10$ V, solid blue line)

device made by assembling exfoliated flakes on metallic split gates (V_{G1} and V_{G2}) separated by 200 nm (see "Methods"). Few-layer graphite flakes placed on both ends of a monolayer WSe_2 flake serve as ambipolar electrical contacts[33] that we use to apply a bias voltage V_B and collect the photogenerated charges. The lateral graphite-WSe_2-graphite assembly is fully encapsulated in hexagonal boron nitride, typically 20 nm thick, which provides a clean and flat substrate. Three devices were measured (see Supplementary Note 1 and Supplementary Figs. 1–3), but unless otherwise specified, all measurements presented in the main text are obtained at room temperature from the device shown in Fig. 1c.

Tuning of bias and gate voltages allows us to finely control the in-plane electric field *F*. Finite-element and analytical calculations of the electric field distribution in our device (see Supplementary Note 2 and Supplementary Figs. 4–7) provide us with a precise estimate of *F* and the electrostatic doping inside the WSe_2 (Fig. 1d). Applying gate voltages of opposite polarity ($V_{asym} = V_{G1} = -V_{G2} = -10$ V) leads to the formation of a sharp *p*–*n* junction (Fig. 1e) with an in-plane electric field reaching 21 V μm^{-1} (Fig. 1d). The photoresponse that we observed at the junction (Fig. 1c) follows a photodiode-like behavior: PC is only generated in the *p*–*n* or *n*–*p* configuration (see Supplementary Fig. 1c) and can be increased by applying a reverse bias voltage (Fig. 1f).

Spectral response. We probe the absorption spectrum in the photoactive region by measuring the PC as a function of photon energy $h\nu$ at a constant laser power *P* and in-plane electric field *F*. Figure 2a shows the responsivity (PC/*P*) spectra of a device similar to the one presented in Fig. 1c, measured at various V_B and at low temperature ($T = 30$ K) in order to reduce thermal broadening. We observe a pronounced peak at a photon energy $h\nu = 1.73$ eV, corresponding to the A exciton, and a step-like increase around 1.87 eV. For increasing electric field, this step-like feature broadens and an additional shoulder appears at 1.83 eV.

To identify the various spectral features, we compare the experimental spectra with first-principles calculations for a monolayer WSe_2 embedded in hBN (see Supplementary Note 3 and Supplementary Fig. 8). By including the electronic screening from the hBN layers in the many-body G_0W_0 and Bethe–Salpeter Equation (BSE) frameworks[34] we obtain a bandgap of 1.85 eV and a lowest bound exciton at 1.67 eV in good agreement with the experimental spectra. To account for the effect of a constant in-plane electric field we use a model based on the 2D Wannier equation (see Supplementary Note 4 and Supplementary Fig. 9). In these model calculations, screening by the TMD itself as well as the surrounding dielectric materials is described via the Keldysh potential for the electron–hole interaction. Figure 2b shows calculated absorption spectra for different in-plane fields *F*. Excellent agreement between experiment and calculations is found assuming a bandgap of 1.9 eV, which yields a binding energy of $E_B = 170$ meV for the A excitons consistent with the first-principles calculations. The unbroadened spectrum calculated at zero field (Fig. 2b, solid black line) confirms the presence of multiple overlapping excited excitonic peaks below the

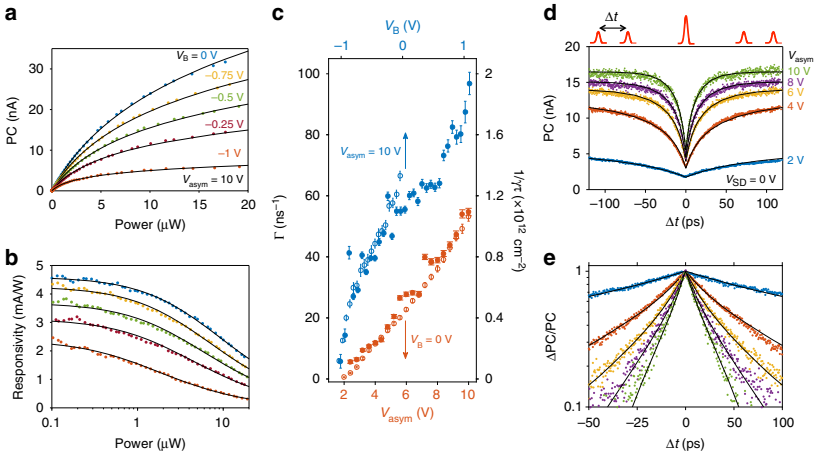

Fig. 3 Determination of the photoresponse time τ by nonlinear and time-resolved photocurrent measurements. **a** PC vs. laser power P for various V_B, at $V_{asym} = 10$ V and $h\nu = 1.65$ eV. **b** Responsivity (PC/P) in the same conditions as **a**. The solid black lines in **a** and **b** are fits to the data of PC $\propto \ln(1 + \gamma\tau N_0)$. **c** Photoresponse rate $\Gamma = \frac{1}{\tau}$ (filled circles, left axis) obtained from the TRPC measurements (shown in **d**, **e** and Supplementary Fig. 10d) and $\frac{\Gamma}{\gamma} = \frac{1}{\gamma\tau}$ (open circles, right axis) obtained from the power dependence measurements (shown in **a**, **b** and Supplementary Fig. 10a) as a function of V_{asym} at $V_B = 0$ V (orange, lower axis) and V_B at $V_{asym} = 10$ V (blue, top axis). Good agreement between TPRC and nonlinear PC measurements is found for an EEA rate of $\gamma = 0.05$ cm^2 s^{-1}. The error bars correspond to the standard deviations obtained from the fits. **d** PC as a function of time delay Δt between two pulses (illustrated above the plot) at various value of V_{asym}, with time-averaged $P = 100$ μW and $V_B = 0$ V. **e** Same data as in **d** but plotted with the normalized $\frac{\Delta PC}{PC} = \frac{PC(\Delta t \to \infty) - PC(\Delta t)}{PC(\Delta t \to \infty) - PC(\Delta t = 0)}$. The solid black lines in **d** and **e** are fits to the data using the model described in the Supplementary Note 5

bandgap. The calculated spectra for higher field reproduce remarkably well the field-induced increase of the sub-bandgap absorption observed experimentally. This is a manifestation of the Franz–Keldysh effect, which results from the leakage of the free electron and hole wave functions into the bandgap (inset of Fig. 2b). We note that our experimental value of E_B agrees well with the one estimated from the diamagnetic shift of a monolayer WSe_2 encapsulated between silica and hBN[35]. Larger E_B has been observed in SiO_2-supported WSe_2 samples[36–38], underlining the role of the dielectric environment on the excitonic properties[39].

Excitonic Stark effect. Turning our attention to the A exciton photocurrent peak, we observe a pronounced red-shift as V_B (Fig. 2c) and V_{asym} increase. We attribute this to the DC Stark effect. In first approximation, the Stark shift of a 1s exciton (without dipole moment) is given by $\Delta E = -\frac{1}{2}\alpha F^2$, where α is the in-plane polarizability. As shown in Fig. 2d, the A exciton energy shows a quadratic dependence with the maximum in-plane electric field F_M calculated for different values of V_{asym} and V_B (Fig. 2e), yielding a polarizability of $\alpha = (1 \pm 0.2) \times 10^{-6}$ Dm/V. This shift matches well with the predicted polarizability of $\alpha = 9.4 \times 10^{-7}$ Dm/V for $E_B = 170$ meV, thus supporting our previous spectral analysis. Interestingly, we note that the measured in-plane polarizability is two order of magnitude larger than the out-of-plane value recently obtained in PL experiments[40]. This strong anisotropy confirms the 2D nature of the A exciton and demonstrates the advantage of using in-plane electric fields for controlling the optical properties of TMDs[31].

Photoresponse dynamics. Along with the Stark shift, the application of a large in-plane electric field shortens the lifetime of excitons, which eventually decay into free electrons and holes (Fig. 1a). We probe these decay dynamics by assessing the photoresponse time τ of the device with time-resolved photocurrent measurements (TRPC), banking on the nonlinear photoresponse of the WSe_2. Figure 3a, b shows the strong sublinear power dependence of the photocurrent (and the corresponding responsivity) under resonant pulsed optical excitation ($h\nu = 1.65$ eV, see "Methods"). Many physical processes may be responsible for or contribute to the observed sublinearity, including phase space filling[41] and dynamic screening effects (e.g., bandgap renormalization[18]). These many-body effects become intricate as the exciton gas approaches the Mott transition[42]. However, recent time-resolved spectroscopy[19,22] and photoluminescence[20,23] experiments indicate that in this exciton density regime ($10^{11} \lesssim N \lesssim 10^{13}$ cm^{-2}), exciton–exciton annihilation (EEA, or exciton Auger recombination) is the dominant decay process for excitons in TMDs[24]. To account for EEA in the rate equation governing the photocurrent we add a loss term that scales quadratically with the exciton density (γN^2, where γ is the EEA rate). Assuming that each pulse generates an initial exciton population N_0, this model yields PC $\propto \ln(1 + \gamma\tau N_0)$, which reproduces well the observed sublinear photoresponse (black lines in Fig. 3a, b, see Supplementary Note 5). Moreover, the fits capture adequately the variation of the sublinear photoresponse with bias (Fig. 3a, b) and gate (Supplementary Fig. 10a) voltages, from which we extract the values of $1/\gamma\tau$ (Fig. 3c). Hence, these nonlinear measurements already offer an indirect way to probe the photoresponse time.

In order to directly extract τ,we resonantly excite A excitons in the p–n junction with a pair of 200 fs-long laser pulses separated by a variable time delay Δt, for various values of V_{asym} (Fig. 3d, e). Due to the sublinear power dependence, the photocurrent displays a symmetric dip when the two pulses coincide in time ($\Delta t = 0$). By extending our nonlinear photocurrent model to the case of two time-delayed pulses (see Supplementary Note 5 and Supplementary Fig. 10), we can show that the time dependence of this dip is dominated by an exponential time constant corresponding to the intrinsic photoresponse time τ of the device. The photoresponse rate $\Gamma = \frac{1}{\tau}$ is extracted from TRPC measurements at various values of V_{asym} (Fig. 3d, e) and V_B (see Supplementary Fig. 10d) and presented in Fig. 3c. We observe

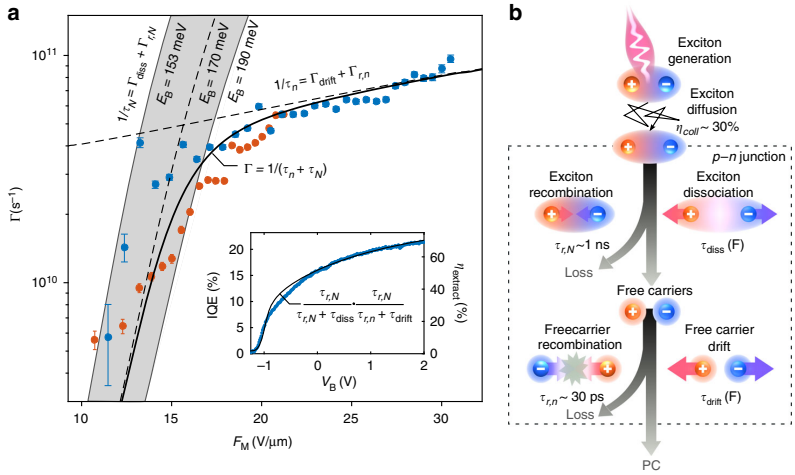

Fig. 4 Dynamic processes governing the photoresponse of monolayer WSe_2 *p*–*n* junctions. **a** Photoresponse rate $\Gamma = \frac{1}{\tau}$ measured by TRPC (same data as Fig. 3c) vs. maximum in-plane electric field F_M calculated for various values of V_{asym} (with $V_B = 0$ V, orange points) and V_B (with $V_{asym} = 10$ V, blue points). At low field ($F_M < 15$ V μm^{-1}), the photoresponse is well described by the total exciton rate $\Gamma_N = \frac{1}{\tau_N} = \Gamma_{diss}(F_M) + \Gamma_{r,N}$, where $\tau_{r,N} = 1/\Gamma_{r,N}$ is the exciton lifetime at zero field ($\tau_{r,N} \sim 1$ ns) and Γ_{diss} is the exciton dissociation rate predicted by the 2D Wannier–Mott exciton (see Supplementary Note 4) with a binding energy between $E_B = 153$ and 190 meV (gray shaded curves) and $E_B = 170$ meV (dotted black line). At high field ($F_M > 20$ V μm^{-1}), the photoresponse is governed by the total free carrier rate $\Gamma_n = \frac{1}{\tau_n} = \Gamma_{drift}(F_M) + \Gamma_{r,n}$ (dotted black line), where $\tau_{r,n} = 1/\Gamma_{r,n}$ is the free carrier lifetime at zero field ($\tau_{r,n} \sim 30$ ps) and Γ_{drift} is the rate at which carriers (with a mobility $\mu = 4$ cm^2 V^{-1} s^{-1}) drift out of the junction (see Supplementary Note 6). Since exciton dissociation and free carrier drift are consecutive processes, the total photoresponse rate of the device is $\Gamma \approx \frac{1}{\tau_N + \tau_n}$ (black solid line). Inset: IQE vs. V_B measured at $V_{asym} = 10$ V extracted from Fig. 1f (left axis, blue data points). Extraction efficiency, $\eta_{extract} = \frac{\tau_{r,n}}{\tau_{r,n}+\tau_{drift}} \frac{\tau_{r,N}}{\tau_{r,N}+\tau_{diss}}$, calculated with our model vs. V_B (right axis, black solid line). **b** Schematic of the processes contributing to the photoresponse of the device. Excitons are generated by resonant optical excitation and approximatively 30% (η_{coll}) of them reach the *p*–*n* junction by diffusion during their lifetime $\tau_{r,N}$. Excitons entering the *p*–*n* junctions (black dotted box) may either recombine with a time constant $\tau_{r,N}$ or dissociate by tunnel ionization at a rate Γ_{diss}. The resultant free carriers generate a photocurrent as they drift out of the junction at a rate Γ_{drift}, but a fraction is also lost due to their finite lifetime $\tau_{r,n}$. Holes and electrons are represented by red and blue spheres

that Γ increases markedly with gate and bias voltages, and remarkably follows the same trend as the values of $1/\gamma\tau$ obtained from the power dependence measurements. Comparing these two results, we obtain an EEA rate of $\gamma = 0.05$ cm^2/s, which is similar to those found in WSe_2[19,23], MoS_2[21,22], and WS_2[20,25]. We also note that the shortest response time we measure, $\tau = 10.3 \pm 0.4$ ps, translates into a bandwidth of $f = 0.55/\tau \sim 50$ GHz, which compares with the fastest responses measured in TMD-based photodetectors[43,44].

Discussion

To directly address the exciton dissociation caused by the in-plane electric field F_M, we examine the dependence of the photoresponse rate Γ on F_M at the *p*–*n* junction (Fig. 4a). Clearly, two regimes can be distinguished. The rapid increase of Γ with F_M is attributed to dissociation by tunnel ionization. We verify this by comparing the measured Γ to the calculated tunnel ionization rate Γ_{diss}, obtained by introducing the complex scaling formalism in the 2D Wannier–Mott exciton model (see Supplementary Note 4 and Supplementary Table 1). According to this model, Γ_{diss} can be evaluated in first approximation by the product of the "attempt frequency"[45], which scales with E_B/h, and the exponential tunneling term $\exp(-E_B/e_0 dF_M)$, where e_0 is the elementary charge, d is the exciton diameter, and h is the Plank constant. We find that the dependence of Γ at low field ($F_M < 15$ V μm^{-1}) coincides well with the calculated dissociation rate of excitons with $E_B =$ 170 meV, in agreement with our photocurrent spectroscopy analysis. More importantly, this shows that in the low-field regime the exciton dissociation process is the rate-limiting step governing the generation of photocurrent. We note that in multilayer TMDs, where $E_B \sim 50$ meV, the ionization rate is two orders of magnitude larger than in the monolayer case[46], and hence this process was not found to limit the photoresponse rate of multilayer devices[44].

At high electric field ($F_M > 20$ V μm^{-1}), the photoresponse rate deviates from the dissociation rate-limited model and enters a new regime characterized by a more moderate increase of Γ with F_M. The observed linear scaling of $\Gamma(F_M)$ suggests that, in this regime, the photoresponse rate is limited by the drift-diffusive transport of free carriers out of the *p*–*n* junction. By considering a carrier drift velocity $v_{drift} = \mu F$, we estimate that carriers generated in the center of the junction of length $L = 200$ nm escape the junction at a rate $\Gamma_{drift} = 2\mu F/L$. Comparing this simple expression (dotted line in Fig. 4a) to the measured Γ at high field, we find $\mu = 4 \pm 1$ cm^2 V^{-1} s^{-1}, which is very similar to the room temperature field-effect mobility that we measure in our sample ($\mu_{FE} \sim 3$ cm^2 V^{-1} s^{-1}, see Supplementary Note 1).

A complete photocurrent model is achieved by introducing competing loss mechanisms caused by the radiative and non-radiative recombination of excitons (see Supplementary Note 6). Good agreement with the experimental data is obtained by considering the finite lifetime of excitons ($\tau_{r,N} = 1/\Gamma_{r,N} \sim 1$ ns[20,23], see Supplementary Note 1) and free carriers ($\tau_{r,n} = 1/\Gamma_{r,n} \sim 30$ ps[41]) at zero electric field. This comprehensive picture of the dynamical processes (Fig. 4b) offers valuable insights into the internal quantum efficiency (IQE) of the photocurrent generation mechanism in this device. Indeed, the efficiency η of each

photocurrent step depends on the competition between the PC-generating (τ_{drift}, τ_{diss}) and the loss ($\tau_{r,N/n}$) pathways, such that $\eta_{diss/drift} = \tau_{r,N/n}/(\tau_{r,N/n} + \tau_{diss/drift})$. In the inset of Fig. 4a, we compare the IQE measured at low power as a function of V_B with the total extraction efficiency $\eta_{extract} = \eta_{drift}\,\eta_{diss}$ derived from the kinetic model shown in Fig. 4b. We find that $\eta_{extract}$ captures very well the bias dependence of the IQE, indicating that we correctly identified the relevant PC-generating processes. The field-independent discrepancy of 30% is attributed to the collection efficiency η_{coll}, which we define as the ratio between the number of excitons reaching the *p*–*n* junction and the number of absorbed photons. This value coincides with our analysis of the measured photocurrent profile and with the prediction of our exciton diffusion model (see Supplementary Note 7 and Supplementary Fig. 11).

In summary, our study offers a global understanding of the fundamental mechanisms governing the exciton dynamics and associated photoresponse in monolayer TMDs under in-plane electric field. We demonstrate that despite their large binding energy, photogenerated excitons can rapidly dissociate into free carriers via tunnel ionization, thereby outcompeting recombination processes. Importantly, this knowledge allows us to identify the main material properties that limit photocurrent generation in TMDs such as carrier mobility, exciton binding energy, and lifetime. This provides guidelines in terms of device design, material quality improvement, and Coulomb engineering of the van der Waals heterostructure to further improve the performances of TMD-based optoelectronics devices and develop their applications in valleytronics. We finally note that the observed Stark and Franz–Keldysh effects open up exciting opportunities for modulating light with 2D materials[47].

Methods

Device fabrication. Exfoliated layers are assembled in a van der Waals heterostructure using the same technique as described in ref. [48]. The monolayer of WSe_2 is identified by photoluminescence measurement (see Supplementary Note 1). The heterostructure is deposited onto metallic split gates (15 nm palladium) defined by electron-beam lithography on a degenerately doped silicon substrate covered with a 285-nm-thick SiO_2 layer. The two graphite flakes are electrically connected by one-dimensional contacts[48] made of Ti/Au (2/100 nm).

Photocurrent measurements. Photocurrent measurements are performed using a photocurrent scanning microscope setup, where a laser beam is focused by a microscope objective (Olympus LUCPlanFLN × 40) onto the device placed on a piezoelectric stage (Attocube ANC300). Photocurrent is measured with a pre-amplifier and a lock-in amplifier synchronized with a mechanical chopper. A supercontinuum laser (NKT Photonics SuperK Extreme), with a pulse duration of ~40 ps, repetition rate of 40 MHz and tunable wavelength (from 500 to 1500 nm) is employed to characterize the devices, perform photocurrent spectroscopy, and measure the photocurrent power dependence. Time-resolved photocurrent measurements are performed using a Ti:sapphire laser (Thorlabs Octavius) with ~200 fs pulses (at the sample), with a repetition rate of 85 MHz, and centered at $h\nu = 1.65$ eV (FWHM = 0.07 eV), which corresponds to the A exciton absorption peak. The laser beam is split into two arms and recombined using 50/50 beamsplitters. A mechanical chopper modulates the laser beam in one arm (pump), while the other arm (probe) has a motorized translation stage that allows for the generation of a computer-controlled time delay Δt between the two pulses.

Data availability. The data that support the findings of this study are available from the corresponding author on request.

Received: 6 October 2017 Accepted: 19 March 2018
Published online: 24 April 2018

References

1. Stark, J. Observation of the separation of spectral lines by an electric field. *Nature* **92**, 401–401 (1913).
2. Koch, S. W., Kira, M., Khitrova, G. & Gibbs, H. M. Semiconductor excitons in new light. *Nat. Mater.* **5**, 523–531 (2006).
3. Mak, K. F., Lee, C., Hone, J., Shan, J. & Heinz, T. F. Atomically thin MoS_2: a new direct-gap semiconductor. *Phys. Rev. Lett.* **105**, 136805 (2010).
4. Mak, K. F. & Shan, J. Photonics and optoelectronics of 2D semiconductor transition metal dichalcogenides. *Nat. Photonics* **10**, 216–226 (2016).
5. Wang, Q. H., Kalantar-Zadeh, K., Kis, A., Coleman, J. N. & Strano, M. S. Electronics and optoelectronics of two-dimensional transition metal dichalcogenides. *Nat. Nanotechnol.* **7**, 699–712 (2012).
6. Low, T. et al. Polaritons in layered two-dimensional materials. *Nat. Mater.* **16**, 182–194 (2016).
7. Kim, J. et al. Ultrafast generation of pseudo-magnetic field for valley excitons in WSe_2 monolayers. *Science* **346**, 1205–1208 (2014).
8. Mak, K. F., McGill, K. L., Park, J. & McEuen, P. L. The valley Hall effect in MoS_2 transistors. *Science* **344**, 1489–1492 (2014).
9. Schaibley, J. R. et al. Valleytronics in 2D materials. *Nat. Rev. Mater.* **1**, 16055 (2016).
10. Xu, X., Yao, W., Xiao, D. & Heinz, T. F. Spin and pseudospins in layered transition metal dichalcogenides. *Nat. Phys.* **10**, 343–350 (2014).
11. Sie, E. J. et al. Valley-selective optical Stark effect in monolayer WS_2. *Nat. Mater.* **14**, 290–294 (2014).
12. Basov, D. N., Fogler, M. M. & Garcia de Abajo, F. J. Polaritons in van der Waals materials. *Science* **354**, aag1992–aag1992 (2016).
13. Ceballos, F., Cui, Q., Bellus, M. Z. & Zhao, H. Exciton formation in monolayer transition metal dichalcogenides. *Nanoscale* **8**, 11681–11688 (2016).
14. Steinleitner, P. et al. Direct observation of ultrafast exciton formation in a monolayer of WSe_2. *Nano Lett.* **17**, 1455–1460 (2017).
15. Mak, K. F. et al. Tightly bound trions in monolayer MoS_2. *Nat. Mater.* **12**, 207–211 (2012).
16. Ross, J. S. et al. Electrical control of neutral and charged excitons in a monolayer semiconductor. *Nat. Commun.* **4**, 1474 (2013).
17. You, Y. et al. Observation of biexcitons in monolayer WSe_2. *Nat. Phys.* **11**, 477–481 (2015).
18. Chernikov, A., Ruppert, C., Hill, H. M., Rigosi, A. F. & Heinz, T. F. Population inversion and giant bandgap renormalization in atomically thin WS_2 layers. *Nat. Photonics* **9**, 466–470 (2015).
19. Poellmann, C. et al. Resonant internal quantum transitions and femtosecond radiative decay of excitons in monolayer WSe_2. *Nat. Mater.* **14**, 889–893 (2015).
20. Yuan, L. & Huang, L. Exciton dynamics and annihilation in WS_2 2D semiconductors. *Nanoscale* **7**, 7402–7408 (2015).
21. Yu, Y. et al. Fundamental limits of exciton-exciton annihilation for light emission in transition metal dichalcogenide monolayers. *Phys. Rev. B* **93**, 201111 (2016).
22. Sun, D. et al. Observation of rapid exciton–exciton annihilation in monolayer molybdenum disulfide. *Nano Lett.* **14**, 5625–5629 (2014).
23. Mouri, S. et al. Nonlinear photoluminescence in atomically thin layered WSe_2 arising from diffusion-assisted exciton-exciton annihilation. *Phys. Rev. B* **90**, 155449 (2014).
24. Danovich, M., Zólyomi, V., Fal'ko, V. I. & Aleiner, I. L. Auger recombination of dark excitons in WS_2 and WSe_2 monolayers. *2D Mater.* **3**, 35011 (2016).
25. Cunningham, P. D., McCreary, K. M. & Jonker, B. T. Auger recombination in chemical vapor deposition-grown monolayer WS_2. *J. Phys. Chem. Lett.* **7**, 5242–5246 (2016).
26. Baugher, B. W. H., Churchill, H. O. H., Yang, Y. & Jarillo-Herrero, P. Optoelectronic devices based on electrically tunable p–n diodes in a monolayer dichalcogenide. *Nat. Nanotechnol.* **9**, 262–267 (2014).
27. Furchi, M. M., Polyushkin, D. K., Pospischil, A. & Mueller, T. Mechanisms of photoconductivity in atomically thin MoS_2. *Nano Lett.* **14**, 6165–6170 (2014).
28. Ross, J. S. et al. Electrically tunable excitonic light-emitting diodes based on monolayer WSe_2 p–n junctions. *Nat. Nanotechnol.* **9**, 268–272 (2014).
29. Koppens, F. H. L. et al. Photodetectors based on graphene, other two-dimensional materials and hybrid systems. *Nat. Nanotechnol.* **9**, 780–793 (2014).
30. Haastrup, S., Latini, S., Bolotin, K. & Thygesen, K. S. Stark shift and electric-field-induced dissociation of excitons in monolayer MoS_2 and hBN/MoS_2 heterostructures. *Phys. Rev. B* **94**, 41401 (2016).
31. Pedersen, T. G. Exciton Stark shift and electroabsorption in monolayer transition-metal dichalcogenides. *Phys. Rev. B* **94**, 125424 (2016).
32. Scharf, B. et al. Excitonic Stark effect MoS_2 monolayers. *Phys. Rev. B* **94**, 245434 (2016).
33. Cui, X. et al. Multi-terminal transport measurements of MoS_2 using a van der Waals heterostructure device platform. *Nat. Nanotechnol.* **10**, 534–540 (2015).
34. Andersen, K., Latini, S. & Thygesen, K. S. Dielectric genome of van der Waals heterostructures. *Nano Lett.* **15**, 4616–4621 (2015).
35. Stier, A. V., Wilson, N. P., Clark, G., Xu, X. & Crooker, S. A. Probing the influence of dielectric environment on excitons in monolayer WSe_2: insight from high magnetic fields. *Nano Lett.* **16**, 7054–7060 (2016).
36. Chernikov, A. et al. Exciton binding energy and nonhydrogenic rydberg series in monolayer WS_2. *Phys. Rev. Lett.* **113**, 76802 (2014).

37. He, K. et al. Tightly bound excitons in monolayer WSe_2. *Phys. Rev. Lett.* **113**, 26803 (2014).
38. Ugeda, M. M. et al. Giant bandgap renormalization and excitonic effects in a monolayer transition metal dichalcogenide semiconductor. *Nat. Mater.* **13**, 1091–1095 (2014).
39. Latini, S., Olsen, T. & Thygesen, K. S. Excitons in van der Waals heterostructures: the important role of dielectric screening. *Phys. Rev. B* **92**, 245123 (2015).
40. Klein, J. et al. Stark effect spectroscopy of mono- and few-layer MoS_2. *Nano Lett.* **16**, 1554–1559 (2016).
41. Aivazian, G. et al. Many-body effects in nonlinear optical responses of 2D layered semiconductors. *2D Mater.* **4**, 25024 (2017).
42. Steinhoff, A. et al. Exciton fission in monolayer transition metal dichalcogenide semiconductors. *Nat. Commun.* **8**, 1166 (2017).
43. Wang, H., Zhang, C., Chan, W., Tiwari, S. & Rana, F. Ultrafast response of monolayer molybdenum disulfide photodetectors. *Nat. Commun.* **6**, 8831 (2015).
44. Massicotte, M. et al. Picosecond photoresponse in van der Waals heterostructures. *Nat. Nanotechnol.* **11**, 42–46 (2015).
45. Perebeinos, V. & Avouris, P. Exciton ionization, Franz-Keldysh, and stark effects in carbon nanotubes. *Nano Lett.* **7**, 609–613 (2007).
46. Pedersen, T. G., Latini, S., Thygesen, K. S., Mera, H. & Nikolić, B. K. Exciton ionization in multilayer transition-metal dichalcogenides. *New J. Phys.* **18**, 73043 (2016).
47. Sun, Z., Martinez, A. & Wang, F. Optical modulators with 2D layered materials. *Nat. Photonics* **10**, 227–238 (2016).
48. Wang, L. et al. One-dimensional electrical contact to a two-dimensional material. *Science* **342**, 614–617 (2013).

Acknowledgements

T.G.P. and K.S.T. acknowledge support for CNG by the Danish National Research Foundation, project DNRF103. T.P.G. also acknowledges support for the VKR center of excellence QUSCOPE by the Villum foundation. M.M. thanks the Natural Sciences and Engineering Research Council of Canada (PGSD3-426325-2012). P.S. acknowledges financial support by a scholarship from the "la Caixa" Banking Foundation. F.V. acknowledges financial support from Marie-Curie International Fellowship COFUND and ICFOnest program. F.H.L.K. acknowledges financial support from the Government of Catalonia trough the SGR grant (2014-SGR-1535), and from the Spanish Ministry of Economy and Competitiveness, through the "Severo Ochoa" Programme for Centres of Excellence in R&D (SEV-2015-0522), support by Fundacio Cellex Barcelona, CERCA Programme/Generalitat de Catalunya and the Mineco grants Ramón y Cajal (RYC-2012-12281) and Plan Nacional (FIS2013-47161-P and FIS2014-59639-JIN). Furthermore, the research leading to these results has received funding from the European Union Seventh Framework Programme under grant agreement no. 696656 Graphene Flagship and the ERC starting grant (307806, CarbonLight).

Author contributions

M.M. conceived and designed the experiments under the supervision of F.H.L.K., M.M., D.D., and F.V. fabricated the samples. M.M. and F.V. carried out the experiments. M.M. performed the data analysis and discussed the results with F.H.L.K., F.V., and P.S. T.G.P. developed the Wannier–Mott exciton model. T.P.G, M.B.L., M.D., and V.I.F. performed the electrostatic calculations, and S.H., S.L., and K.S.T. performed the ab-initio calculations. K.W. and T.T. provided hBN crystals. M.M., F.V., P.S., and F.H.L.K. co-wrote the manuscript, with the participation of T.G.P. and K.S.T.

Additional information

Supplementary Information accompanies this paper at https://doi.org/10.1038/s41467-018-03864-y

Competing interests: The authors declare no competing interests.

Reprints and permission information is available online at http://npg.nature.com/reprintsandpermissions/

Publisher's note: Springer Nature remains neutral with regard to jurisdictional claims in published maps and institutional affiliations.

CHAPTER 7

Conclusion and Outlook

In this thesis, we have seen how we can use electronic structure theory to calculate a wide range of properties for a vast range of two-dimensional materials. The structures have been generated using combinatorial lattice decoration of the known two-dimensional structures.

We have also seen how the use of an automated workflow truly helps in performing electronic structure calculations, and reduces the time it takes to calculate any given property.

The properties calculated in the database can serve as a look-up table for experimental researchers, and they well-documented high-quality calculations can be used to benchmark and compare different codes and methodologies. In addition to these uses of the data, we have seen how data-driven approaches can be used to determine structure-property relations, and in the future it will be interesting to explore this further. Eventually, this will hopefully lead to new models and descriptors, which can help determine properties of interest without having to do *ab-initio* calculations.

In this vein, it would be natural to extend the workflow to calculate parameters which appear in less computationally expensive models, such as the momentum matrix elements for $\mathbf{k} \cdot \mathbf{p}$ perturbation theory, or localized Wannier functions to calculate Born charges and piezoelectric coefficients.

We have also seen how access to high-quality calculations allows us to assess the performance of simpler models, and understand in more detail how and why they break down. Once more properties are calculated, it will be interesting to continue this work, and to use these validations as a guide for model development.

In this work we have identified hundreds of novel, stable two-dimensional materials and some tens of materials with interesting properties, including semiconductors with high intrinsic carrier mobility and ferro-magnets with large magnetic anisotropy, as well as plasmons in the visible energy range. It will be interesting to study these materials in more detail. In particular, all of the materials properties are calculated for the perfect crystalline materials, and for many applications taking defects into account will be necessary.

Finally, we have seen how the method of complex scaling can be used to describe open quantum systems, and applied the theory to the dissociation of excitons in MoS_2 and WSe_2.

APPENDIX A

A Note on units

In this work, unless otherwise stated, we are working in Hartree atomic units.

In practice, this means that the following four elemental constants have been set to one: The reduced Planck's constant, $\hbar$; The elementary charge, e; The electron mass, m_e; and Coulomb's constant, $\frac{1}{4\pi\varepsilon_0}$. In these units, an electron has mass 1 and charge -1, and it creates an electric potential given by $V(\mathbf{r}) = \frac{1}{r}$. Table A.1 shows how quantities in atomic units are related to those in SI units.

Quantity	Atomic unit	SI equivalent
Mass	Electron mass (m_e)	9.11×10^{-31} kg
Length	Bohr radius (a_0)	5.29×10^{-11} m
Time		2.42×10^{-17} s
Energy	Hartree (Ha)	4.36×10^{-18} J

Table A.1: The atomic units of mass, time, length and energy, and their relation to SI units.

Bibliography

[1] John Bardeen. "Surface states and rectification at a metal semi-conductor contact". In: *Physical Review* 71.10 (1947), page 717.

[2] JL Moll et al. "PNPN transistor switches". In: *Proceedings of the IRE* 44.9 (1956), pages 1174–1182.

[3] Linda Wilson. "International technology roadmap for semiconductors (ITRS)". In: *Semiconductor Industry Association* (2013).

[4] Kostya S Novoselov et al. "Electric field effect in atomically thin carbon films". In: *science* 306.5696 (2004), pages 666–669.

[5] Alexander A. Balandin et al. "Superior thermal conductivity of single-layer graphene". eng. In: *Nano Letters* 8.3 (2008), pages 902–907. DOI: 10.1021/nl0731872.

[6] Alexander S. Mayorov et al. "Micrometer-Scale Ballistic Transport in Encapsulated Graphene at Room Temperature". eng. In: *Nano Letters* 11.6 (2011), pages 2396–2399.

[7] Changgu Lee et al. "Measurement of the elastic properties and intrinsic strength of monolayer graphene". eng. In: *Science* 321.5887 (2008), pages 385–388. DOI: 10.1126/science.1157996.

[8] Charles L Kane and Eugene J Mele. "Quantum spin Hall effect in graphene". In: *Physical review letters* 95.22 (2005), page 226801.

[9] Richard Balog et al. "Bandgap opening in graphene induced by patterned hydrogen adsorption". In: *Nature materials* 9.4 (2010), page 315.

[10] Melinda Y Han et al. "Energy band-gap engineering of graphene nanoribbons". In: *Physical review letters* 98.20 (2007), page 206805.

[11] Filip A Rasmussen and Kristian S Thygesen. "Computational 2D materials database: Electronic structure of transition-metal dichalcogenides and oxides". In: *The Journal of Physical Chemistry C* 119.23 (2015), pages 13169–13183.

[12] Miguel M Ugeda et al. "Characterization of collective ground states in single-layer NbSe 2". In: *Nature Physics* 12.1 (2016), page 92.

[13] Jaekwang Lee et al. "Strain-engineered optoelectronic properties of 2D transition metal dichalcogenide lateral heterostructures". In: *2D Materials* 4.2 (2017), page 021016.

[14] Ying Wang et al. “Structural phase transition in monolayer MoTe 2 driven by electrostatic doping”. In: *Nature* 550.7677 (2017), page 487.

[15] Andre K Geim and Irina V Grigorieva. “Van der Waals heterostructures”. In: *Nature* 499.7459 (2013), pages 419–425.

[16] Simone Latini. “Excitons in van der Waals Heterostructures: A theoretical study”. eng. 2016.

[17] Nicolas Mounet et al. “Novel two-dimensional materials from high-throughput computational exfoliation of experimentally known compounds”. In: *arXiv preprint arXiv:1611.05234* (2016).

[18] Kurt Lejaeghere et al. “Reproducibility in density functional theory calculations of solids”. In: *Science* 351.6280 (2016), aad3000.

[19] L. H. Thomas. “The calculation of atomic fields”. eng. In: *Mathematical Proceedings of the Cambridge Philosophical Society* 23.05 (1927), page 542. DOI: 10.1017/S0305004100011683.

[20] E Fermi. “Application of statistical gas methods to electronic systems”. und. In: *Atti Della Reale Accademia Nazionale Dei Lincei* 6 (1927), pages 602–607, 602–607.

[21] P Hohenberg and W Kohn. “Inhomogeneous Electron Gas”. eng. In: *Physical Review B* 136.3B (1964), B864–+. DOI: 10.1103/PhysRev.136.B864.

[22] W Kohn and LJ Sham. “Self-consistent equations including exchange and correlation effects”. eng. In: *Physical Review* 140.4A (1965), pages 1133–. DOI: 10.1103/PhysRev.140.A1133.

[23] Paul AM Dirac. “Note on exchange phenomena in the Thomas atom”. In: *Mathematical Proceedings of the Cambridge Philosophical Society*. Volume 26. 3. Cambridge University Press. 1930, pages 376–385.

[24] David M Ceperley and BJ Alder. “Ground state of the electron gas by a stochastic method”. In: *Physical Review Letters* 45.7 (1980), page 566.

[25] Klaus Capelle. “A bird’s-eye view of density-functional theory”. eng. In: *Brazilian Journal of Physics* 36.4A (2006), pages 1318–1343. DOI: 10.1590/S0103-97332006000700035.

[26] Mark S. Hybertsen and Steven G. Louie. “First-Principles Theory of Quasiparticles: Calculation of Band Gaps in Semiconductors and Insulators”. In: *Phys. Rev. Lett.* 55.13 (September 1985), pages 1418–1421. DOI: 10.1103/PhysRevLett.55.1418.

[27] M Gajdos et al. “Linear optical properties in the projector-augmented wave methodology”. eng. In: *Physical Review B* 73.4 (2006), page 045112. DOI: 10.1103/PhysRevB.73.045112.

[28] J. P. Perdew, K. Burke, and M. Ernzerhof. “Generalized Gradient Approximation Made Simple”. In: *Physical Review Letters* 77 (November 1996), pages 3865–3868. DOI: 10.1103/PhysRevLett.77.3865.

[29] Lars Hedin. “New Method for Calculating the One-Particle Greenś Function with Application to the Electron-Gas Problem”. In: *Phys. Rev.* 139.3A (August 1965), A796–A823. DOI: 10.1103/PhysRev.139.A796.

[30] Jorge Kohanoff. *Electronic structure calculations for solids and molecules: theory and computational methods*. Cambridge University Press, 2006.

[31] J e Enkovaara et al. “Electronic structure calculations with GPAW: a real-space implementation of the projector-augmented-wave method”. In: *Journal of Physics: Condensed Matter* 22.25 (2010), page 253202.

[32] Ask Larsen et al. “The Atomic Simulation Environment—A Python library for working with atoms”. In: *Journal of Physics: Condensed Matter* (2017).

[33] Peter E Blochl, Clemens J Forst, and Johannes Schimpl. “Projector augmented wave method: ab initio molecular dynamics with full wave functions”. In: *Bulletin of Materials Science* 26.1 (2003), pages 33–41.

[34] Marco Bernardi, Maurizia Palummo, and Jeffrey C. Grossman. “Extraordinary Sunlight Absorption and One Nanometer Thick Photovoltaics Using Two-Dimensional Monolayer Materials”. In: (2013).

[35] R KUBO. “Statistical-mechanical theory of irreversible processes 1. General theory and simple applications to magnetic and conduction problems”. eng. In: *Journal of the Physical Society of Japan* 12.6 (1957), pages 570–586.

[36] Erich Runge and E. K. U. Gross. “Density-Functional Theory for Time-Dependent Systems”. In: *Phys. Rev. Lett.* 52 (12 March 1984), pages 997–1000. DOI: 10.1103/PhysRevLett.52.997.

[37] Nathan Wiser. “Dielectric Constant with Local Field Effects Included”. In: *Phys. Rev.* 129.1 (January 1963), pages 62–69. DOI: 10.1103/PhysRev.129.62.

[38] Jun Yan et al. “Linear density response function in the projector augmented wave method: Applications to solids, surfaces, and interfaces”. In: *Phys. Rev. B* 83.24 (2011), page 245122. DOI: 10.1103/PhysRevB.83.245122.

[39] Stephen L. Adler. “Quantum Theory of the Dielectric Constant in Real Solids”. In: *Phys. Rev.* 126.2 (April 1962), pages 413–420. DOI: 10.1103/PhysRev.126.413.

[40] Falco Hüser, Thomas Olsen, and Kristian S Thygesen. “How dielectric screening in two-dimensional crystals affects the convergence of excited-state calculations: Monolayer MoS 2”. In: *Physical Review B* 88.24 (2013), page 245309.

[41] S Latini, T Olsen, and K S Thygesen. “Excitons in van der Waals heterostructures: The important role of dielectric screening”. In: *Phys. Rev. B* 92.24 (December 2015), page 245123. DOI: 10.1103/PhysRevB.92.245123.

[42] Pierluigi Cudazzo, Ilya V Tokatly, and Angel Rubio. “Dielectric screening in two-dimensional insulators: Implications for excitonic and impurity states in graphane”. In: *Physical Review B* 84.8 (2011), page 085406.

[43] D. G. Pettifor. “Chemical scale for crystal-structure maps”. eng. In: *Solid State Communications* 51.1 (1984), pages 31–34.

[44] Henning Glawe et al. “The optimal one dimensional periodic table: a modified Pettifor chemical scale from data mining”. eng. In: *New Journal of Physics* 18.9 (2016), page 093011. DOI: 10.1088/1367-2630/18/9/093011.

[45] Ji Chen et al. “Two Dimensional Ice from First Principles: Structures and Phase Transitions”. In: *Phys. Rev. Lett.* 116 (2 January 2016), page 025501. DOI: 10.1103/PhysRevLett.116.025501.

[46] Mohnish Pandey and Karsten W. Jacobsen. “Heats of formation of solids with error estimation: The mBEEF functional with and without fitted reference energies”. In: *Phys. Rev. B* 91 (23 June 2015), page 235201. DOI: 10.1103/PhysRevB.91.235201.

[47] Ralph Walter Graystone Wyckoff. *The Analytical Expression of the Results of the Theory of Space-groups*. 318. Carnegie institution of Washington, 1922.

[48] Ankit Jain. Private Communication. September 1, 2018.

[49] Peter Mahler Larsen. “Structural Analysis Algorithms for Nanomaterials”. PhD thesis. Department of Physics, DTU, September 2017, pages 21–36.

[50] Robert R Sokal and F James Rohlf. “The comparison of dendrograms by objective methods”. In: *Taxon* (1962), pages 33–40.

[51] G. Grosso and G.P. Parravicini. *Solid State Physics*. Elsevier Science, 2000.

[52] Korina Kuhar. “Computational screening of new inorganic materials for highly efficient solar energy conversion”. eng. 2017.

[53] Thomas Olsen et al. “Simple Screened Hydrogen Model of Excitons in Two-Dimensional Materials”. eng. In: *Physical Review Letters, Phys. Rev. Lett, Phys Rev Lett, Phys Rev L, Prl* 116.5 (2016), page 5. DOI: 10.1103/physrevlett.116.056401.

[54] Y. Yu and M. Cardona. *Fundamentals of Semiconductors*. eng. Springer Berlin Heidelberg, 1996, 617 s.

[55] Alex Krizhevsky, Ilya Sutskever, and Geoffrey E Hinton. “Imagenet classification with deep convolutional neural networks”. In: *Advances in neural information processing systems*. 2012, pages 1097–1105.

[56] Geoffrey Hinton et al. “Deep neural networks for acoustic modeling in speech recognition: The shared views of four research groups”. In: *IEEE Signal processing magazine* 29.6 (2012), pages 82–97.

[57] Denis Tomè et al. “Deep convolutional neural networks for pedestrian detection”. In: *Signal processing: image communication* 47 (2016), pages 482–489.

[58] David Silver et al. “Mastering the game of Go with deep neural networks and tree search”. In: *nature* 529.7587 (2016), page 484.

[59] Keith T. Butler et al. “Machine learning for molecular and materials science”. eng. In: *Nature* 559.7715 (2018), pages 547–555. DOI: 10.1038/s41586-018-0337-2.

[60] Tim Mueller, Aaron Gilad Kusne, and Rampi Ramprasad. “MACHINE LEARNING IN MATERIALS SCIENCE: RECENT PROGRESS AND EMERGING APPLICATIONS”. eng. In: *Reviews in Computational Chemistry* 29 (2016), pages 186–273.

[61] Matthias Rupp et al. “Fast and Accurate Modeling of Molecular Atomization Energies with Machine Learning”. In: *Phys. Rev. Lett.* 108 (5 January 2012), page 058301. DOI: 10.1103/PhysRevLett.108.058301.

[62] Haoyan Huo and Matthias Rupp. “Unified Representation of Molecules and Crystals for Machine Learning”. und. In: (2018).

[63] Katja Hansen et al. “Machine learning predictions of molecular properties: Accurate many-body potentials and nonlocality in chemical space”. In: *The journal of physical chemistry letters* 6.12 (2015), pages 2326–2331.

[64] Sandip De et al. “Comparing molecules and solids across structural and alchemical space”. eng. In: *Physical Chemistry Chemical Physics* 18.20 (2016), pages 13754–13769. DOI: 10.1039/c6cp00415f.

[65] Felix A Faber et al. “Alchemical and structural distribution based representation for universal quantum machine learning”. In: *The Journal of Chemical Physics* 148.24 (2018), page 241717.

[66] S Takagi, A Toriumi, and M Iwase. “On the universality of inversion layer mobility in Si MOSFET’s: Part I-effects of substrate impurity concentration”. In: *IEEE Transactions on Electron Devices* 41.12 (1994), pages 2357–2362. DOI: 10.1109/16.337449.

[67] Bevin Huang et al. “Layer-dependent ferromagnetism in a van der Waals crystal down to the monolayer limit”. In: *Nature* 546.7657 (2017), page 270.

[68] N. D. Mermin and H. Wagner. “Absence of Ferromagnetism or Antiferromagnetism in One- or Two-Dimensional Isotropic Heisenberg Models”. In: *Physical Review Letters* 17 (November 1966), pages 1133–1136. DOI: 10.1103/PhysRevLett.17.1133.

[69] Miguel M Ugeda et al. “Giant bandgap renormalization and excitonic effects in a monolayer transition metal dichalcogenide semiconductor”. In: *Nature materials* 13.12 (2014), page 1091.

[70] Ziliang Ye et al. “Probing excitonic dark states in single-layer tungsten disulphide”. In: *Nature* 513.7517 (August 2014), pages 214–218. DOI: 10.1038/nature13734. eprint: 1403.5568.

[71] GG Macfarlane et al. “Exciton and phonon effects in the absorption spectra of germanium and silicon”. In: *Journal of Physics and Chemistry of Solids* 8 (1959), pages 388–392.

[72] AR Klots et al. “Probing excitonic states in suspended two-dimensional semiconductors by photocurrent spectroscopy”. In: *Scientific reports* 4 (2014).

[73] J. Stark. “Observation of the Separation of Spectral Lines by an Electric Field”. eng. In: *Nature* 92.2301 (1913), pages 401–401. DOI: 10.1038/092401b0.

[74] Giovanni Onida, Lucia Reining, and Angel Rubio. “Electronic excitations: density-functional versus many-body Green’s-function approaches”. In: *Rev. Mod. Phys.* 74 (2 June 2002), pages 601–659. DOI: 10.1103/RevModPhys.74.601.

[75] Giuseppe Grosso and Giuseppe Pastori Parravicini. “Solid state physics”. eng. In: (2000).

[76] Thomas Olsen et al. “Simple Screened Hydrogen Model of Excitons in Two-Dimensional Materials”. In: 3 (2015), pages 1–5. arXiv: 1510.06777.

[77] F. Gesztesy et al., editors. *Spectral Theory and Mathematical Physics: A Festschrift in Honor of Barry Simon’s 60^{th} Birthday*. 2007.

[78] Siegert. “Derivation of dispersion formula for nuclear reactions”. In: *Physical Review* 56 (1939), pages 750–752.

[79] Naomichi Hatano et al. “Some properties of the resonant state in quantum mechanics and its computation”. und. In: *Progress of Theoretical Physics* 119.2 (2008), pages 187–222.

[80] W. P. Reinhardt. “Complex Coordinates in the Theory of Atomic and Molecular Structure and Dynamics”. In: *Annual Review of Physical Chemistry* 33 (1982), pages 223–255. DOI: 10.1146/annurev.pc.33.100182.001255.

[81] Balslev and Combes. “Spectral properties of many-body Schrodinger operators with dilatation- analytic interactions”. In: *Communications in Mathematical Physics* 22.4 (1971), pages 280–294. DOI: 10.1007/BF01877511.

[82] Ira W. Herbst. “Dilation analyticity in constant electric field”. In: *Communications in Mathematical Physics* 64.3 (1979), pages 279–298. DOI: 10.1007/bf01221735.